Department of Earth and Environmental Sciences

Director: Prof. G. Rossi

Master course Geosciences for Sustainable Resources

PETROLOGY AND Nd-Sr-Pb ISOTOPIC COMPOSITIONS OF GABBROS FROM THE SHIKOKU BACK-ARC BASIN, PHILIPPINE SEA

Supervisor
Prof. Alessio Sanfilippo
Co-supervisors
Prof. Martina Casalini, Dr. Valentin Basch

Master thesis
in Geosciences for Sustainable Resources
of Francesca Dimasi
matr. 527188

Academic Year 2023/2024

CHAPTER 1 – INTRODUCTION

1.1 Geodynamic of back-arc basin

1.2 Back-arc basin basalts: geochemical composition and comparison with MORB

CHAPTER 2 – GEOLOGICAL SETTING

2.1 Philippine Sea back-arc basin

2.2 Isotopic characteristics of Philippine Sea basalts

2.3 Oceanic Core Complexes

2.4 Mado Oceanic Core Complex

2.5 Nankaido OCCs group: Tosa and Sanuki

CHAPTER 3 – SAMPLE SELECTION AND ANALYTICAL TECHNIQUES

3.1 Sample selection

3.2 Analytical techniques

- 3.2.1 Optical microscope study
- 3.2.2 Sr-Nd-Pb isotope determinations
- 3.2.3 Sample preparation for isotopic analyses
- 3.2.4 Thermal ionization mass spectrometry (TIMS)

CHAPTER 4 – RESULTS

4.1 Petrography

- 4.1.1 Central Mado

4.1.1. a) Olivine-Gabbro

4.1.1 b) Gabbro

4.1.1 c) Varitextured Gabbros

4.1.1 d) Felsic Veins (contact)

- 4.1.2 Mado along the Transform fault

4.1.2 a) Mylonitic Oxide Gabbros

4.1.2. b) Mylonitic Gabbros

- 4.1.3 Tosa and Sanuki (Nankaido OCCs)

4.1.3. a) Oxide Diorites

4.1.3 c) Basaltic Andesite – Oxides Diorite contact

4.2 Major and trace element compositions of the mineral phases

- 4.2.1 Plagioclase
- 4.2.2 Clinopyroxene
- 4.2.3 Amphibole

4.3 Isotopic compositions

CHAPTER 5 – DISCUSSION AND CONCLUSIONS

5.1.1 Petrographic evidence

5.1.2 Major and trace elements

5.1.3 Isotopic compositions and geodynamic implication

5.2 Synthesis and geodynamic implicatons

CHAPTER 6 - BIBLIOGRAPHY

CHAPTER 1 – INTRODUCTION

Back-arc basins account for the formation of a significant fraction of the seafloor worldwide. (Sdrolias & Müller, 2006; Taylor & Martinez, 2003). In these systems, magmatism is closely linked to the influx of subduction fluids within the upper mantle, and the composition of the lower oceanic crust formed during back-arc expansion has never been characterized in detail, nor has an archetype of back-arc lithosphere composition been defined. Oceanic spreading is a key component of global tectonic cycles and needs to be thoroughly constrained in the effort to understand the Earth's evolution. This research thesis aims at providing constraints on the petrography and geochemical composition of the lower gabbroic crust sampled in the Shikoku Basin (Philippine Sea). Sampling at increasing distance from the extinct spreading center will allow us to evaluate the compositional evolution of parental melts over the lifespan of the back arc basin, from initial spreading to its extinction. In turn, we will assess the compositional evolution of the oceanic lithosphere in relation with its geodynamic setting. Hence, this thesis will furnish new data to compare the magmatic features of ocean ridges formed at back-arc basins with those of the better-known mid-ocean ridges.

The Philippine Sea is constituted by three basins that formed as a result of the westward subduction of the Pacific plate. The westernmost basin is the first to have opened between ~65 and ~35 Myr, and is characterized by a NE-SW spreading direction. After ~10 Ma, the spreading ridge associated with the Western Philippine basin was no longer stable, and jumped towards the east, closer to the subduction trench. This process led to the opening of a second basin, with the Shikoku basin, on the North, and the Parece Vela basin, on the South. The latter is also extinct nowadays, since ~15 Myr ago the active spreading was relocated eastward, along the Mariana Trough, active to date. The instability of the spreading ridge was most likely dictated by the retreat of the subducting slab in both cases. This slab roll-back results from the sinking of the old and heavy Pacific slab. (Mrozowski and Hayes, 1979; Shih, 1980b). We postulate that the ridge relocation can be related to variations in slab morphology, which governs the subduction fluid supplied into the upper mantle. A decline in fluid influx might lead to *i)* displacement of the main magmatic activity from the ridge to the volcanic arc, and to *ii)* the extinction of the ridge and opening of a new basin, 'splitting' the volcanic arc in two. Our sampling of the lower gabbroic crust of the Shikoku basin includes areas formed during both the early spreading (~25-30 Myr) towards the extinction of the ridge activity (~15 Myr). This allows us to reconstruct the compositional evolution of the basin over time and extrapolate the relationship with the geodynamic subducting slab architecture.

To characterize the gabbroic lithologies forming the lower oceanic crust in these settings, we will complete a previous petrographic description of the samples, followed by major and trace element analyses of the main minerals composing these lithologies (olivine, plagioclase, clinopyroxene, amphibole, ilmenite). In order to trace the involvement of fluids in the formation of parental melts, this thesis will complete an existing geochemical dataset with new determination of Sr, Nd and Pb radiogenic isotopes performed on clinopyroxene and amphibole handpicking chips.

The main scientific question of this research work: is there a variation in the influx of subduction fluids during the life cycle of the magmatism in the Shikoku basin?
The main hypothesis to be tested is that the system evolves from having high amounts of fluids during the early phases of back-arc spreading to an anhydrous environment, equivalent or slightly more hydrated compared to mid-ocean ridges. This variation in fluid influx mainly results from the retreat of the subducting slab.

1.1 Geodynamic of back-arc basin

Subduction zones develop at convergent margins, where one plate subducts beneath another. In the over-riding plate, a magmatic arc develops, typically explosive and hazardous to human populations due to the high volatile contents in the arc magmas (e.g., Tatsumi and Suzuki-Kamata, 2014). Behind the volcanic arc, in areas characterized by an extensional regime, a back-arc basin can develop (Fig.1), first defined by Karig in 1971. It is worth noting that not all subduction systems are associated with back-arc basins; although all the processes related to these two tectonic regimes (subduction and extension) can influence each other, extension is not guaranteed behind convergent margins; in some systems extension ceases but subduction continues (Artemieva, 2023). Moreover, if lithospheric extension occurs, it may or may not evolve into seafloor spreading; some authors believe that if the overlying plate is of oceanic type, the back-arc rifting systematically transitions to seafloor spreading. The extent of back-arc opening, however, tends to be limited in width by the length of the subduction system; back-arc basins never lead to the birth of large oceans but rather to multiple small-scale basins (I.M. Artemieva, 2023).
The mechanisms that can lead to the opening of a back-arc basin in this geodynamic context have been long debated and studied. Nowadays, various models of back-arc basin aperture exist for the different kinds of systems. Some of these aperture patterns and/or parameters are discussed in the following.

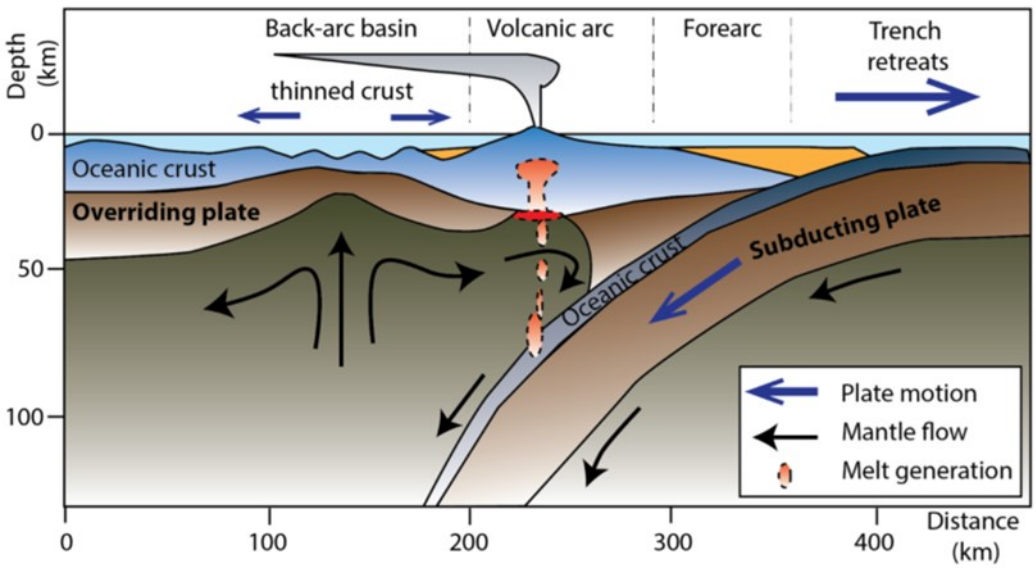

Figure 1: Schematic draw of geodynamic environment, as back-arc basin - magmatic arc - subduction system.

According to Sdrolias (2006), the main factors that trigger the opening of back-arc basins are: 1) the age of the subducting lithosphere, 2) convergence rate and direction, 3) absolute motion of the downgoing and overriding plates, 4) rollback of the subduction hinge, and 5) dip angle of the subducting slab.

The age of the subducting oceanic crust is fundamental and, to be a triggering factor, must necessarily be greater than 55 million years old. The age of the crust generally influences its density and weight, which in turn influences the slab-lateral mantle flow interaction, as well as the subduction slab angle. The latter, which apparently controls the location of the slab melting zone and the efficiency of slab roll-back, must reach a critical intermediate dip angle of 30° for the opening to begin. While the overriding plate moves away from the trench, thus ensuring the creation of an accommodation space. Such accommodation space will also be affected by the passive rollback of the subduction hinge and the mantle flow dragging the subducting slab downward. Finally, once spreading begun, the rate of rollback of the subduction hinge increases.

Therefore, the extension/evolution of the back-arc basin system associated with subduction depends on the surface kinematics, the characteristics of the subducting slab and the lateral mantle flow acting on the subducting slab.

Artemieva (2023) focused on the geophysical and tectonic characteristics of 31 offshore back-arc basins and sub-basins worldwide (Fig.2) deriving three main opening models: *i*) the roll-back slab model, *ii*) deeply anchored slab model, and *iii*) lateral mantle flow model.

The *slab roll-back model* has a trench retreating because of combined forces of slab pull and gravity. In these conditions the overlying plate tends to follow the retreat of the trench, passively forming an extension of the lithospheric crust behind the volcanic arc. In some cases, this process can

also subdivide the arc in an active and an extinct segment, or even create an extension in front of the volcanic arc (i.e., forearc zone). Both cases, the extension zone will be characterized by weak rheological conditions, caused by? temperature and hydration. In these systems the weakest part of the lithosphere will be located above 65-170 km depth, i.e. above the melt production region.

The *depth-anchored subduction slab model* predicts that the trench is fixed, resulting in extension only occurring if the overlying plate moves landward, trailing the slab. Fracturing instead of tensile deformation is not possible due to the much greater lithostatic load (see also Shemenda, 1993; Mantovani et al., 2001). Therefore, the extensive process depends on the relative motion of the plate with respect to the trench. Furthermore, this extensional stress is also influenced by the hydrodynamic force of the viscous asthenosphere moving upwards. The magnitude of the hydrodynamic force in turn depends on overriding plate velocity, slab surface and mantle viscosity. Despite the 'deep anchor' model was designed with the aim of explaining the extension in the Mariana Trough (Uyeda and Kanamori, 1979; Stern et al., 2003), the slab associated with the Mariana subduction, i.e. the Philippine Sea plate, appears not to be entirely anchored and the model is still debated.

The *lateral mantle flow model* predicts that if the lateral mantle flow has the same direction as the subducting plate, the latter will have a low angle, the slab will be assimilated closer to the surface hampering the formation of a back-arc basin. If the lateral mantle flow, however, moves in the opposite direction respect to subduction direction, this will lead to an increase in the subduction angle of the slab with retreat of the trench and formation of the back-arc basin. This model is supported by numerical modelling and is ultimately associated with the slab roll-back with migration of the slab hinge towards the same direction as the mantle flow. A similar model was proposed by Doglioni (1991) to explain the opening of the Tyrrhenian Sea back-arc basin associated to the Ionian subduction in southern Italy.

In all models, the characteristics of the overlying oceanic plate are fundamental conditions for the opening of the back-arc basin and the development of the entire subduction system. In this framework the convergence can be ocean-ocean, arc-ocean, or continent-ocean.

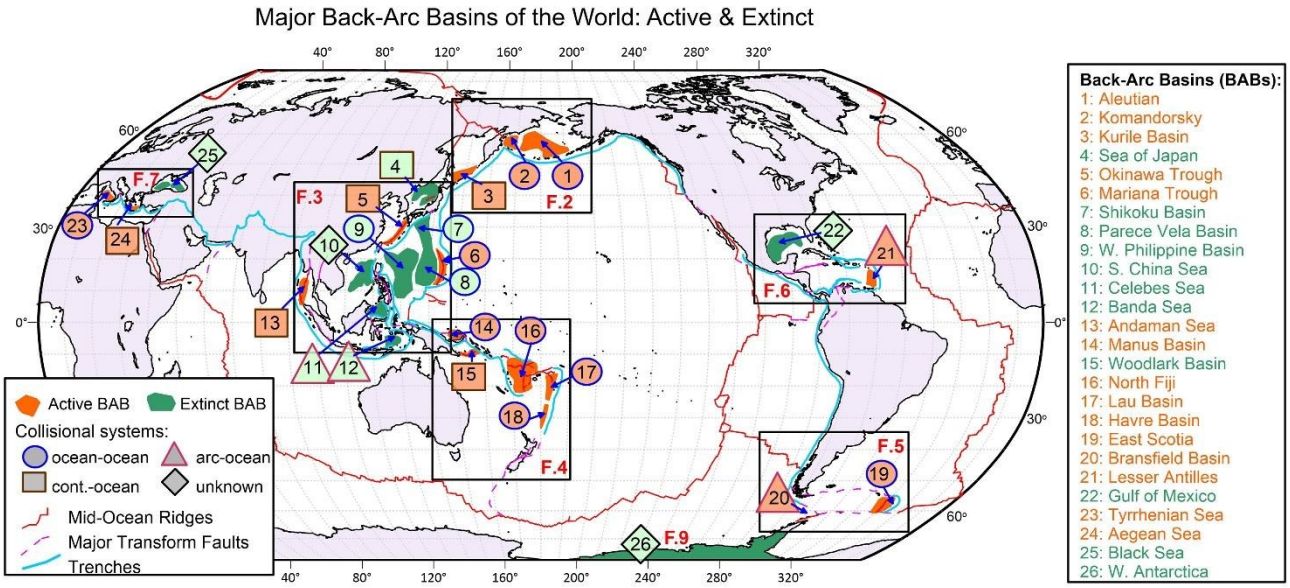

Figure 2: Global Map of major off-shore back-arc basins, in green extinct BABs and in red active ones (I.M. Artemieva, 2023).

1.2 Back-arc basin basalts: geochemical composition and comparison with MORB

The very first studies on basalts recovered from back-arc basins (BAB) focused on the similarity of the latter with basalts produced along mid-ocean ridges (i.e., MOR Basalts). Only after the pioneering study of Gill (1976) the BABB started to be considered as a different type of magmatism, intermediate between MORB and Island-Arc Basalts (IAB). A substantial difference discovered between MORB and BABB is the primary water content, which is higher in the BAB type basalts, as proposed by Gill (1976) for the volcanic glasses from the Mariana Trough and by Garcia et al. (1979) for the basalts from the East Scotia Sea. The other great difference with MORB is that BABB have enrichments of LILE (Large-Ion Lithophile Elements), i.e. fluid mobile elements such as Rb, Ba and Light Rare Earth element, decreases in HFSE (High Field Strength Elements) i.e. fluid immobile elements such as Ti, Zr and Hf, and high radiogenic $^{87}Sr/^{86}Sr$ isotope ratios. These characteristics, shared with IAB, are due to the increasing extent of melting (at lower pressures) or to the saturation of water-bearing phases during the fractionation/crystallization of the melt (i.e., amphibole), triggered by the addition of a fluid component.

Hawkins and Melchior (1985) confirmed that both MORB-type and BAB-type basalts can be found at back-arc basins, depending on the contribution from the subducted slab, which is limited to less than 100 km from the front of the volcanic arc. This transition in a single geodynamic system is highlighted by the systematic trace element variation seen above. Specifically, the marginal part of the basin tends to have a BAB-type composition and to be floored by attenuated arc crust (Gill,1976). While the spreading centers of the back arc basin have a MORB-like composition, to gradually changes as it gets closer to the volcanic arc and therefore to the active subduction zone. Examples of

back arc basins witnesses of this geochemical transition are the Lau Basin (Pearce et al.,1995) and the East Scotia Sea (Leat et al., 2000 and Fretzdorff et al., 2002). However, the geochemical zoning of back arc basin and their magma type distribution seems more complicated and not valid globally. For instance, BABB in the Manus Basin are characterized by LREE, P, and Zr enrichments compared to MORB (Sinton et al., 2003), whereas those in the North Fiji basin have MORB composition, having almost all the spreading axes distant from the subduction zone (Eissen et al., 1991).

For a better comparison, three terms will be used, following classification of Gale et al. (2013): “all MORB”, “all MORB plus BABB” and “all normal MORB”.

The term “all MORB” indicates the average composition of the basaltic portion of the oceanic crust (N-MORB, E-MORB, D-MORB), excluding the back-arc basins and the basalts originating in environments influenced by the presence of plumes.

Mantle plumes can influence the composition of the upper mantle portion, in which they are found for hundreds of km (enrichment in most incompatible elements), while the formation of BAB influences the local composition of the crust for <100 km and is closely related to the influence of the nearby slab in subduction magmatic arc developed during subduction.

The term “all normal MORB” excludes both BABs and the global ridge system that are less than 500 km from the hot-spot or plume.

The term “all MORB plus BABB” includes all the normal MORBs plus back-arc basin basalts. “All MORB plus BABB” and "all normal MORB" have average compositions of moderately incompatible elements that are very similar, but their average composition diverges for the highly incompatible elements, from Pr on. The "all normal MORB” group therefore has a concentration of incompatible elements less than 15% compared to “all MORB’’. The "all MORB" and “all MORB plus BABB” groups present very similar concentrations of incompatible elements but differ in the lower ratios of Ce/Pb, Rb/Cs, Ba/Cs in the latter.

Regarding major element contents, BAB basalts have low averages of MgO and TiO_2 and higher SiO_2, K_2O and Al_2O_3. Furthermore, the average content of FeO and CaO in BAB is also lower than in MORB. These fine variations can be due to the different crystal forming during the magma evolution. During fractional crystallization of a dry tholeiitic melt, the first crystal to saturate in the liquidus phase is olivine, followed by plagioclase and clinopyroxene. Therefore, one would expect an increase in Fe and Ti, coupled to decreases in MgO and Al contents. In the BAB these elements show an opposite behaviour, which has been explained by the delayed crystallization of plagioclase and early saturation of amphibole in hydrated conditions (Basch et al. 2020).

Trace elements agree with what is reported above. The main evidence is the low concentration of moderately and highly incompatible elements in BAB, which are about 20% less abundant than in

MORB. Observing relationship between BABB and MORB in Graph A (Fig.3), enrichments in Cs, Rb, Ba, U, Pb and Sr in BABB trend are clear notable. Finally, evidence of more depleted sources for BABB than MORB are the low ratios of Zr/Sm, Zr/Hf and Y/Yb.

Observing the complete pattern (Fig.3) of enrichment of the fluid-mobile elements of the BABBs we note how this is very similar to the pattern of the involved fluid phase (Gale et al., 2010). The latter is also called "wet component" calculated by Bezos et al. 2009 for the Lau Basin, using the principal components analysis (PCA) for arbitrary water content (50 wt.%) they determined the concentrations of all other elements. They found diagnostic depletion in Nb-Ta, K_2O or La, and high ratios of Ba/Th, Pb/Nd, La/Nb and Sr/Nd, in addition to La/Nd less than 0,8.

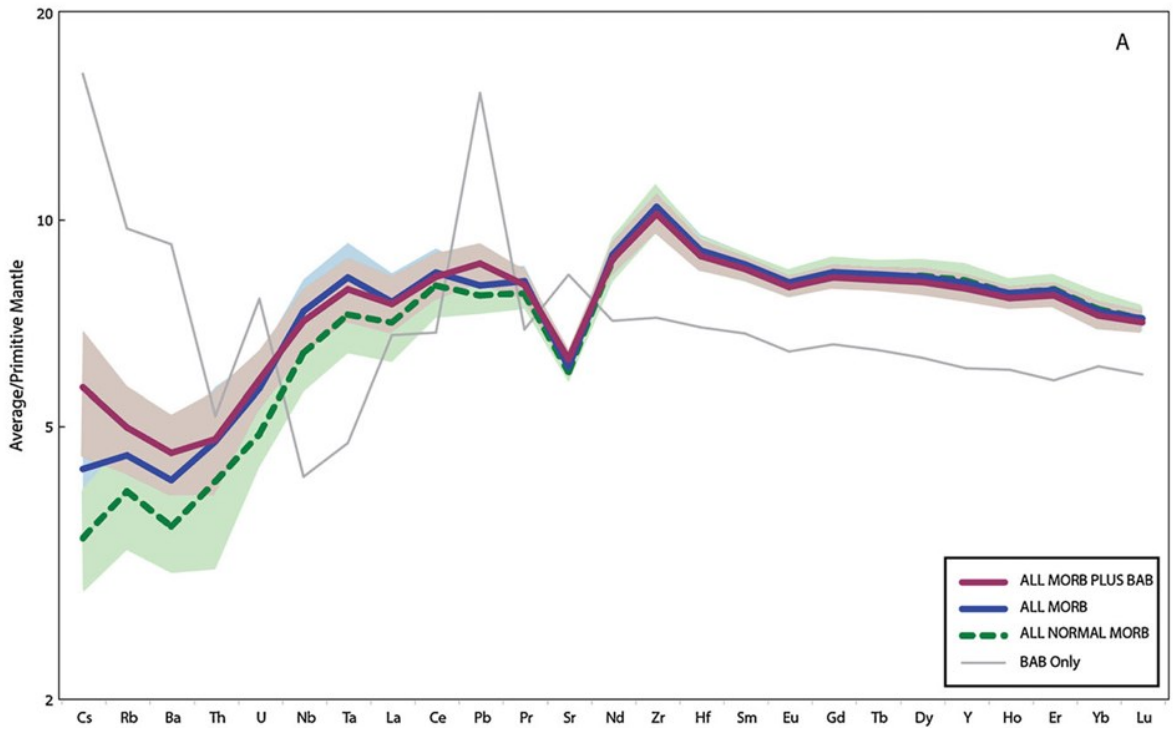

Figure 3: Average composition (normalized in the primitive mantle) vs trace elements of ALL MORB, ALL MORB PLUS BAB, ALL NORMALMORB, from Sun and McDonough, (1989). Graph A shows positive anomalies in Cs, Rb, Ba and Pb (fluid-mobile elements) in back-arc basin basalts. The composition of the basalts of the nearby ridges instead shows enrichment in highly incompatible elements.

CHAPTER 2 - GEOLOGICAL SETTING

2.1 Philippine Sea back-arc basin

Along the West Pacific Margin three different tectonics plates, the Pacific, Eurasian, and Indian-Australian plates, interact since about 50Ma, creating a convergent zone of the largest trench-arc-basin systems on Earth, containing 75% of global marginal basins (Quanshu Yan et al., 2022). This is the only region where plate subduction and accretion occur simultaneously (Qin et al., 2011). Located between these three major plates, the small Philippine Sea Plate (PSP)(Fig.4) is one of the largest marginal oceanic plates in Southeast Asia. According to plate reconstruction since the beginning of the Cenozoic, the PSP has moved from Equatorial latitudes more than 2000 km northwards reaching the actual position while rotating clockwise. At 52 Ma, the proto-Izu- Bonin-Mariana (IBM) Arc began to form due to the westward subduction of the Pacific Plate. The present-day Philippine Sea plate is part of different subduction zones: to the west the Ryukyu Trench and the Nankai Trough to the north, the IBM Trench to the east, and the Yap and Palau trenches to the south. These latter represent the convergence zone of the Pacific Plate, the Caroline Plate, and the Philippine Sea Plate, with a total length of over 700 km. These subduction zones are associated with four back arc basins, three inactive and one active, and several remnant arcs.

The back-arc basins include: (i) the West Philippine Basin (WPB) that began its opening at 65 Ma and then stopped at 35 Ma. (ii) the Shikoku Basin (SKB), which is younger than WPB and started the spreading at 27 until 15 Ma. The first spreading period (corresponding to Chron 7-6) have a ENE-WSW motion, the second one (corresponding to Chron 5E-5B) a NE-SW spreading direction (Okino et al., 1994, 1998, 1999), this change in the spreading orientation may have been related to the clockwise rotation of the PSP (Sdrolias et al., 2004). (iii) the Parece Vela Basin (PVB), which has similar age to the SKB, it began opening at 29 also until 15 Ma. Here the tectonic evolution evolved from an initial rifting (29-26 Ma), a subsequent seafloor spreading (23-15 Ma) and a non-magmatic rifting (< 15 Ma) (Okino et al., 1998). (iv) the Mariana Trough (MT), which is the only active back arc basin that started from 5 Ma to present. Coherently with the occurrence of three phases of back arc extension, the PSP include three arc systems which are the (Relic) Kyushu- Palau (Arc) Ridge (KPR, termination at 29 Ma), this arc was disrupted during the rifting and seafloor spreading of SKB e PVB; the (Relic) West Mariana Arc (Ridge) (WMR, termination at 6Ma), the active Izu Bonin Mariana (IBM; since 11 Ma), and Yap (since 24 Ma) Arcs.

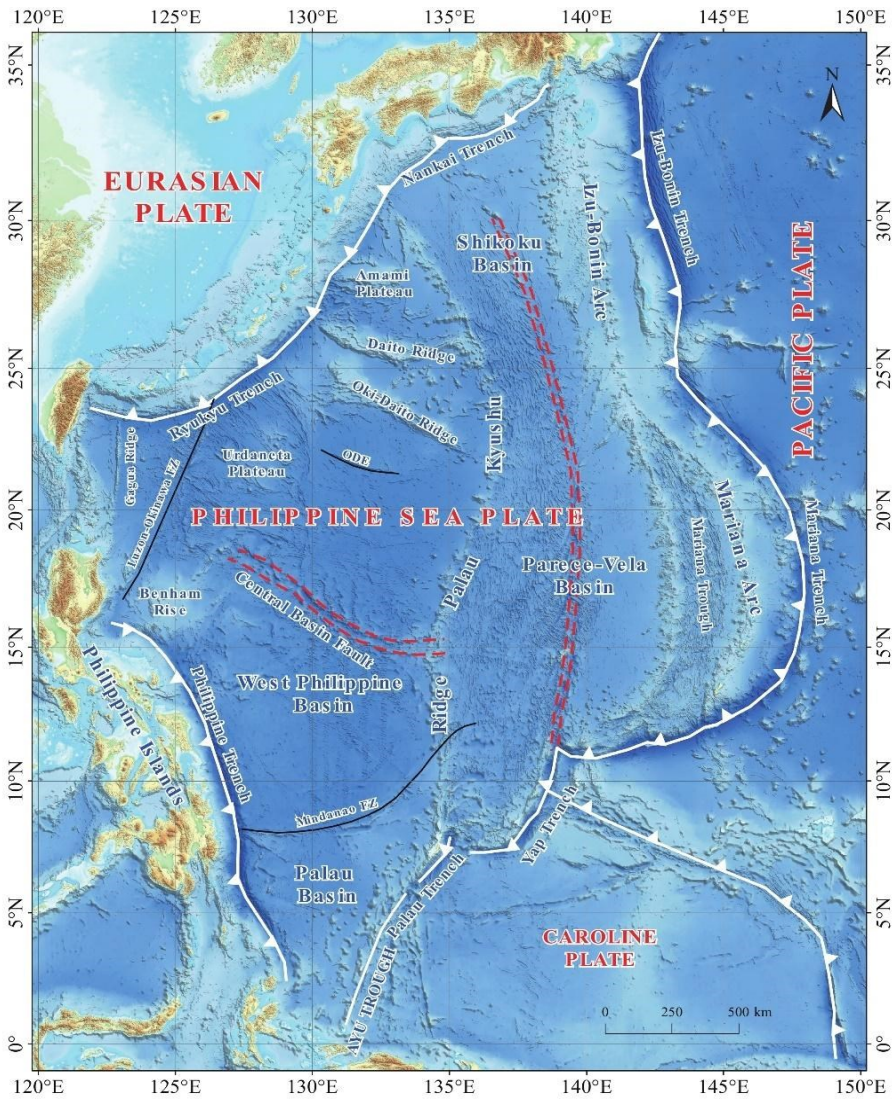

Figure 4: Geotectonic map of Philippine Sea Plate, among Eurasian, Pacific and Caroline Plates in a convergent zone, in South Asia. Red line for ancient spreading centers and white ones subduction zones. Map from Zhang et al. 2022.

The back-arc basins of the PSP have rocks of different types. The WPB basalt compositions range from N-MORB to E-MORB, which agree with the back-arc spreading and intraplate magmatism experienced by the WPB. OIB-like basalts are present in the Benham Rise and Urdaneta plateau (Fig. 1). Basalts from the SKB are mainly BAB basalts associated to lavas with N-MORB to E-MORB affinities (Fig. 5). The BABB and N-MORB are slightly depleted in Nb and Ta, possibly indicating that the mantle source of these lavas was affected by fluids from the subducting slabs (Hickey-Vargas, 1998). The Kinan seamount chain, a group of large volcanic edifices, overlap the extinct spreading centre of the Shikoku Basin, so the seamounts chain is located in the central part of SKB. Kinan seamount chain developed between 7.73 and15.48 Ma at the very end of the SKB expansion, here there are medium to high-potassic alkali basalts that have an OIB-like signature and do not exhibit Nb-Ta depletion. This implies that they are geochemically similar to magmas from

intraplate magmatism, without the input of an active subduction. Similar to the SKB, the PVB also mostly features back-arc basin basalts (BABB) slightly enriched in Rb, K, and Ba with respect to MORB that could indicate a subduction influence on the source. Some basalts have high-aluminum (Al) content with a flat REE patterns and lack Eu anomalies (Fig.6).

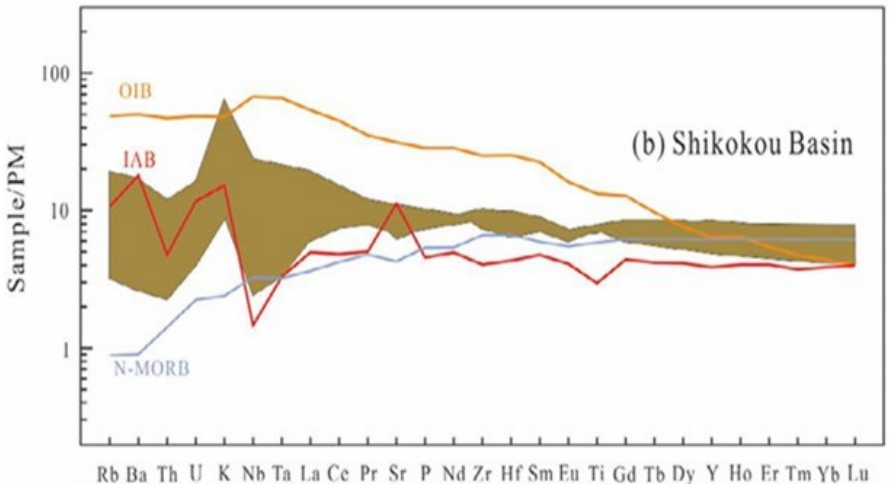

Figure 5: Spider Diagram of Shikoku basin basalts from Dick et al. (1980), Marsh et al. (1980) and Ishizuka et al. (2009).

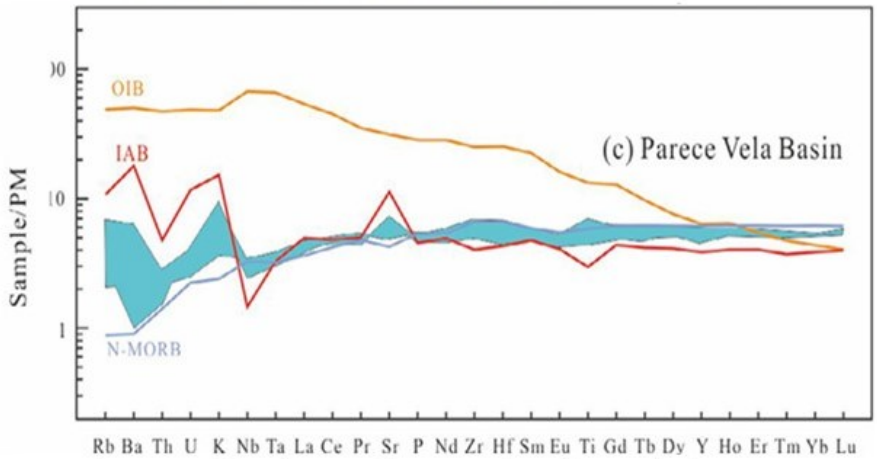

Figure 6: Spider Diagram of Parece Vela Basin samples from Ridley et al. (1974) and Hickey-Vargas (1998).

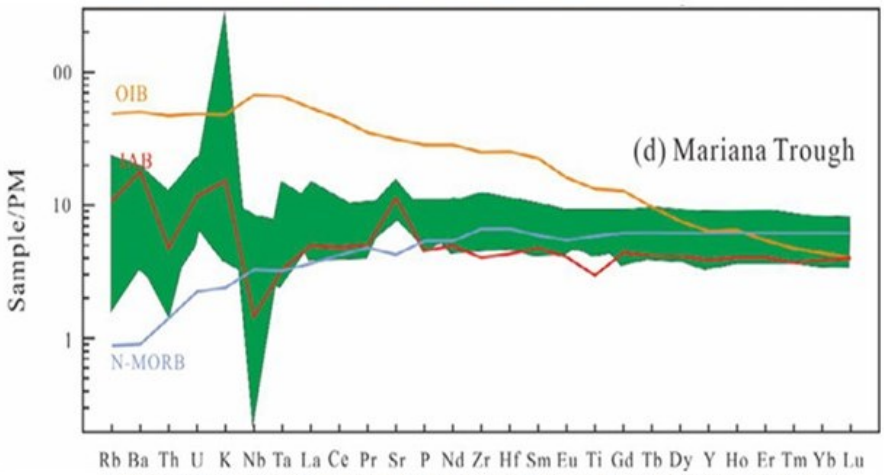

Figure 6B: Spider diagram of Mariana Trough from Volpe et al.(1987-1990), Stern et al. (2006) and Yan et al. (2019)

The Mariana Trough (Fig.6B) mainly contains BABB and island arc basalts (IAB), the latter present in the expansion centre near the island arc. On the other hand, the subaerial volcanism in the IBM arc is composed of forearc basalts with an age of 52- 51 Ma, followed by 49-45 Ma-old boninites (i.e., highly depleted, MgO-rich andesites) and mature island arc magmatic rocks with age <45 Ma. The two relict arcs (the KPR and the WMR) contain mainly IAB-type basalts.

2.2 Isotopic characteristics of Philippine Sea basalts

The basement rocks in the Philippine Sea back-arc basin are isotopically similar to the Indian Ocean MORB. The most diagnostic characteristics are their high $^{208}Pb/^{204}Pb$ (Fig.7c), high $^{87}Sr/^{86}Sr$ and low $^{143}Nd/^{144}Nd$ (ε_{Nd}) (Fig.7b) for given $^{206}Pb/^{204}Pb$. N-MORB and E-MORB-like basalts from SKB have initial $^{87}Sr/^{86}Sr$ of 0.70265 to 0.70338, initial $^{143}Nd/^{144}Nd$ of 0.51311 to 0.51291 (initial εNd = +9.9 to +6.3), and initial $^{206}Pb/^{204}Pb$ of 17.79 to 18.44. OIB-like basalts from SKB have initial $^{87}Sr/^{86}Sr$ of 0.70367-0.70435, $^{143}Nd/^{144}Nd$ of 0.51290- 0.51278 (initial εNd = +6.3 to +4.0), and $^{206}Pb/^{204}Pb$ of 18.60 to 19.35. All the basalts have initial $^{208}Pb/^{204}Pb$ and $^{207}Pb/^{204}Pb$ ratios higher than the Northern Hemisphere Reference Line (NHRL), with delta ^{208}Pb of +33 to +57 and delta ^{207}Pb of +0.4 to +6.8 in MORB and delta ^{208}Pb of +29 to +63 and delta ^{207}Pb of +0.3 to +7.6 in OIB (Vargas 1998). Basalts from SKB and PVB reveal the most depleted isotopic composition, nearly coincident with the Indian MORB, at high εNd and very low Pb isotopes for relatively radiogenic Sr. Samples from Kr Segment or Kyhoshu Ridge are generally enriched in Sr and Pb and seem to cover a wide range of variability from HIMU-like OIB to EM2 compositions (Qian et al. 2024). Samples from WPB are distinct from those in the SKB and PVB in retaining isotopically enriched compositions tending towards the EM2 endmember, in accordance with their derivation from ancient mantle plume (Qian et al. 2024).

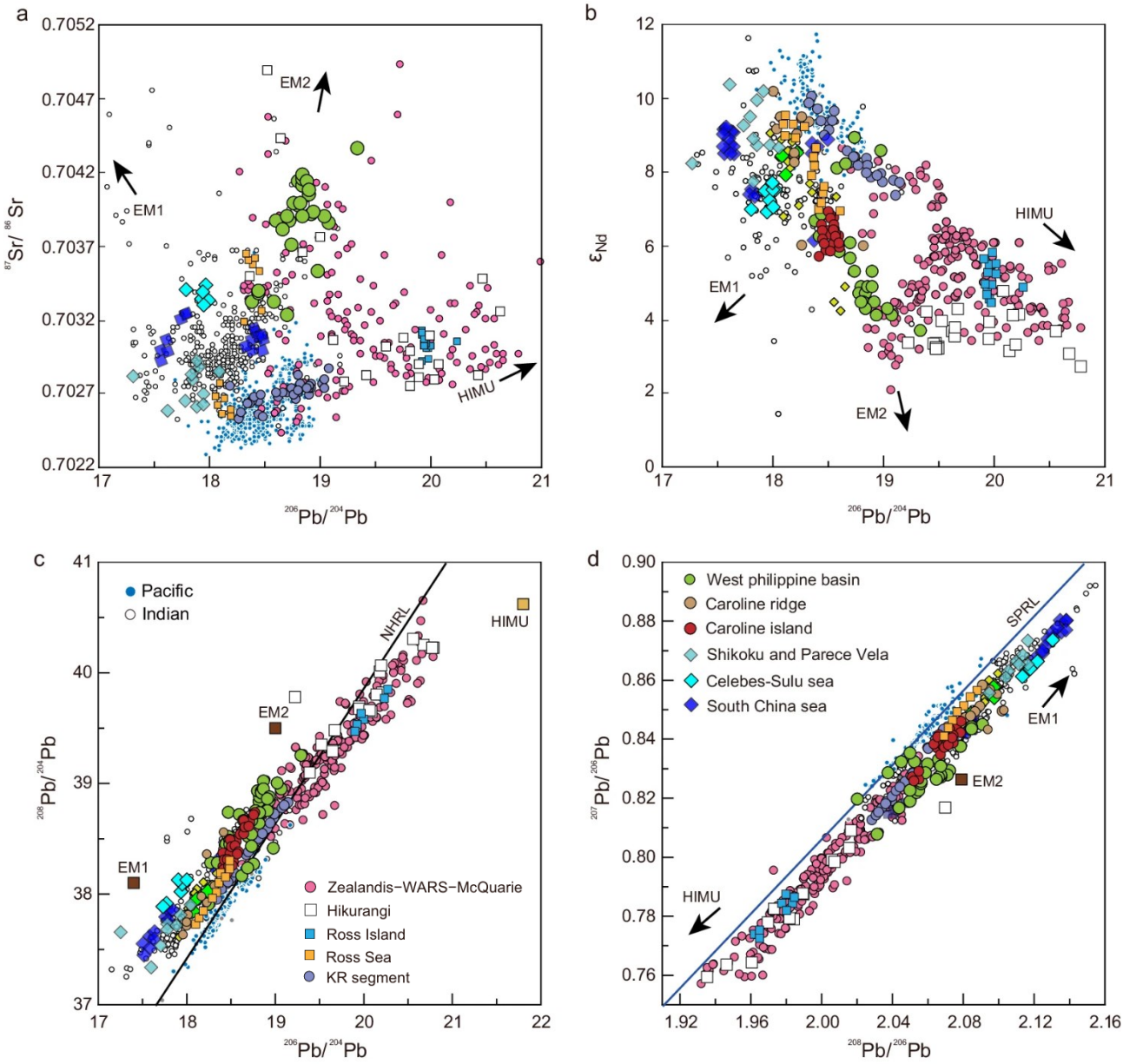

Figure 7: ***Comparisons between isotope ratios from the Philippine Sea plate, mid -ocean ridge segments, and surrounding regions.*** ***a)*** *$^{87}Sr/^{86}Sr$ vs $^{206}Pb/^{204}Pb$.* ***b)*** *εNd vs $^{206}Pb/^{204}Pb$.* ***c)*** *$^{208}Pb/^{204}Pb$ vs $^{206}Pb/^{204}Pb$.* ***d)*** *$^{207}Pb/^{206}Pb$ vs $^{208}Pb/^{206}Pb$. MORB dataset from Gale A., C. A. Dalton, C. H. Langmuir, Y. Su, and J.-G. Schilling (2013); Australian Domain dataset from Park, S.-H. et al. (2019) and Pacif Domain dataset from GEOROC database.*

2.3 Oceanic Core Complexes

Given the complexity of the magmatism in the region, and the sparse geographical distribution of the different subduction and backarc spreading events, this work will take the advantage of examining oceanic lower crust or mantle rocks exhumed through oceanic core complexes (OCCs) in different stage of a backarc basin evolution.

Oceanic core complexes (OCCs) are topographic highs that form by extension and uplift during periods of reduced magma supply, usually at the intersection between a transform fault and a

spreading ridge (Ildefonse et al., 2007; MacLeod et al., 2009; Olive et al., 2010). They represent exhumed footwall of long-lived oceanic detachment faults and are formed by deep-rooted material. The OCC structure is composed of smooth domes that are characterized by spreading-parallel corrugations and high mantle Bouguer anomalies related to the occurrence of lower crustal and mantle material at shallow depths. OCC can vary in size from 10 to 150 km in length, 5 to 15 km in width, and can form domes of thousands of meters in height. The first OCCs were identified along the Mid-Atlantic Ridge in 1997 (Cann et al. 1997), most of the studies of OCCs have in fact been done in this area and along the Southwest Indian Ridge. Since they are both slow and ultra-slow spreading ridges, they mostly present this type of structure. The largest ocean core complex in the world (10 times larger in area than the typical OCC in the Mid-Atlantic Ridge has been identified in 2001 at the back-arc basin Parece Vela, 16°N (Harigane et al., 2008, 2010, 2011, 2019; Loocke et al., 2013; Michibayashi et al., 2014, 2016; Ohara, 2016; Ohara et al., 2001, 2003, 2011; Ohara & Snow, 2009; Sanfilippo et al., 2013, 2016; Spencer & Ohara, 2014; Tani et al., 2011). It is a huge megamullion first named as Giant Megamullion (Ohara et al., 2003) and then renamed as Godzilla Mullion. This structure is 55 km along-segment, 125 km ridge-perpendicular and presents topographic corrugations indicative of long-lived detachment faulting exhuming mantle peridotites, massive gabbroic bodies, diabase, and basalts (e.g., Ohara, 2016). Since the discovery of the Godzilla Megamullion, several oceanographic expeditions were aimed at obtaining a high-resolution survey of the Philippine Sea back-arc, and tens of other OCC were found.

The samples studied in this thesis have been collected at two oceanic core complexes recently discovered in the Shikoku basin: Mado Megamullion located on axis along the central-south part of SKB, and Tosa and Sanuki belonging to the Nankaido OCCs, located in the westernmost area of the SKB in vicinity to the Kyushu-Palau relict arc (Fig.8). As such, these OCC expose lower crustal and peridotite samples formed at different times in the SKB back-arc and can be used to prove its evolution, from the beginning to the end of a back-arc lifetime.

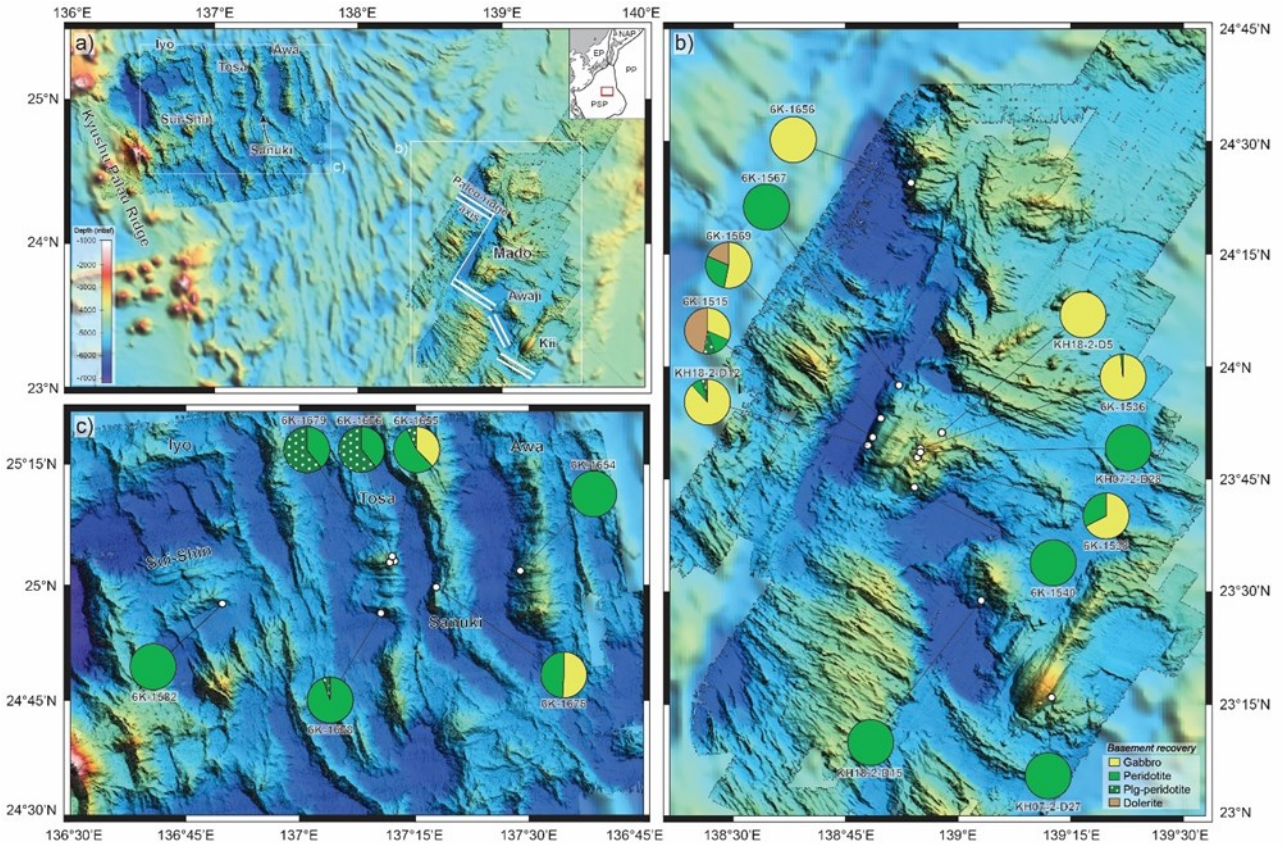

Figure 8: Bathymetry of the southwestern Shikoku Basin, showing the location of Sanuki and Tosa OCCs on the North-West, and of the Mado Megamullion on the South-East and the point of sampling.

2.4 Mado Oceanic Core Complex

The Mado Megamullion (MM) is an OCC recently identified in the southernmost Shikoku Basin and first mapped in 2018 (Ohara et al., 2018). It is located at only 1,300 km from Tokyo, Southeast Japan Coast, ~ 2 days ship transit, therefore it represents an easily accessible tectonic window in the world's oceans, in fact Mado means Window in Japanese. The MM is located at the northeastern side of the extinct axial rift, so in the inside corner of the ridge-transform intersection (23°50′N, 138°50′E), at the junction of two basins (SKB and PVB). The formation (from 14.1 to 12.2 Ma) of the MM is related to the last phase of spreading of the extinct Shikoku back-arc basin, most likely in a period of slow spreading. It has developed at the inside corner of the axial rift, where the spreading axis has been segmented by transform faults at relatively short intervals. One important characteristic is the traces of the final appearance of the back-arc SKB opening leaves by the Mado.

This domal massif has spreading-parallel corrugations extending for 24 Km from the breakaway to the termination, with a total extent of the corrugated surface of ~500 Km^2 (Fig.9a). The breakaway is ~ 30 Km from the relict axial rift, while the termination which represents the detachment fault

hanging wall cutoff, continues to the axial rift valley, suggesting that the detachment faulting continued until the end of the back-arc basin opening (Okino et al. 2023).

The OCC is wider at the breakaway and narrowed showing a steep slope toward the termination; this shape may be related to the different magma supply. The magma budget parameter (M) is given by the ratio between the magmatic input and the tectonic accretion. For an M=0.5 (intermediate value) the magmatic input reaching the surface can occupy half the space created by the stress. The deformation is stable and concentrated along the detachment fault. Okino et al. (2023) predicted by numerical modelling a M ~ 0.5 during the detachment dominant phase, that exhumed MM. The length and width of the Mado are 23 and 25 km, respectively. It is similar in size to most OCCs documented at the Mid-Atlantic Ridge and Southwest Indian Ridge.

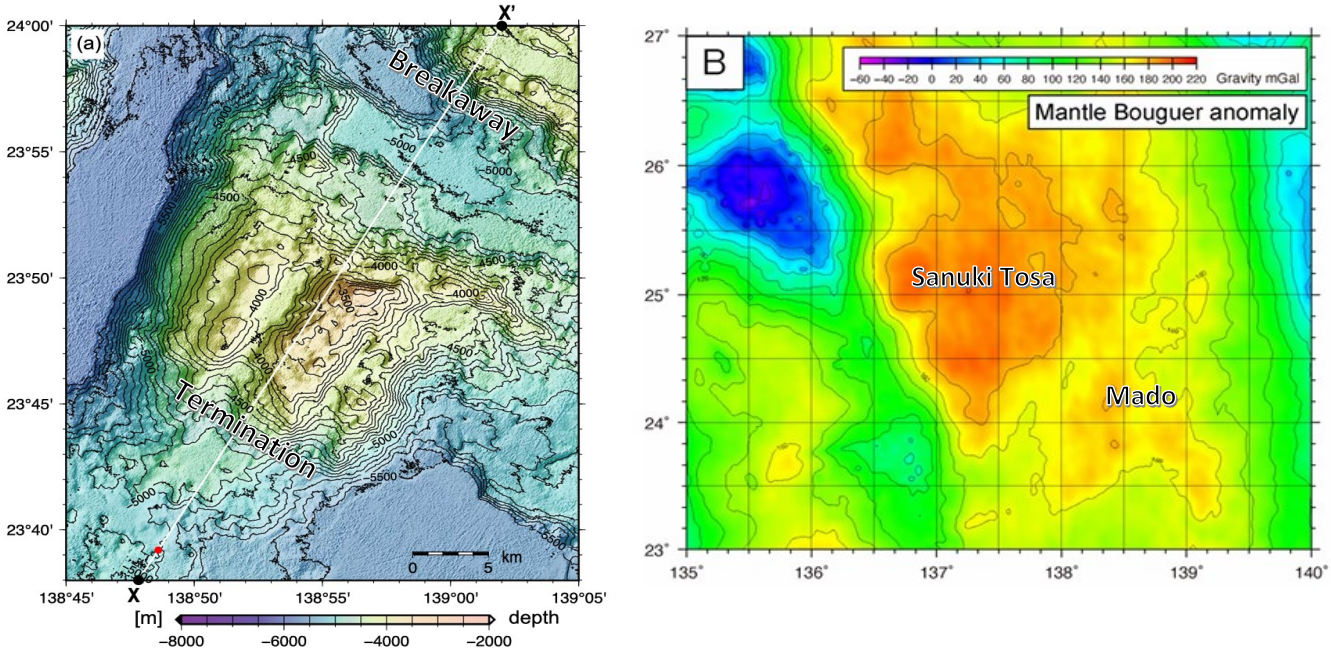

Figure 9: a) Close-up view of the Mado MM OCC. The contour interval is 20 m. From Okino et al. (2023); b) Mantle Bouguer anomaly map of the southwestern Shikoku Basin. From 2023_YK23-05S_Report.

The gravity anomaly analysis shows positive mantle Bouguer anomalies (Fig.9b), ~ 20 mGal larger than the surrounding area (Ohara et al., 2018; 2019; 2023). This MBA value corresponds to a 3.4 km decrease in magmatic crust or a 270 kg/m3 decrease in density. The weaker positive MBA area extends to the eastern part of the Mado segment, where the seafloor is relatively deep and flat without any corrugation. This high positive gravity anomaly is due to the lower crust/mantle materials exposition along the detachment.

Regarding the lithologies, sample collection includes serpentinized peridotites, variably evolved and deformed gabbroic rocks, and minor pillow basalts and decimeter-size doleritic intrusions.

Zircon U–Pb age analyses conducted on zircons separated from gabbroic rocks reveal ages ranging from 11.74 ± 0.61 Ma to 12.96 ± 0.30 Ma. (Okino et al.2023). The petrology of the gabbros and peridotites has been reported by Basch et al. 2020 and Akizawa et al. (2021) and Sen et al. (2021) which will be detailed in the next chapters. The rocktypes are similar to and follow a compositional trend close to that of MOR gabbros, with particular similitudes to the Atlantis Bank in the Southwest Indian Ridge (SWIR). The most critical finding is the widespread occurrence of amphibole having a wide compositional range, from tremolite to pargasite in many samples (peridotite, oxide gabbro and olivine gabbro).

2.5 Nankaido OCCs group: Tosa and Sanuki

Tosa and Sanuki are part of Nankaido Megamullions located at ~25ºN in the western part of the Shikoku Basin (Fig.8). The Western Shikoku Basin OCCs comprehend numerous OCCs, but until now just five have been mapped, including Tosa and Sanuki. The names are old district names of Honshu Island, Japan, and they were first used to indicate the entire area now known as Nankaido. Successively, scientists decided to Tosa and Sanuki for individual OCCs. The first high resolution bathymetric survey of Tosa (Fig.10B) and Sanuki was carried out during cruise YK-22-18S, in 2022.

Tosa Megamullion presents an east-dipping and steep termination (Fig.10A), covered with sediment and scattered rubbles of plagioclase bearing peridotite and gabbro. The potential breakaway area (Fig.11A), that is the southwestern slope of this topographic high, is also east-dipping and it is steeper upward with landslide features. Sampling conducted here shows a part of muddy sediment peridotite ultramylonite and plagioclase bearing peridotite. The entire east-dipping and spreading-parallel corrugated surface of Tosa Megamullion consists of relatively fresh peridotites and plagioclase bearing peridotite, suggesting that this massif is poorly magmatic and exposes a tectonic block consisting mostly of uplifted mantle. Differently, the western steep slope of the breakaway area of Sanuki Megamullion (Fig.10A) is generally covered with muddy sediment and mainly presents higher amount of mafic rocks, also associate with peridotites. Same as for Tosa, Sanuki Megamullion represent a tectonic block exhuming deep crustal and mantle rocks due to the detachment faulting. As a result, the entire Nankaido area presents high mantle Bouguer anomaly 20 mGal (Fig.9b), in accordance with abundant mantle material recovered.

The areal extent of all the Nankaido Megamullions range from ~22 Ma to ~20 Ma crust (Okino et al. 2015). Hence, these massifs allow to understand the early lithospheric evolution of the SKB backarc basin from rifting stage (corresponding to Sui Shin Megamullion) to mid-term spreading stage (corresponding to Awa Megamullion) (Fig. 8). To date, there is no petrological data on the peridotites nor on the gabbros from the Nankaido Megamullions, but it should be noted that the

occurrence of large amounts of plagioclase-peridotite with much lesser number of gabbros, suggests that this area was nearly a-magmatic, and that melt entrapment occurred beneath the cold thickened lithosphere. Given the magnetic age of the lithosphere in this area of the Shikoku basin, the lithospheric thickening should have occurred right after the initial rifting stage of back arc opening. These poorly magmatic terrain thereby represents the so-called "Hess Model"-type oceanic crust, consisting mostly of peridotite with the MoHo representing an alteration front. This has led scientists to indicate the Tosa Megamullion, with a shallowest depth of ~4100 m, as an ideal location for scientific drilling aimed at recovering a continuous section of backarc mantle.

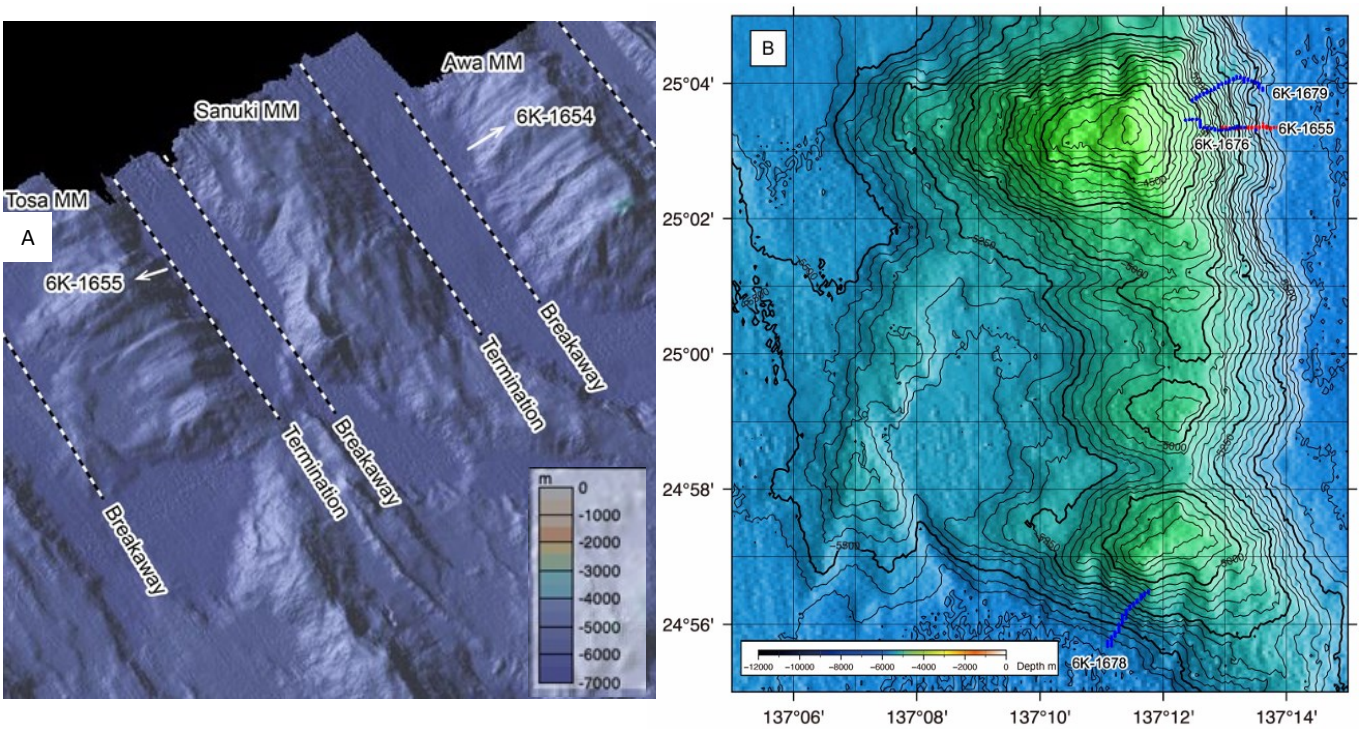

Figure 10: A) Bathymetric 3D map (looking from southwest) showing Tosa and Sanuki breakaway and termination; B) Bathymetric map of Tosa. Contours in 100 m. Shallowest depth ~4100 m.

CHAPTER 3 - SAMPLE SELECTION AND ANALYTICAL TECHNIQUES

3. Sample selection

Twenty-four samples have been selected for this work thesis, collected during five different oceanographic expeditions on board the R/V Yokosuka (JAMSTEC). Most samples were collected during dives by HOV Shinkai 6500, with exception of 3 samples recovered by dredging (D05 and D12).

The cruises were carried out: in June 2018 (YK18-07S); April 2019 (YK19-04S); October-November 2020 (YK20-18S), in October 2022 (YK22-16S), April 2023 (YK23-05S). Each expedition sampled in different areas of the Shikoku Basin, in 2018 at the transform fault walls in the Parece Vela, in 2019 at Shikoku Basin Oceanic Core Complex (MM, NTO, 23º20'N OCC), in 2020 Mado Megamullion (MM), in 2022 and in 2023 at Nankaido OCC in the Western SKB, including Tosa and Sanuki (Fig. 8). Below the table [Tab.1] we report the samples selected for this project. The name of the sample consists in the cruise name followed by the type of sampling technique (dredging or submarine, i.e. D or 6K) and dive or dredge number followed by rock number (R). The sample is also associated with the coordinates of the exact sampling point (latitude and longitude) and the recovering depth (m).

Table 1: name, location and estimated age (Ma) of the different samples selected for this study.

Sample name	Sampled Area	Depth (Km)	Latitude	Longitude	Age
AYK19-04S-6K-1536R10	Mado central	3,76	23°49.8219′N	138°56.7271′E	12,5
YK19-04S-6K-1536R14B	Mado central	3,608	23°49.7226′N	138°56.6931′E	12,5
YK19-04S-6K-1536R16	Mado central	3,608	23°49.7226′N	138°56.6931′E	12,5
YK19-04S-6K-1536R18	Mado central	3,54	23°49.6782′N	138°56.6738′E	12,5
YK19-04S-6K-1536R20	Mado central	3,498	23°49.6532′N	138°56.6656′E	12,5
YK19-04S-6K-1536R20F	Mado central	3,498	23°49.6532′N	138°56.6656′E	12,5
KH18-2-D05R101A	Mado central	4,522	23°51.7310′N	138°57.8930′E	12,5

KH18-2-D05R101F	Mado central	4,522	23°51.7310′N	138°57.8930′E	12,5
YK18-07S-6K-1515R04	Mado near Transform Fault	5,599	23°50.6100′N	138°47.9940′E	12,5
YK18-07S-6K-1515R14	Mado near Transform Fault	5,073	23°50.4372′N	138°48.3942′E	12,5
YK20-18S-6K-1569R07B	Mado near Transform Fault	5,422	23°53.3168'N	138°49.4689'E	12,5
YK20-18S-6K-1569R08A	Mado near Transform Fault	5,422	23°53.3168'N	138°49.4689'E	12,5
YK20-18S-6K-1569R09	Mado near Transform Fault	5,308	23°53.2839'N	138°49.5291'E	12,5
KH18-2-D12R111	Mado near Transform Fault	5,403	23°49.3060′N	138°47.6350′E	12,5
YK22-16S-6K-1655R02	Tosa	5,592	25º3.3599'N	137º13.6145'E	21
YK22-16S-6K-1655R05	Tosa	5,485	25º3.3425'N	137º13.4834'E	21
YK23-05S-6K-1675R02A	Sanuki	5,532	24º59.2755'N	137º16.9279'E	21
YK23-05S-6K-1675R02C	Sanuki	5,532	24º59.2755'N	137º16.9279'E	21
YK23-05S-6K-1675R02B	Sanuki	5,532	24º59.2755'N	137º16.9279'E	21
YK23-05S-6K-1675R02F	Sanuki	5,532	24º59.2755'N	137º16.9279'E	21
YK23-05S-6K-1675R10A	Sanuki	4,923	24º58.9624'N	137º17.4552'E	21
YK23-05S-6K-1675R11	Sanuki	4,923	24º58.9624'N	137º17.4552'E	21

3.2 Analytical techniques

This section includes a description of the analytical methods used for a series of analysis performed on selected samples (n=24). The performed analyses were: *i)* petrographic analysis under the optical microscope and *ii)* Sr-Nd-Pb isotope compositional analyses using Thermal Ionization Mass Spectrometry (TIMS). In order to perform these characterizations and measurements, the samples followed several phases of preparation including the preparation of thin sections for observation using the optical microscope, the separation of minerals or rock powders; the dissolution and purification through ion exchange columns, and the isotopic determination by TIMS. Laboratories used during this project were 1) the thin section and rock preparation laboratory of DSTA for samples cutting, crushing, separation and weighing of the mineral separates, 3) the 'Filippo Olmi Laboratory' and and 'MEMA' (electron microscopy and microanalysis) at the department of Earth Sciences of the University of Florence, for preparation of the purified fractions of Sr, Nd and Pb in clean labs, and isotopic analyses using TIMS.

3.2.1 Optical microscope study

The petrographic analysis allows to identify the minerals composing the samples and their petrographic characteristics, in order to identify the different lithologies described in section "*5. Results*".

The samples previously recovered and processed into thin sections were analysed petrographically using Nikon Eclipse E400 polarized optical light microscope (Fig.12) with magnifications of 2x, 4x, 10x and 20x. The thin sections have a thickness of ~50 µm and are attached on a glass slide and are polished to allow for the passage of light through the sample. The light is polarized by the Nicol prism (polarizer), in a way that the electric field vector of the source is forced to vibrate mainly or exclusively on a single plane (Fig.13a). Specifically with parallel Nicol, this calcite prism polarizes by double refraction, i.e. of the two rays produced by the doubling (bi-refraction phenomenon(Fig.13b): the light ray crossing an anisotropic body is doubled) of the non-polarized beam, one is completely reflected and the other refracted.

Figure 12: Nikon Eclipse E400 POL microscope.

With crossed Nicols, an analysing prism is added to the polarizer, which blocks the single component of the light coming out of the polarizer, allowing observation of the interference colours (Fig.14). Interference colours are not related to the colour of the mineral seen with the naked eye. These are formed by the interference (waves with the same amplitude and wavelength have a phase difference)

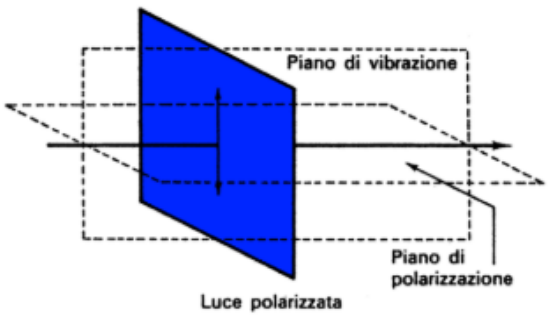

Figure 13a: Schematic representation of a polarized light on a preferential plane of vibration.

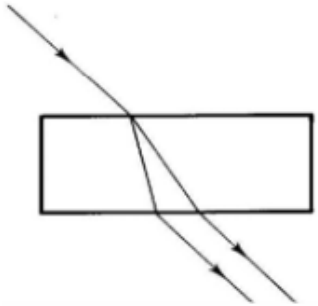

Figure 13b: Schematic representation of birefraction of a ray passing through an anisotropic material.

of the ordinary ray (follows Snell's law) and extraordinary ray (does not follow Snell's law, and it is always orthogonal to the ordinary ray)[1] which they travel at different speeds in the material. When they arrive on the analyser the rays recombine, giving rise to different interference colours.

Other petrographic characteristics established thanks to microscopic analyses are the natural colours defined by the combination of colours not absorbed in transmission/reflection by the material, this

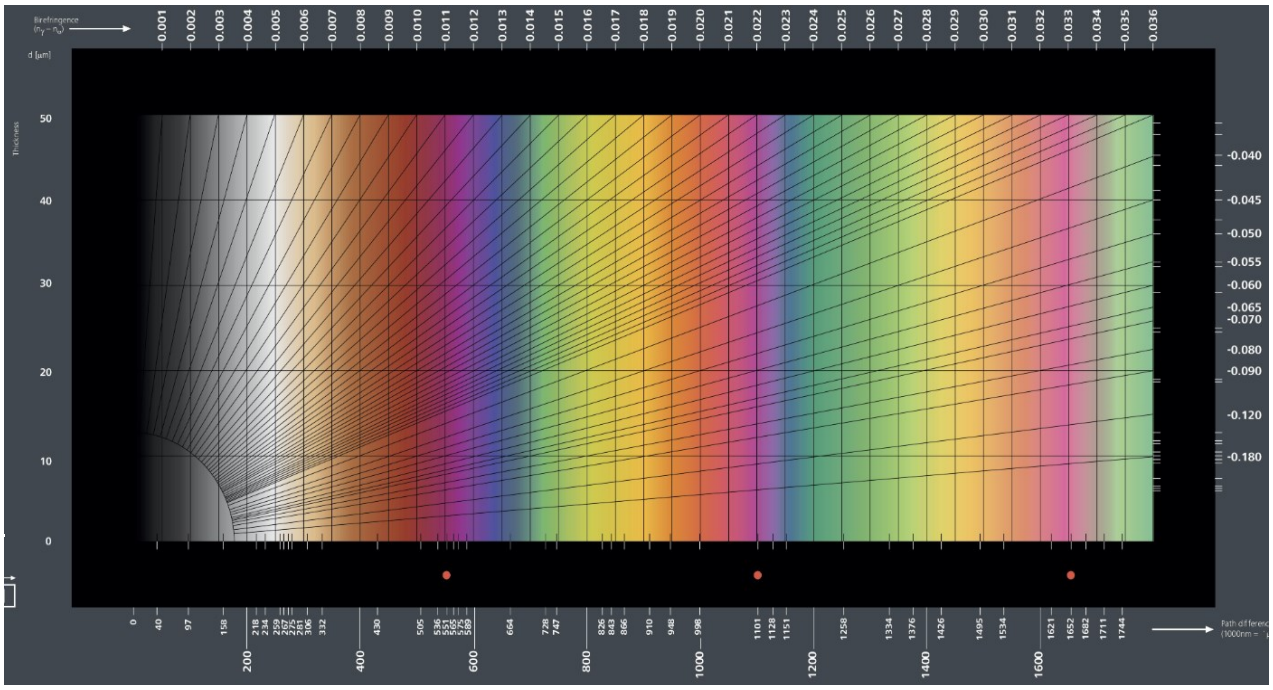

Figure 14: Michel-Lévy Interference Colour Chart used to identify minerals observed in crossed Nicols on an optical microscope. The interference (difference of wavelength, λ, increase from right to left.

[1] Snell's law which governs the phenomenon of refraction: (sin i) / (sin r) = n1 2 = V1 / V2 (n1 2 = refractive index of medium 2 with respect to medium 1) v = velocity of propagation in the medium.

phenomenon is called selective absorption, meaning that some frequencies of the visible spectrum are absorbed more than others. This colour can vary based on the direction of observation, this is a phenomenon called pleochroism, which can be more or less accentuated. Pleochroism occurs because in anisotropic materials the light is absorbed differently depending on the direction with respect to that of the electric field of the polarized incident beam. The relief was also established, given by the 'overhanging/projection' effect of the granule compared to the surrounding medium. It can be strong or weak depending on the difference between the refractive indices of the two media. Additionally, a series of morphological characteristics of the minerals identified within the sample, such as grain size, crystalline habit, extinction (i.e., the variation of the refractive index with the direction, which is visualized with the extinction of the mineral by rotating the sample stage), flaking, microfractures. It was also possible to evaluate the deformation (mylonitic bands, recrystallization edges, phenocrysts and neoblasts), the degree of alteration and the presence of microstructures (e.g. veins). The identification of the optical and petrographic characteristics of each mineral allowed their recognition, therefore, for each sample in thin section, the mineralogical modal composition was estimated, expressed in vol%, for the following minerals: olivine, plagioclase, pyroxene, magmatic amphibole and Fe-Ti oxides.

Polarized light microscopy represents a valid and fundamental investigation method. It provides a non-destructive way to identify solid substances with relatively high spatial resolution, while phases can be studied within their structural framework. It allows to identify minerals and provides clues to their formation history, using specific textural characteristics such as structure, fabric, phase assemblage, phase relationships, reaction textures.

3.2.2 Sr-Nd-Pb isotope determinations

The primary application of the characterization of radiogenic isotope ratios are in geochronology and in tracer studies. Radiogenic isotopes refer to isotopes (daughter) that form by the decay of long-lived radioactive isotopes (parents). More precisely, radioisotopes are various species of the same chemical element with different masses whose nuclei are unstable and dissipate excess energy by spontaneously emitting radiation (decay). They can be successfully used to characterize mantle reservoirs, crust-mantle differentiation processes, and mantle melting processes.

If we consider ^{87}Sr as an example, it's known that this is generated by the decay of ^{87}Rb in a defined time:

$$^{87}\mathrm{Rb} \rightarrow {}^{87}\mathrm{Sr} \quad (\lambda = 1.42 \times 10^{-11}\mathrm{years}) \qquad {}^{87}\mathrm{Sr} = {}^{87}\mathrm{Rb}\left(e^{\lambda t} - 1\right) \quad \text{[Eq.1]}$$

[Eq.1] describes the production of ^{87}Sr by decay of ^{87}Rb. However, usually it is not known how much ^{87}Rb was contained at the very beginning of the geochemical system, therefore the solution is given by relating both compositions to the content of stable ^{86}Sr, because this was not caused by decay, in the following way [Eq.2].

$$\frac{^{87}Sr}{^{86}Sr} = \frac{^{87}Rb}{^{86}Sr}(e^{\lambda t} - 1) \approx \frac{^{87}Rb}{^{86}Sr}\lambda t \qquad \text{[Eq.2]}$$

The $^{87}Sr/^{86}Sr$ isotope ratio in a system is a linear function of the parent/daughter chemical ratio Rb/Sr and a quasi-linear function of time or the geological age of the system. Through this study method, Hurley and co-workers, in the early 1960s, were able to distinguish crustal magma sources from those located in the mantle on the basis of their initial strontium-isotopic compositions (Hurley et al.,1962). Subsequently, studying isotope ratios in MORB and OIB several authors realized that $^{87}Sr/^{86}Sr$, $^{206}Pb/^{204}Pb$, $^{207}Pb/^{204}Pb$, and $^{208}Pb/^{204}Pb$ increase as functions of time, and their respective radioactive-parent/non radiogenic daughter (stable isotope) ratios, $^{87}Rb/^{86}Sr$, $^{238}U/^{204}Pb$, $^{235}U/^{204}Pb$, and $^{232}Th/^{204}Pb$, increase in the sources of the magmas. This result led to the discovery that the mantle must contain old reservoirs with different time-integrated Rb/Sr, U/Pb, and Th/Pb ratios. This application provides general chronologic information (model ages), constrains of interactions between geochemical reservoirs, up to the mantle source type identification. The most commonly used radiometric systems are: U-Th-Pb, Rb-Sr, Sm-Nd, Lu-Hf, Re-Os, U series disequilibrium, as resumed in table 2.

Parent nuclide	*Daughter nuclide*	*Half-life (years)*	*Tracer ratio (radiogenic/nonradiogenic)*
^{147}Sm	^{143}Nd	106×10^9	$^{143}Nd/^{144}Nd$
^{87}Rb	^{87}Sr	48.8×10^9	$^{87}Sr/^{86}Sr$
^{176}Lu	^{176}Hf	35.7×10^9	$^{176}Hf/^{177}Hf$
^{187}Re	^{187}Os	45.6×10^9	$^{187}Os/^{188}Os$
^{40}K	^{40}Ar	1.25×10^9	$^{40}Ar/^{36}Ar$
^{232}Th	^{208}Pb	14.01×10^9	$^{208}Pb/^{204}Pb$
^{238}U	^{206}Pb	4.468×10^9	$^{206}Pb/^{204}Pb$
^{235}U	^{207}Pb	0.738×10^9	$^{207}Pb/^{204}Pb$

Figure 15: Table 2, main radioactive parents and radiogenic daughter, half-life decay and they relationship.

3.3 Sample preparation for isotopic analyses

For the isotopic analyses, the samples were previously subjected to distinct preparation phases: crushing (1), hand picking (2), leaching (3), dissolution and chromatographic separation with exchange ions chemical columns for Sr, Nd and Pb (4). As for all geochemical analyses, care must be taken to preserve sample integrity from the time of preparation through analysis in all steps.

The crushing (1) was carried out at the Department of Earth and Environmental Sciences from the University of Pavia. The instrument used was the Retsch model BB50 jaw crusher (Fig.16), which crushed with a speed of 600 rpm set for all samples. The particle size reduction was carried out in various steps depending on the sample, starting from 10-15 mm until obtaining particles of 0.2 mm for all samples (n = 24). After grain reduction, the samples were sieved at 500 microns, in order to remove the finest portion, possibly associated with alteration. The granulate was also placed in contact with a magnet in order to remove the oxides where present to facilitate the following handpicking step. At this point, using a microscope and tweezers (2), from the granulate fragments were separated primary amphibole crystals for 5 samples and fragments of clinopyroxene crystals for 13 samples; for the remaining 4 samples the handpicking phase was not carried out, since the analyses are to be carried out on the whole rocks. Both the separate and the bulk rocks were weighed with an analytical balance, taking from 0,1 to 0,6 gr for the amphibole and clinopyroxene crystals and ~ 1 gr for the whole rock samples.

Figure 16: Retsch BB50 jaw crusher used for samples preparation.

The leaching, dissolution and chromatographic separation operations were carried out at the Department of Earth Science of the University of Florence, consisting of a fine chemistry laboratory (clean room) (Fig.17a) with ”class *1000*“ air treatment, over pressurized (10 Pa) and thermally conditioned (20°C). It is equipped with partially aspirated ”*class 100*“ laminar flow workbenches/hoods which ensure an atmosphere with a low particulate (fine dust) content, allowing sample contamination to be reduced to a minimum.

The sample dissolution (3) was done on all samples at atmospheric pressure with concentrated HF-HNO^3 acid, at 150° for 48h. HNO^3 promotes oxidation and the formation of nitrates/leachates, while HF brings cations into solution which form perchlorates/nitrates of Ca, Na, etc. This process allows the removal of the silicate matrix but also causes the loss of volatiles. For evaporation and nitrates/leachates dissolution, 10 to 20 ml of 6M HCl acid were added to the samples at 170° for 48h. Specifically, for samples <500 mg, 10 ml were added, for those >500 mg, 20 ml of acid were added. This evaporation step for the separated samples was performed 3 times. Once evaporation was completed, the samples were split into 3 parts: 1/50 used for the analysis of major elements and trace elements with ICP-MS for age correction; 20-30% used for the Sr, REE and Nd chemical collection columns; 70-80% used for chemical Pb collection columns. It was decided to use a greater quantity

of material to facilitate the collection of Pb as it is present in quantities (ppb concentrations) much lower than the content of Sr and Nd in the separated crystals.

The liquid chromatography (4) to isolate elements of interest involves several steps:

- Chemical column AG 50W8 hydrogen-form resin for Sr and REE collection (Fig.17b):
    - conditioning with 25 mL HCl 2.5N (the night before)
    - sample centrifugation to separate any solid residue
    - sample loading 0,5 mL (in HCl 2.5N)
    - acid addition:
      0,5 mL HCl 2.5N (x2)
      17 mL HCl 2.5N
    - inserting Teflon beaker collection and addition 10 ml HCl 2.5N

The steps above allows to discard the elements not of interest and to collect all the Sr isotopes present within the sample thanks to the resin present in the columns and the acids used, however the chemical column continues for the REE collection:

- 4 mL HCl 6N to clean the column
- 8 mL HCl 6N to collect REE
- cleaning
  25 mL HCl 6N
  15 mL H2O (next morning)

These last steps are used for the REE collection (left at 140° overnight) from which we will start for the Nd collection.

- Chemical column Ln- Spec HDEHP resin for Nd collection (Fig.17c):
    - cleaning 3,5 mL HCl 6N
    - conditioning
      2 mL HCl 0.18N
      1 mL HCl 0.18N (x2)
    - sample loading 0,3 mL (in HCl 0.18N)
    - rinsing 0,15 mL HCl 0.18N (x3)
    - eluting 16 mL HCl 0.18N
    - Nd recover inserting Teflon baker and adding 4 mL HCl 0.3N
    - cleaning
      4 mL HCl 6N
      1 mL HCl 0.18N
    - column storage 1 mL HCl 1N

The steps above allow to discard the elements not of interest and to collect all the Nd isotopes present within the sample thanks to the resin present in the columns and the acids used.

- Chemical column AG1 anion exchange resin for Pb collection (Fig.17d):
  - filling Teflon column with 0,3 mL resin
  - cleaning residues

    0,5 mL HCl 6N (x2)

    0,5 mL MilliQ (x2)

    0,5 mL HCl 6N

    0,5 mL MilliQ
  - pre-conditioning 0,5 mL HBr 0.7N
  - sample loading 0,5 mL (in HBr 0.7N)
  - rinsing

    0,5 mL HBr 0.7N (x2)

    0,3 mL HBr 0.7N (x2)

    0,3 mL HCl 3N
  - elution 0,5 mL HCl 6N

In this process HBr acid is used to ensure that the lead present in the samples sticks well to the resin. The step prior to collecting the Pb instead involves HCl acid because it allows all the Pb to be detached from the resin.

The last step after each chromatographic separation involves neutralization with 50 microliters H2O2 - HNO3, at 150° C x 2h, to remove possible resin contamination within the recovered material which would retain most of the isotopes of the sample. The last actual step before the analyses at TIMS involves the dilution of the collected material with 2N HNO3.

The three chemical columns have different characteristics. Those for the collection of Sr are glass columns with dry resin inside; those for the collection of Nd in the same way are made of glass and have the resin inside them, however they are stored by putting 6N HCl inside them and the capillary part is inserted into tubes full of the same acid, in order to always keep the resin wet ; those for the collection of Pb are handmade in Teflon and much smaller in size, these are stored inside tubes full of 6N HCl, before being used they are therefore emptied, rinsed with MilliQ water and then manually filled with resin, finished the collection the columns are cleaned and reinserted into the tubes. A common feature of all three columns is the quartz wool filter placed at the end of the capillary.

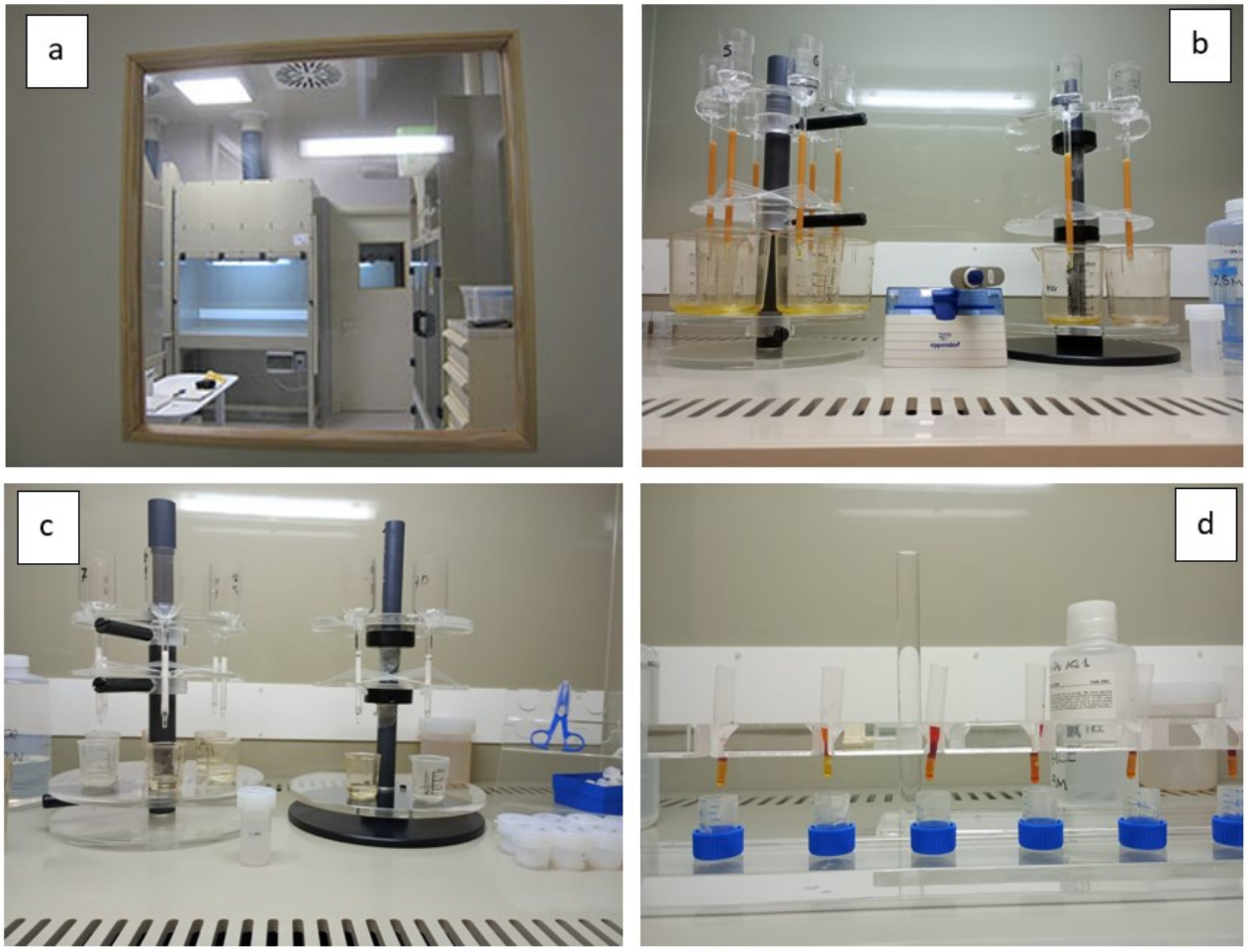

Figure 17: a) fine chemistry clean room; b) AG 50W8 for Sr and REE collection; c) Ln- Spec HDEHP for Nd collection; d) AG1 for Pb collection

Part of the collected material (~150 ppm) for each isotope for each sample is loaded onto a high purity rhenium filament previously manually soldered onto the filament holder (Fig. 18), the latter is subsequently positioned on a sample turret which normally has 10 to 20 filament assemblies. The filaments have pins that are passed through by current to heat the filament to which the sample is attached, so that the isotopes evaporate from it and then ionize. To increase the ionization of some elements, a drop of chloride is used for Sr, a silica gel for Pb, while for Nd a double filament is used, in front of the one on which the sample is attached there is an empty filament which is heated to encourage ionization.

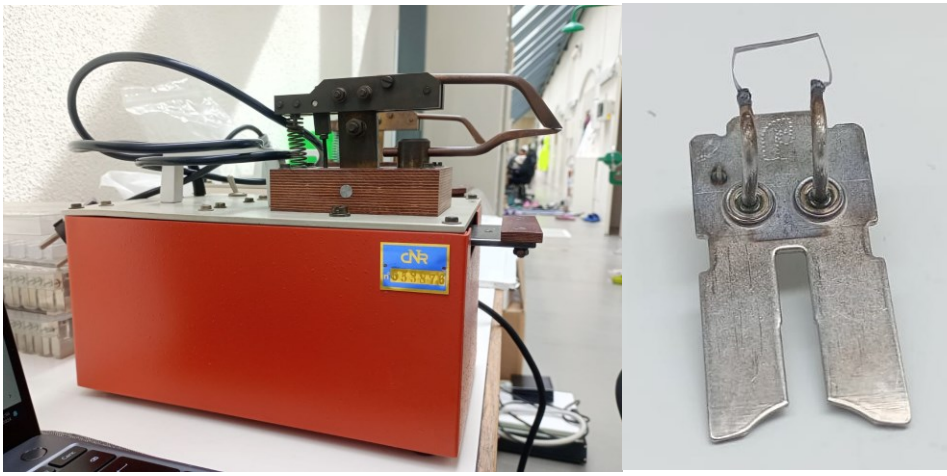

Figure 18: Soldering tool and holder for high purity rhenium filament.

3.2.1 Thermal ionization mass spectrometry (TIMS)

Analyses of Sr, Nd and Pb isotopic ratios were performed at the Department of Earth Sciences (University of Florence) using the Thermal Ionization Mass Spectrometer (TIMS) Thermofisher Scientific Triton Plus (Fig.19).

Figure 19: Thermal Ionization Mass Spectrometer (TIMS) Thermofisher Scientific Triton Plus.

The TIMS is equipped with 9 mobile Faraday collectors and 1 electron multiplier (SEM) with RPQplus (Retarding Potential Quadrupole lenses) filter for the measurement of very low intensity signals. It is also equipped with 4 x 10^{13}ohm amplifiers for optimized determination of the signal/noise ratio on low intensity signals (such as ^{204}Pb). The amplifiers follow the law V = I x R. The sample turret has 21 positions, and the collectors have linearity extended from 0 to 50V. There is a system that allows the "virtual rotation" of the amplifiers on each Faraday collector, and a system

of additional electromagnetic lenses (Zoom Optics) to ensure maximum overlap of the peaks during the analysis in dynamic mode. The magnet has an effective dispersion of 810 mm and a maximum mass difference of 16% which allows the measurement of isotopes at mass unit intervals for elements from Lithium to Uranium. This is an instrument capable of making very precise measurements of isotope ratios of elements that are ionized thermally; filaments are in a vacuum that can reach temperatures anywhere from 400-2300°C, usually by passing a current. The ions created are accelerated by an electrical potential (10 kV) and focused into a beam via a series of lenses and electrostatically charged plates. This ion beam then passes through a magnetic field and the original ion beam is dispersed into separate beams on the basis of their mass to charge ratio. These ion beams are then directed into collectors and converted into voltage. Comparison of voltages yields precise isotope ratios.

Therefore, TIMS is characterized by four main components (Fig.20): 1) ion source capable to produce, with a very small kinetic energy spread (~0.5) eV, ions from the recovered element of the sample; the evaporation, by heating, allows the suction by a very high vacuum flight tube which channels the ion beam towards the 2) analyser, it is a magnet capable of sorting the same isotopes based on mass/charge ratios; 3) the collector is a central Faraday cage, made up of various electronic cards, able to count the signal emitted by the isotopes measured either sequentially; electronics cards must operate to very close tolerances in order to produce isotope ratios with 0.01-0.001% accuracy; finally the entire instrument is associated with a 4) software, that allows automated sample manipulation and automated or configurable measurement procedures, and filament heating programs; then data package such as results in spreadsheet or graphical form are available both on-line and off-line.

For each analysis, an international standard is also measured (example: G-2 which is a granite, BHVO-1 which is an Hawaiian Basalt, RGM-1 which is a rhyolite) of which the concentrations of Sr, Nd and Pb are known with certainty as a reference for correctness of measurements.

Once the analyses are completed, an average of the measured values is obtained (stable and unstable isotopes). For evaporation it is necessary to carry out a fractionation correction using the ratio of the stable isotopes (e.g. $^{88}Sr/^{86}Sr$) present in nature of which there is absolute certainty, applied to the other unstable isotopes.

The use of TIMS compared with other isotope ratio techniques is very advantageous due to the chemical and physical stability of the measurement environment, the ability to ionize the elements with a restricted range of energies and the 100% transmission (from the source to the collector), lower and more consistent average mass fractionation and the use of single element solutions to eliminate isobaric interferences. On the other hand, not all elements are easily ionized, some have low ionization potentials, in fact ionization is generally less than 1%; mass fractionation continually

changes during analysis and in addition the correction is possible just for the elements that have 3 or more isotopes of which at least 2 are stable and finally elementally pure solutions are required to avoid isobaric interferences, which requires extensive preparation.

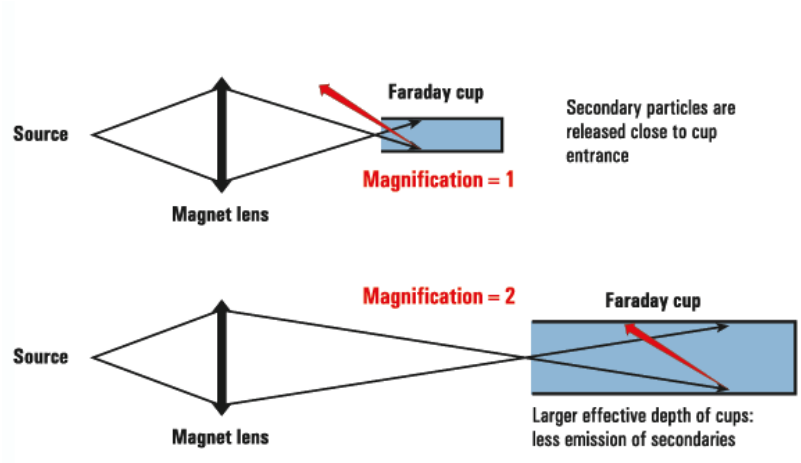

Figure 20: TIMS' main components, as the source, the magnet and the Faraday cup (collector).

CHAPTER 4 - RESULTS

This section reports the results obtained from the optical microscope analysis *i)* petrographic description, and the results obtained from the isotopic analyses *ii)* isotopic ratios and compositions. The major and trace element mineral compositions of gabbros from the Mado Megamullion are those published in Basch et al. (2022). Petrographic analyses and mineral geochemical compositions of Tosa and Sanuki Megamullion gabbros are unpublished data obtained during the postdoc project of Valentin Basch and reported here as a separate study for simplicity.

4.1 Petrography

Thin sections (n=30) approximately 50 microns-thick were obtained from the hand samples and analysed with a transmitted polarised light optical microscope. For each thin section, a petrographic description was produced, accompanied by a high-resolution scan of the thin section, both in parallel polarised light, crossed polarised light, and reflected light for some samples where it was deemed necessary. From this initial work, a distinction of four lithologies was obtained for the central Mado, i.e., olivine gabbro, gabbro, varitextured gabbro and felsic veins; for the sampling of the Mado transform walls, two main lithologies were recognised, namely mylonitic gabbros and mylonitic oxide gabbros. The samples recovered from the Nankaido OCCs group have been assigned to four main lithologies, i.e., diorite, oxide diorite, felsic vein and basaltic andesite. Table 3, at the end of the chapter, provides a summary of the lithologies identified for each sample.

4.1.1 Central Mado

For each lithology, it is reported the modal content in vol% of the rock-forming minerals, then described through observations done with the microscope.

4.1.1. a) Olivine-Gabbro

Thin sections YK19-04S-6K-1536R14A, YK19-04S-6K-1536R18, YK19-04S- 6K -1536R20I, YK19-04S-6K -1536R20II, YK19-04S-6K -1536R20III are identified as deformed olivine gabbros. While YK19-04S-6K-1536R14A and YK19-04S-6K1536-R18 show no deformation (Fig.21), YK19-04S-6K-1536-R20I, YK19-04S-6K -1536R20II and YK19-04S-6K -1536R20III show a mylonitic foliation (Fig 22). All samples have an intermediate to strong alteration characterised by the presence of green amphibole. In addition, the deformed sample is crosscut by a felsic vein. Accordingly, the olivine gabbro samples present a phaneritic-hypidiomorphic texture to mylonitic texture. The grain-size in the undeformed samples is medium, whereas the deformed sample has

larger porphyroclasts of clinopyroxene and olivine immersed in a fine-grained background matrix of mainly plagioclase. Olivine crystals are rarely preserved and tend to appear almost completely substituted. Plagioclase represents the dominant phase in both samples; plagioclase crystals are large and well preserved in the undeformed samples, while they are fine-grained and form neoblastic aggregates in the deformed sample. Clinopyroxene crystals are preserved in places, as in sample YK19-04S-6K1536-R18, while in other cases they are poorly preserved and replaced by amphibole, surrounded by amphibole coronas or very fine-grained aggregates of plagioclase and amphibole crystals.

In the mylonitic olivine gabbro sample, it is also possible to establish the deformation facies by examining the mineral assemblage composing the mylonitic bands. When these are characterised by amphibole neoblasts, the deformation will have taken place at the temperature, pressure and depth typical of amphibolite facies; when the mylonitic bands are characterised by recrystallization of clinopyroxene and amphibole neoblasts, it indicates that the deformation most likely took place in granulite-facies conditions. Mylonitic bands within sample YK19-04S-6K1536-R20II present small crystals of both clinopyroxene and amphibole (green-brown), suggesting granulite-facies deformation andrecrystallisation.

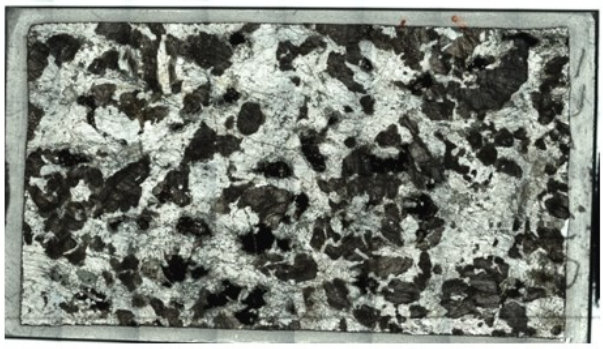

Figure 21: YK19-04S-6K1536-R18 olivine gabbro undeformed

Figure 22: YK19-04S-6K -1536R20II mylonitic olivine gabbro

- Olivine (5-10 vol%)

Although olivine is mainly substituted by alteration minerals, the characteristic mesh texture is still recognizable (Fig. 23a) and the habitus of the former olivine ranged from sub-euhedral to anhedral and millimetric in size. In very few cases, it is possible to glimpse the typical colourless/yellowish appearance, with parallel Nicols, and the typical high interference colours with crossed Nicols, of olivines (Fig.23b). Olivine rims are very characteristic as they have a denticulated shape and are

surrounded by a crown of alteration of serpentine. The inner portion of the olivine is mostly magnetite and serpentine.

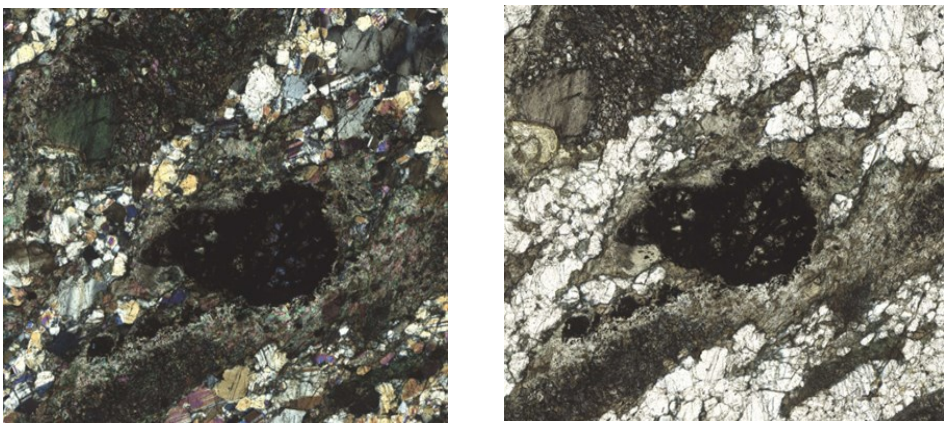

Figure 23: a) Olivine crystal in // Nicols; b) Olivine crystal in X Nicols.

In the mylonitic bands of the deformed sample, the relict olivine appears stretched, following the trend of the deformation and displaying sigma-shapes, although much less than the clinopyroxene/amphibole. Recrystallization shadows can be spotted along the edges (Fig.22)

- Plagioclase (50-60 vol%)

Plagioclase crystals are found in olivine gabbro samples as two main occurrences. In the undeformed sample it appears as crystals of medium size and mostly well preserved, with a sub-prismatic shape. At parallel Nicols the crystals are colourless/clear and show low relief. Even if well preserved, they are characterised by strong fracturing. Crossed Nicols still show the characteristic grey colour of the first order and albite polysynthetic twinning. Plagioclase crystals in the deformed samples accumulate along the mylonitic bands with a fine-grained recrystallization texture. Recrystallization represents the replacement of large magmatic plagioclase with aggregates of plagioclase neoblasts, following deformation. Aggregates of even smaller dimensions are arranged along the edges of relict clinopyroxene and olivine phenocrysts together with hornblende, forming the so-called recrystallization shadows (Fig.22) typical of mylonitic belts.

- Clinopyroxene (30-40 vol%)

The other predominant phase in these olivine gabbros is clinopyroxene. Clinopyroxenes are also often poorly preserved, as they are affected by a diffuse alteration and substitution by low-temperature amphibole. In the undeformed sample, despite the above-described alteration, the pyroxene crystals tend to have large dimensions, its relief is high and its natural colour ranges from grey to pale brown

with very weak pleochroism and evident fractures. The shape of the crystals is prismatic but shows strong cleavage planes. Crossed Nicols highlight the typical high interference colours of clinopyroxene. In the deformed samples the clinopyroxene is almost completely replaced, yet it is still possible to see reworked clinopyroxene porphyroblasts surrounded by an alteration crown of amphibole replacing clinopyroxene and by small, recrystallised aggregates of amphibole, plagioclase and secondary clinopyroxene. These neoblasts form shadows around the stretched clinopyroxene crystals. Notably, the porphyroclasts of relict clinopyroxene are surroundedby a fine-grained assemblage of crystals of secondary clinopyroxenes and amphibole, indicating deformation and recrystallization in granulite facies (Fig.24).

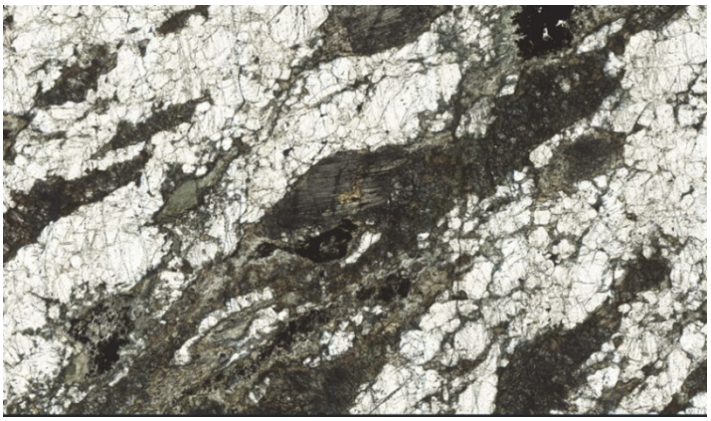

Figure 24: Cpx porphyroclast surrounded by new cpx and amph neoblasts.

- Felsic Vein

The thin section YK19-04S-6K1536-R20I is an olivine gabbro which underwent deformation. The thin section bears a contact between a felsic vein and the crosscut mylonitic olivine gabbro (Fig.25). The direction of intrusion is perpendicular to the direction of deformation (mylonitization) undergone by the sample. This crosscutting vein is associated with some displacement of the host rock and represents the crystallisation of an evolved melt that has intruded the host gabbro along a pre-existing fault. The contact between the host rock and the vein is sharp, and the latter is formed of millimetric crystals of plagioclase, green-brown amphibole, and oxides. The edges of the vein are characterized by an enrichment of dark-green amphibole possibly representing a reaction zone between the intrusion and the host rock.

Figure 25: YK19-04S-6K1536-R20I felsic vein-mylonitic olivine gabbro contact.

4.1.1 b) Gabbro

Two thin sections were identified as undeformed gabbro, KH18-2-D5-R101B3 and YK19-04S-6K1536-R16II, which presents mylonitic deformation in part of the sample, while the rest is undeformed. Both samples are mainly composed of three mineralogical phases, i.e., mostly plagioclase, relic clinopyroxene, and low-temperature green amphibole linked to the alteration and forming coronas around the relic clinopyroxene. In fact, both sections present a medium- to high-grade alteration, highlighted by the greenish colour characterizing the hand specimen after formation of alteration minerals such as green amphibole. This green colour is best visible in the sample KH18-2-D5R101B3. These gabbro samples present a phaneritic-hypidiomorphic to foliated texture. YK19-04S-6K1536-R16II shows a general medium grain-size, with plagioclase occurring as small crystals while relict clinopyroxene shows larger dimensions ranging from 0.5 to 2 mm. Within the deformed part of the sample, clinopyroxene shows similar crystal size to the undeformed part of the sample, whereas neoblastic plagioclase is characterized by very fine grain size in some recrystallization bands concentrating deformation (Fig.26a). Conversely, KH18-2-D5-R101B3 is a fine-grained gabbro, i.e.

crystals of all phases show fine grain-size. It also shows the occurrence of two narrow amphibolite veins and a series of fractures (Fig.26b).

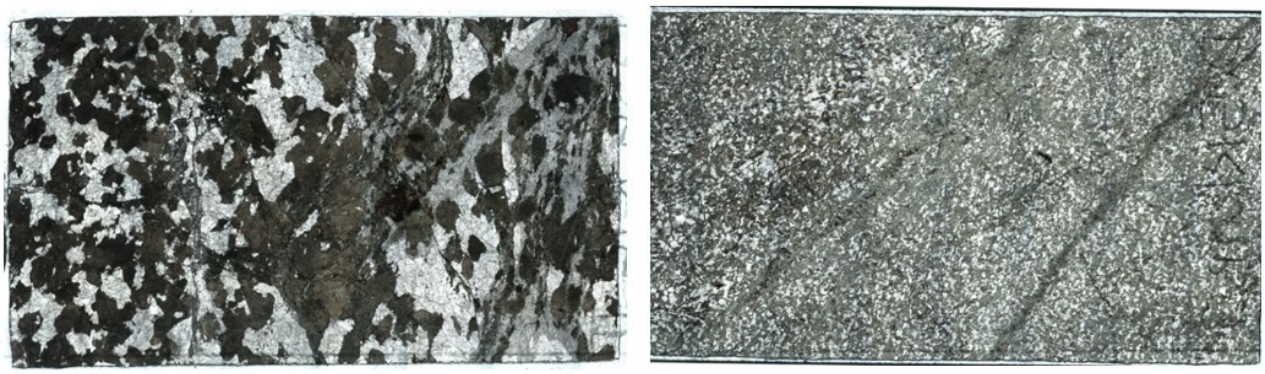

Figure 26: a) YK19-04S-6K1536-R16II medium to fine grain size, and partly deformed with recrystallization bands; b) KH18-2-D5-R101B3 fine grained gabbro with amphibolite veins and fractures.

- Plagioclase (50-60 vol%)

Plagioclase is the most common phase in gabbro samples. It occurs as large crystals formed by the parental melt, or recrystallized in smaller dimensions, forming a groundmass in the deformed sample in which the large relict clinopyroxene crystals are immersed. In the fine-grained sample, plagioclase and clinopyroxene both present small grain sizes. Regardless of size, plagioclases are generally euhedral with rectangular or square shapes, and is colourless, clear and with low relief in plain-polarized light. Plagioclase is strongly fractured and the identification of the cleavage planes along [001] and [010] is not straightforward. At crossed Nicols the plagioclase crystals present grey colours of the first order and in some cases albite polysynthetic twinning.

- Clinopyroxene (40-50 vol%)

Clinopyroxenes represent the other fundamental component of the gabbro samples. In the deformed sample, clinopyroxene have dimensions ranging from 0.5 to 2 mm and therefore tend to be large despite often appearing as poorly preserved relics. These are immersed in a groundmass of small-sized plagioclase. In the case of the undeformed but homogeneously fine-grained sample, however, the clinopyroxene crystals show similar grain size to the plagioclase. These clinopyroxene crystals are mostly replaced by hydrated minerals of a greenish colour with parallel Nicols, i.e. the green amphibole typical of low-medium temperatures. At parallel Nicols therefore the clinopyroxene has a dark grey-brown colour, high relief and very low pleochroism. The edges of clinopyroxene crystals are sometimes irregular, while the shape of the crystal remains quite elongated prismatic in most cases. They also tend to form an intergranular/interstitial texture in the undeformed part of the

deformed sample; in the foliate band they instead tend to arrange themselves along the trend of the deformation. Also in this deformed zone, the clinopyroxene crystals present a large amphibolite crown which in some cases has almost completely replaced the primary clinopyroxene in secondary alteration amphibole; Furthermore, in the recrystallization bands we find clinopyroxenes of very small dimensions, therefore not primary relics but rather of a crystallisation that occurred subsequently. At crossed Nicols the clinopyroxene crystals show high interference colours and oblique extinction with respect to elongation. These features are common in the two different samples but obviously less easy to see on the fine-grained sample.

4.1.1 c) Varitextured Gabbros

KH18-2-D05R101AI, KH18-2-D05R101AII, KH18-2-D05R101AIII, KH18-2-D05R101AIV were identified as varitextured gabbros, all undeformed. The phases present with the greatest volume percentage in the whole rock are plagioclase, with crystals of very variable dimensions and relic clinopyroxene of large dimensions, partly altered, dark patches of brownish amphibole can be seen which it is replacing clinopyroxene due to alteration. These samples were called varitexture precisely because they present different textures and sizes of crystals in the same sample. Specifically, we find these areas in which crystals have crystallised, in a radial pattern, in small dimensions, but above all they form 120° angles between the grain boundaries of three crystals (less present in KH18-2-D05R101AII). This texture is in fact called triple junction grain and is typical of magmatic processes, already at first glance it is possible to recognize its magmatic origin (Fig.27). This type of texture is associated with in situ crystallisation of melt drops during the crystallisation of the Olivine (near solidus) at relatively low Temperature and Pressure, in an environment with little magmatic input. May subsequently the body, exhumed by the detachment fault, pass to shallower environment conditions. Therefore, the melt did not have much time and space to develop large plagioclase and clinopyroxene crystals. In general, varitextured gabbro exhibit relatively low to high alteration. The greatest evidence is found in green amphibole/chlorite coronas that form at relatively low temperature and pressure. We also find amphibole as a filling inside fractures. Scattered throughout all the samples we find bands of recrystallization/alteration made up of very small, needle-like crystals of different aggregates: plagioclase, pyroxenes and amphiboles (Fig.28).

Figure 27: KH18-2-D05R101AI varitextured gabbro with triple junction grain.

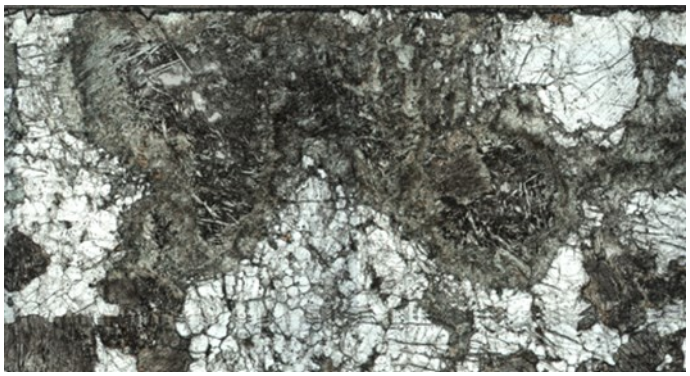

Figure 28: Recrystallization bands with needle-like crystals (KH18-2-D05R101AIII)

- Plagioclase (55-70 vol%)

Plagioclase represents the main phase. In these samples the plagioclase crystallises in different sizes, in some cases exceeding 2.5 mm while in other cases it has dimensions of 0.5 mm or less. It tends to have these small dimensions in the triple junction grain zones where the residual melt crystallises in situ without having time (i.e. temperature) and space to develop the crystals. At parallel Nicols the crystals are colourless, clear and with low relief, but characterised by strong fracturing. The euhedral habit of the plagioclase crystals has an elongated rectangular shape if well preserved, while the crystals developed in the triple junction grain areas have a square shape. At crossed Nicols we observe first order birefringence colours, grey and Carlsbad twinning typical of plagioclases, for those crystals that have managed to remain well preserved. However, it is also possible to observe interference colours that are always first order but yellow or fuchsia, with less clear and preserved twinning for those crystals that have undergone a certain alteration.

- Clinopyroxene (30- 45 vol%)

The other major phase in these samples is clinopyroxene. The crystals are in most cases affected by alteration, which ranges from relatively low to high degree. Despite the alteration and thanks to their

large size (>2.5mm in some cases) these crystals are clearly visible. As well as the plagioclase crystals, in the triple junction grain zones we also find clinopyroxene crystals. This type of texture represents the last phases of crystallisation of a melt in situ, probably the melt trapped in separate drops begins to crystallise in conditions of low temperature, pressure and depth and therefore develops small crystals. Parallel Nicols have a rather dark grey-brown colour, elongated shape and irregular grain boundaries. It is also possible to notice high relief, weak pleochroism and traces of cleavage. With crossed Nicols the crystals appear with high interference colours sometimes masked by the very dark colour of the crystal itself, the extinction is oblique with respect to the elongation of the crystal. The characteristics just described are the same both in the triple junction grain areas and in the other parts of the sample. Clinopyroxene crystals often present alteration structures such as amphibolite crowns or narrow recrystallization bands composed of very small needle-shaped crystals of various aggregates including green amphiboles, or spots of reddish magnetite-type oxides on the mineral itself.

4.1.1 d) Felsic Veins (contact)

KH18-2-D05R101B1, KH18-2-D05R101B2 and KH18-2-D05R101B4 are classified as the contact between the host fine-grained gabbro and an intruded felsic vein. The gabbro constitutes the encasing or host rock older and undeformed, while the felsic vein represents the intrusion of a melt rich in light elements (such as silica, aluminium, oxygen, etc.), which made its way into the encasing rock through fractures or along areas of weakness. Along the contact there is a millimetre-thick reaction zone (Fig.29), characterised by green amphiboles, relict/altered clinopyroxene and oxides, with a poikilitic texture. Amphibole and clinopyroxene are phenocrysts while plagioclase is enclosed within. This suggest that plagioclase crystalize before clinopyroxene and amphibole. The host gabbro is fine-grained and composed mainly of plagioclase and clinopyroxene mostly altered to green and brown amphibole. The felsic vein is composed mainly of large plagioclase and scattered relics of clinopyroxene with reaction crowns around the edges of the crystals. Furthermore, it is often possible to identify a granulitic or poikilitic texture typical of intrusion magmatism.

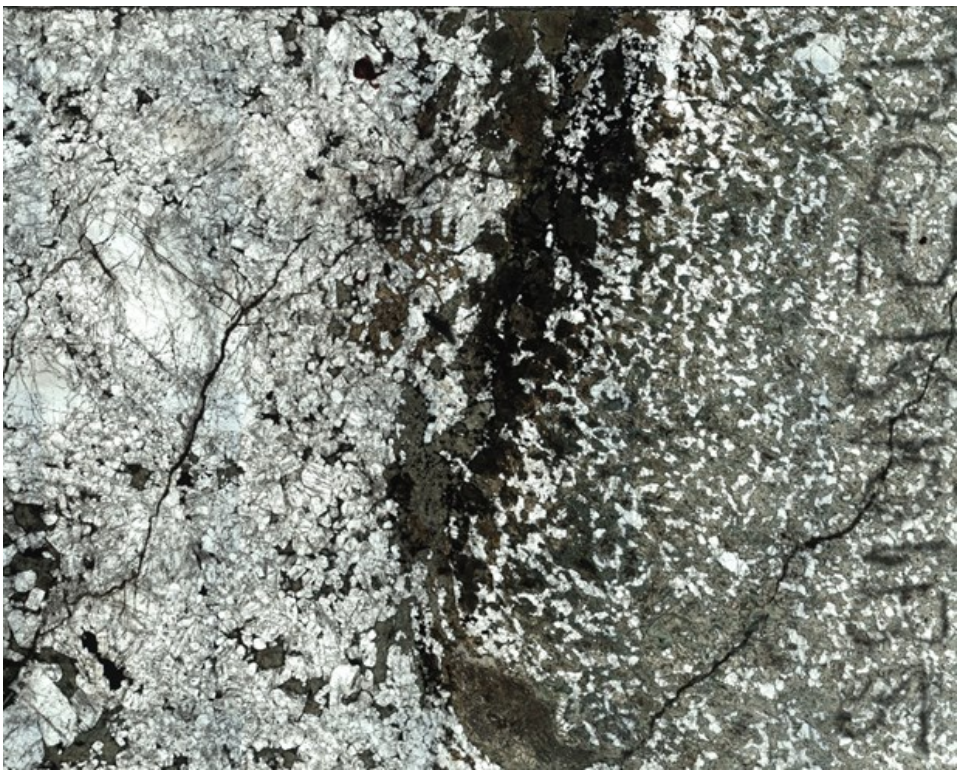

Figure29: Reaction zone along the contact gabbro-felsic vein (KH18-2-D05R101B2).

- Plagioclase (60-65 vol%)

Compositionally, plagioclase is the phase that dominates both lithologies, i.e. the fine-grained gabbro and the felsic vein, but it occurs in different sizes and shapes. In gabbro it occurs with dimensions of less than 0.5 mm, while in the felsic vein the plagioclase crystals in some cases exceed 2.5 mm in size. Analysing the sample in parallel Nicols, in both areas of the sample, the appearance of the plagioclase crystals are colourless, clear and with low relief. The shape of the crystals tends to be sub-prismatic in the gabbro, euhedral, rectangular or square in the felsic vein. The traces of cleavage are barely visible (due to the size?) in the fine-grained gabbro but are clearly visible in the felsic vein. At cross Nicols, the plagioclase crystals show the typical interference colours of this mineral, i.e. grey but also yellowish orange, of the first order and twinning. Furthermore, plagioclase occurs, in the felsic vein and in the reaction zone, as chadacrysts, small, elongated crystals enclosed in larger crystals called oikocrysts, forming a poikilitic texture.

- Clinopyroxene (30-40 vol%)

Clinopyroxene represents the other predominant phase within these samples. The dimensions of the crystals vary, in the gabbro there are relics and small ones often almost completely replaced by green amphibole due to the alteration, while in the felsic vein the crystals, relics here too, can exceed 5 mm

in size. With parallel Nicols, pyroxene crystals are dark grey, brown in colour with an elongated shape and irregular edges. The pleochroism is typically weak while the relief is very high. With crossed Nicols clinopyroxene crystals exhibit oblique extinction with respect to elongation and second-order interference colours. However, the very dark colour of the crystals influences the interference colours, which despite being high, are not very bright/intense. In KH18-2-D05R101B1 there is a reaction structure (Fig.30), i.e. a core of relict clinopyroxene, surrounded by a large crystal of brown amphibole, the latter characterised by some oxide and plagioclase in poikilitic texture. The reaction rim between relict clinopyroxene and amphibole is made up of very small aggregates of clinopyroxene and amphibole.

Figure 30: Reaction structure, cpx relic core surrounded by brown amph with poikilitc texture (KH18-2-D05R101B1).

4.1.2 Mado along the Transform fault

Samples recovered along the transform fault near Mado, are all more or less deformed, as it is expected in a shear zone. The original lithologies were gabbro and oxide gabbro, however, being deformed samples, the lithologies identified after microscope analysis are: protomylonitic and mylonitic oxide gabbro; and mylonitic and ultramylonite gabbro.

4.1.2 a) Mylonitic Oxide Gabbros

Oxide gabbros have been classified into protomylonites and mylonites, based on texture that depend on the degree of deformation undergone. The protomylonitic ones are: YK18-07S-6K-1515R14, YK20-18S-6K- 1569R06A, YK20-18S-6K-1569R08B, KH18-2-D12R101 and KH18-2-D12R107.

The mylonitic oxide gabbros are: YK18-07S-6K-1515R04, YK20-18S-6K-1569R06B, YK20-18S-6K-1569R07B, YK20-18S-6K-1569R08A and YK20-18S-6K-1569R09.

- Protomylonite:

The protomylonites do not yet have a well-developed foliation as they are linked to the first stages of deformation. In fact, these samples contain more than 50% porphyroclasts, meaning most of the rock has not been recrystallized. Thus, these samples are characterised by less to more reworked large clinopyroxene porphyroclasts. In some it is also possible to see the shadows of the beginning of deformation around the porphyroclast (Fig.31). The background matrix is instead represented by plagioclase, not that much altered, and secondary clinopyroxene. Mylonitic bands are characterised by small crystals of brown amphibole suggesting that deformation occurred in the amphibolitic facies (medium T and P). As mentioned in paragraph 5.1.1a, by identifying the crystallised mineral in the mylonitic bands it is possible to establish the metamorphic facies at which the deformation occurred. The mylonitic bands are also enriched in oxides, this could represent the injection of an evolved melt therefore enriched in oxides, which by crystallising can produce these enrichments. The alteration ranges from medium to high, in fact the phenocrysts are often almost completely replaced and there is a strong presence of green and brown amphibole.

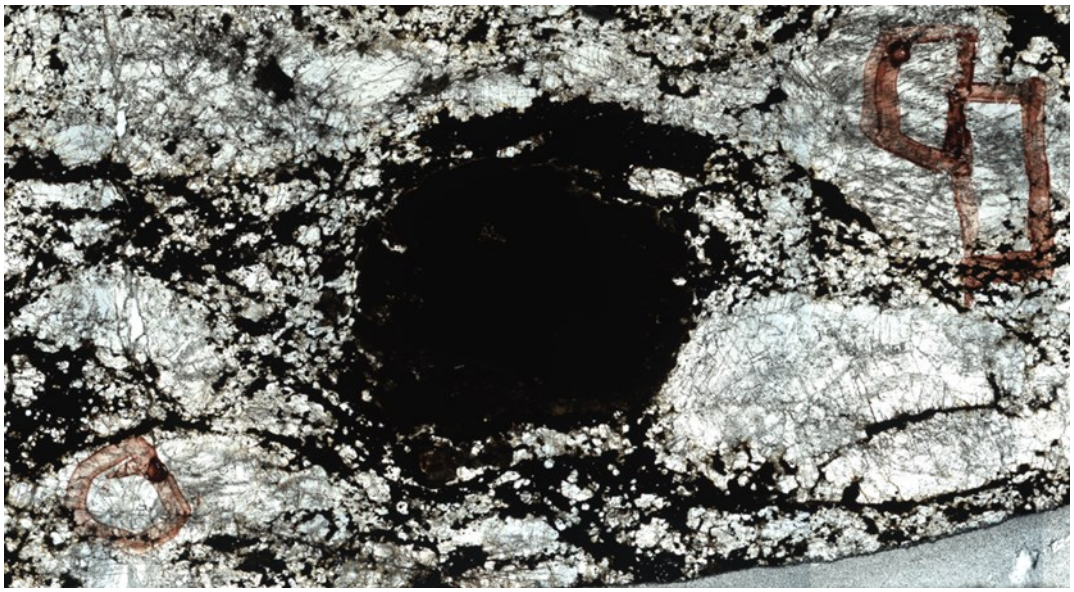

Figure 31: Porphyroclast with deformation shadows (KH18-2-D12R107).

- Mylonites:

These samples are strongly foliated and characterised by grain reduction. Large porphyroclasts, some exceeding 10 mm of clinopyroxene are observed, surrounded by mylonitic bands with amphibole

neoblasts, sometimes secondary clinopyroxene are also observable, as well as plagioclase porphyroclasts surrounded by plagioclase neoblasts (Fig.32), so the deformation facies were both granulitic and amphibolitic ones. In this case the mylonitic bands are much more widespread than those present in protomylonites. The porphyroclasts are arranged in a preferential direction representing the direction of deformation. Also, in these samples there are enrichments of oxides within the mylonitic bands or around the phenocrysts. The alteration ranges from medium to high, in fact the phenocrysts are often almost completely replaced and there is a strong presence of green and brown amphibole.

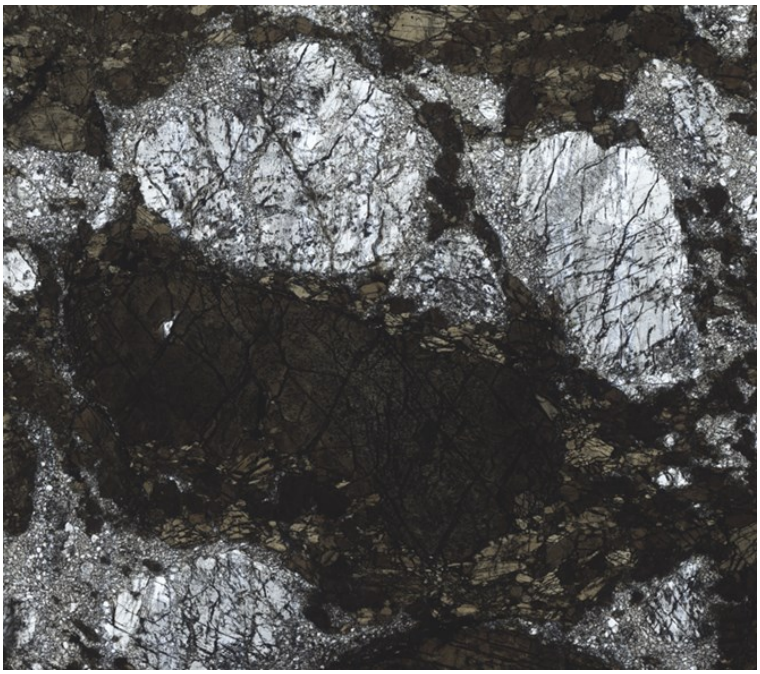

Figure 32: Cpx porphyroclast surrounded by secondary cpx and amph; Plg porphyroclast surrounded by plg neoblasts (YK20-18S-6K-1569R07B).

- Plagioclase (45-65 vol%)

Protomylonitic samples contain approximately 50-70 vol% of plagioclase while mylonitic samples contain approximately 45-65 vol% of plagioclase. Plagioclase crystals appear in different shapes and sizes based on the areas within the sample, so based on the level of deformation they have undergone. Porphyroclasts are large with rather rounded edges and shapes. These are surrounded by small secondary plagioclase. At parallel Nicols the colour of large plagioclase crystals goes from clear to wavy (Fig.33) (as the crystals are more affected by deformation), while small crystals are typically colourless and very clear. In both cases the crystals have low relief. At crossed Nicols the plagioclase presents first order interference colours from grey to yellowish, rarely Carlsbad gemination. Regarding alteration, some samples (e.g. KH18-2-D12R107) present the plagioclase crystals as relicts.

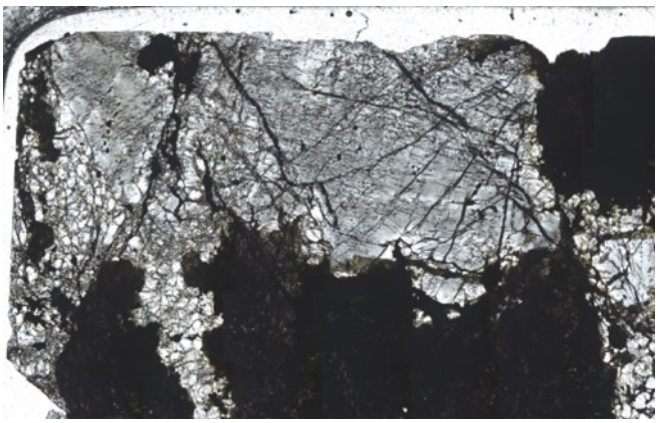

Figure 33: Plagioclase from clear to wavy, as deformation suffered increases (YK20-18S-6K-1569R06B).

- Clinopyroxene (20-40 vol%)

The clinopyroxene crystals appear mostly relict and deformed, sometimes replaced by green amphibole. They appear as phenocrysts in a background matrix; these are often surrounded by small secondary brown amphiboles as neoblasts born from deformation (amphibolite facies). At parallel Nicols the clinopyroxene has a very dark grey-brown colour, high relief and low pleochroism. They present strong fracturing, as well as the typical traces of cleavage, and edges that are increasingly less defined as the crystal presents greater alteration/deformation. At crossed Nicols the interference colours are not as high as normally expected from clinopyroxene. The interference colours of clinopyroxene are in this case of the first order brownish and influenced by the dark coloration visible at parallel Nicols. Where the clinopyroxene phenocrysts are almost completely replaced we notice very small, almost needle-like aggregates of green-brown colour with parallel Nicols, and with very high interference colours with crossed Nicols (Fig.34). These are second order amphiboles.

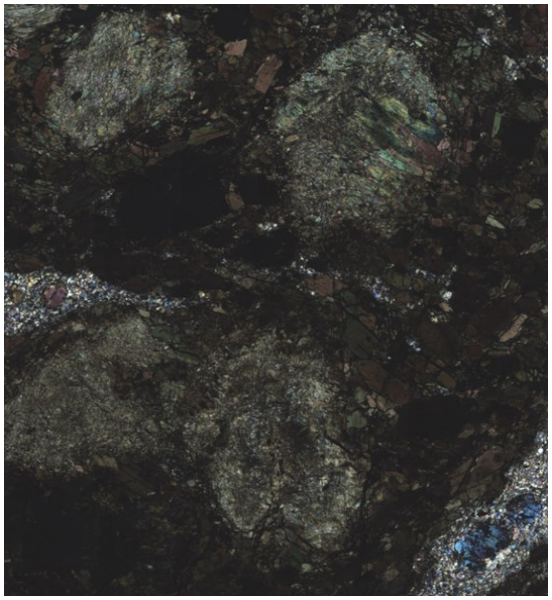

Figure 34: Needle-like second order amphiboles crystals around almost replaced cpx (YK20-18S-6K-1569R07B).

- Oxides (10-35 vol%)

The oxides represent the third fundamental phase of this gabbro lithology with mylonized oxides. Their distribution is characteristic, in fact they are found with greater concentration in the mylonitic bands (Fig.35), at the edges of the porphyroclasts and within those porphyroclasts that are almost completely altered/replaced. In protomylonitic samples their estimated presence in vol% is slightly lower than in mylonitic samples. For the protomylonitic ones, a content of 10 to 20 vol% was estimated, while for the mylonitic ones the estimate ranges from 10 to 35 vol%. Both at parallel nicols and at crossed nicols the oxides are always dark and always extinguished. For greater confirmation, these samples were also analysed with reflected light, in this case the oxides appear completely white, due to the high weight of the elements that compose them (Fig.36). The strong presence of oxides in the mylonitic bands is called enrichment and may represent the intrusion of a highly evolved melt, therefore rich in oxides, which made its way thanks to the greater ease of inserting itself into areas characterised by strong and therefore weaker deformations. The analysis of this enrichment can provide useful information on the temperature, pressure and depth conditions at which the intrusion would have occurred. It can also be associated with a specific deformation facies.

Figure 35: Mylonitic bands with oxide enrichments (YK20-18S-6K-1569R08A).

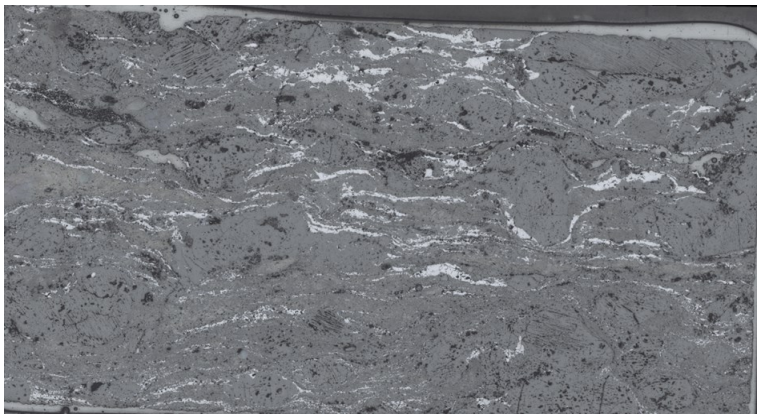

Figure 36: YK20-18S-6K-1569R08A in reflected light, white portion are oxides.

4.1.2. b) Mylonitic Gabbros

The thin sections YK20-18S-6K-1569R04A and YK20-18S-6K-1569R04B are classified as mylonitic gabbro, while YK20-18S-6K-1569R10 as ultramylonite gabbro. The difference lies in the degree of deformation, in the case of mylonitization we have well-defined mylonitic bands interspersed with large stretched porphyroclasts and surrounded by neolastes to form recrystallization trails around the phenocrysts; while in the case of ultramylonites the deformation has reached such a high level that all the crystals of the rock have been completely recrystallized in small dimensions, no phenocryst remains. The samples classified as mylonitic gabbro differ from those described in paragraph 6.1.2. a as they do not present oxides, or rather there are, but confined to a specific part of the sample. This represents the relationship between the two different lithologies: gabbro and oxide gabbro. This relationship will be described later. The main phases present within the samples are plagioclase, clinopyroxene and amphibole.

- Plagioclase (60-65 vol%)

The plagioclase appears everywhere as recrystallized in small dimensions, forming the mylonitic bands (together with other aggregates the background matrix, underlying the relics of phenocrysts). In some areas of the sample, i.e. those characterised by the presence of oxides, the plagioclase crystals are larger in size (Fig.37). Parallel Nicols observations predict colourless and clear crystals, in some cases they may present a wavy greyish colour. Furthermore, the plagioclase has low relief and euhedral shapes. At crossed Nicols the interference colours of the plagioclase crystals range from grey to yellow-brown of the first order. Furthermore, despite the very small size, Carlsbad twinning can also be observed.

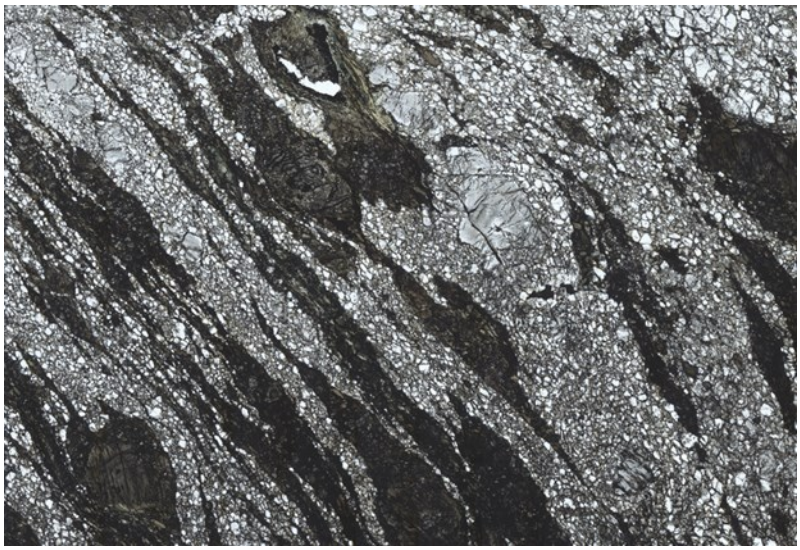

Figure 37: Large plagioclase in a zone with oxides (YK20-18S-6K-1569R04B).

- Clinopyroxene (30-40 vol%)

Clinopyroxene is present within these samples both as a recrystallization phase within the mylonitic bands and as relict phenocrysts weakened by deformation. In the mylonitic belts the clinopyroxene is secondary and is associated with aggregates of brown amphibole, both small but perfectly unaltered. These crystals, if observed parallel to the Nicols, appear colourless to light grey-brown and high relief, with well-defined edges and euhedral shape. Crossed Nicols, on the other hand, have high and bright interference colours. The clinopyroxenes that make up the porphyroclasts are broken and extremely deformed. In fact, they have a sigmoidal shape and are surrounded by small secondary crystals to form the shadow or wings of the porphyroclast. These parallel Nicols crystals appear dark in colour and with very marked cleavages. At crossed Nicols you can glimpse the high interference colours typical of this mineral (Fig.38), in other cases they appear almost completely oxidised and therefore black and always extinct.

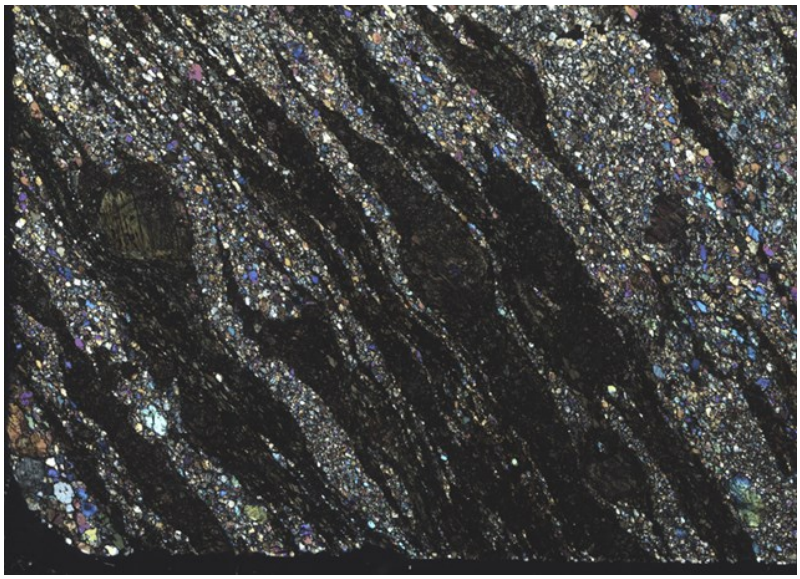

Figure 38: YK20-18S-6K-1569R04B wit X Nicols showing cpx high interference colours.

4.1.2. bb) Relationship between Oxides Gabbro and Gabbro mylonitic

The sample of mylonitic gabbro (YK20-18S-6K-1569R04B) seen in paragraph 6.1.2.b represents the evolution of the deformation undergone by the gabbro, in exhumation, which from the granulitic facies of greater depth (greater T and P) passes to the amphibolite facies which occurs more on the surface (lower T and P). Furthermore, by analysing this sample it was possible to associate the enrichments of oxides exclusively within the mylonitic bands of amphibolite facies, i.e. those composed of small light brown amphibole crystals. This association could indicate that the intrusion of an evolved oxide-rich melt occurred at shallower depths during the exhumation of the gabbro. In

the mylonitic bands of granulitic facies we find small crystals of secondary clinopyroxene and light brown amphibole, however we do not observe enrichment in oxides. Furthermore, the grain size appears to increase in the amphibolite facies.

4.1.3 Tosa and Sanuki (Nankaido OCCs)

In the following section, the petrographic features of the main lithologies sampled at Tosa and Sanuki, that form part of the Nankaido OCsC group, are described. For each lithology, the modal content in vol% of the minerals contained therein is expressed and they are described through observation under the optical microscope.

4.1.3. a) Oxide Diorites

Samples YK22-16S-6K-1655R02, YK22-16S-6K-1655R05 from Tosa and sample YK23-05S-6K-1675R10A from Sanuki were analysed under the microscope and were classified as oxide diorites. These samples are mainly composed of plagioclase, non-oriented euhedral, large, magmatic primary amphibole, and primary oxides. The oxide content is characteristic as in some cases it is very high. Among the different samples this oxide content varies, ranging from a very high concentration to lower concentrations. The texture of this lithological family also varies from interstitial, characterised by primary amphibole which crystallises in the empty spaces present between the plagioclases, to poikilitic, where large amphibole crystals are observed which within them include plagioclase crystals formed earlier. In this lithology the grain size of the minerals is also variable, ranging from millimetric (~5 mm) to centimetre (~1 cm). Another fundamental characteristic of these samples is the total absence of clinopyroxene. As regards the alteration, a low to intermediate level has been defined as in most cases all the minerals are well preserved, only in a few cases has green amphibole alteration been observed at the rim of the primary amphiboles. However, this presence of green amphibole at the rim of the dark brown amphibole represents a re-equilibration phase of the mineral that occurred during the exhumation of the OCC, due to the sample temperature and pressure conditions. Therefore, in addition to having low alteration, these samples did not undergo any deformation.

- Plagioclase (45-70 vol%)

One of the three main phases is plagioclase. In these samples the plagioclase crystals are well developed, perfectly euhedral, i.e. rectangular, and large (>8mm), where the samples have an interstitial texture. Inside the samples with poikilitic texture the plagioclase crystals are well preserved but are smaller in size as they are surrounded by the primary amphibole. Therefore, being

included within another primary mineral, they have a rounded shape. In both cases at parallel nicols the crystals appear colourless and clear with low relief. Traces of cleavage, good on [001] and distinct on [010], and fractures can also be observed. Cross-Nicols plagioclase crystals exhibit first-order interference colours from grey to dark yellow. Geminations associated with Carlsbad are very frequent.

- Primary amphibole (20-50 vol%)

The second important phase due to the high content within these samples is primary amphibole. This is mostly large, sometimes it can reach centimetre dimensions. Since the alteration is low to medium, it is very well preserved, in some cases there are crystals whose edges are surrounded by green amphibole of lower temperature and pressure probably due to the re-equilibrium of the primary amphibole minerals. This rebalancing may be associated with the exhumation of the OCC body. The amphibole crystals develop, forming a texture that goes from interstitial to poikilitic, or in the first case they develop by crystallising in the empty spaces more and more until they include the previously crystallised plagioclase crystals within them. In fact, through observation under the microscope, the 120° angles that form between the grain boundaries are extremely evident (Fig.39). Each crystal has well-defined sharp/sharp corners, typical of this magmatic texture. At parallel Nicols the amphibole crystals have a light to dark brown colour, low relief, high pleochroism and fracturing. In some crystals, traces of cleavage are also clearly observable. At crossed Nicols the interference colours range from yellow-brown of the first order to green-blue-pink of the third order, therefore from medium-low to high interference colours.

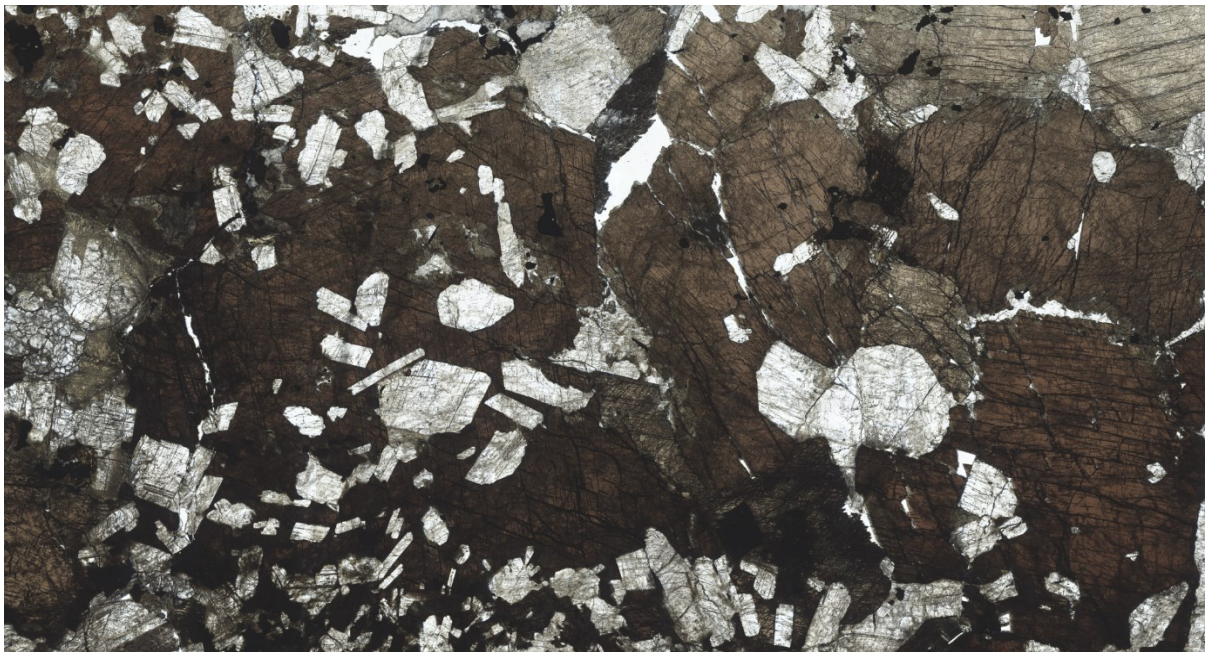

Figure 39: Poikilitic texture formed by large primary amphiboles crystals in YK22-16S-6K-1655R05B.

- Oxides (5-20 vol%)

The third fundamental phase of this lithological family are the oxides. These are magmatic oxides and not alteration. In fact, these present a sharp-edged shape typical of the in-situ crystallisation of parts of melt highly enriched in oxides. Their concentration is not high everywhere however they represent a fundamental element for the classification of these samples. In some cases, they are found at the edges of plagioclase and amphibole grains, in other cases they are also found overlapping these crystals. Oxides also sometimes form a poikilitic texture by including other aggregates within them. As well as the distribution, the size of the oxide crystals also varies, some can reach dimensions of 2.5 mm. At parallel Nicols they appear very dark in colour and have no relief or pleochroism. At crossed Nicols the crystals are always extinct. In order to have a better visualisation of the oxides, analyses with reflected light were also carried out on these samples in order to obtain a map of the minerals present in the thin sections. The oxides typically containing heavy elements appear almost milky white on the map (Fig.40a). YK22-16S-6K-1655R02A shows a very characteristic titanite oxide (Fig.40b)

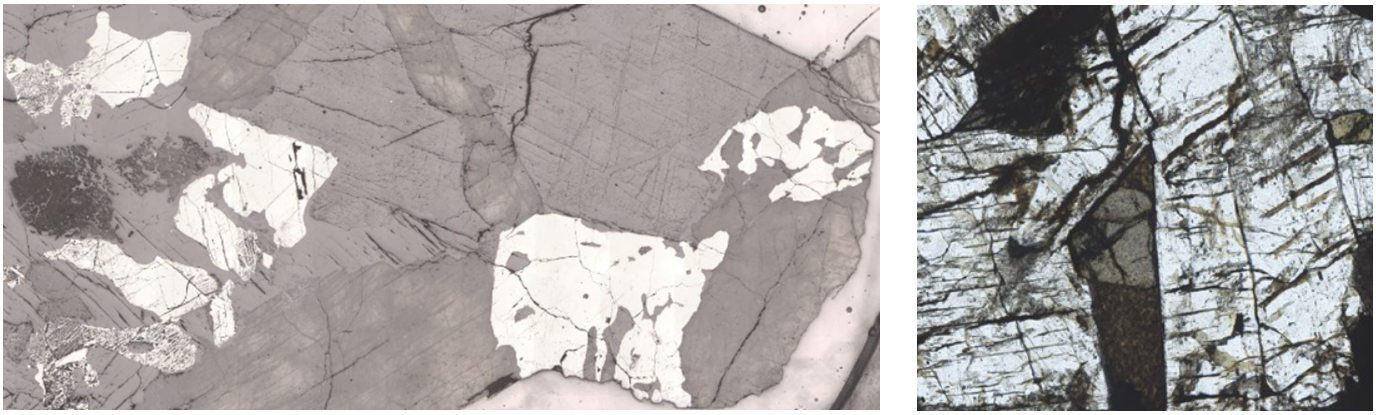

Figure 40: a) YK22-16S-6K-1655R05 in reflected light to highlight oxides phases; b) Titanite in YK22-16S-6K-1655R02A.

4.1.3. b) Felsic Vein - Oxides Diorite contact

Thin section YK23-05S-6K-1675R02A, from Sanuki it was possible to observe the contact between the oxide diorite and a felsic vein (Fig.41). Although the main lithology is the same as that seen in paragraph 6.1.3.a, some things about this oxide diorite differ slightly. For example, we observe a slightly lower content of primary amphibole which is smaller in size and slightly more altered, even the plagioclase crystals are sometimes less preserved and finally the presence of oxides is lower.
The felsic vein present on the right side of the sample is clearly visible at first glance. This has a fibrous, fine-grained texture, meaning that inside it the crystals have crystallised with a fibrous or

elongated shape. The felsic vein probably occupied a fracture and therefore an empty space within the oxide diorite. Within this vein we observe different aggregates such as feldspars, amphiboles and oxides. At parallel Nicols the clear colourless crystals of plagioclase are particularly visible, and brown-green amphibole crystals; while at crossed Nicols interference colours ranging from first order grey to high interference colours are observed, gemination and rarely even zonation are also observed.

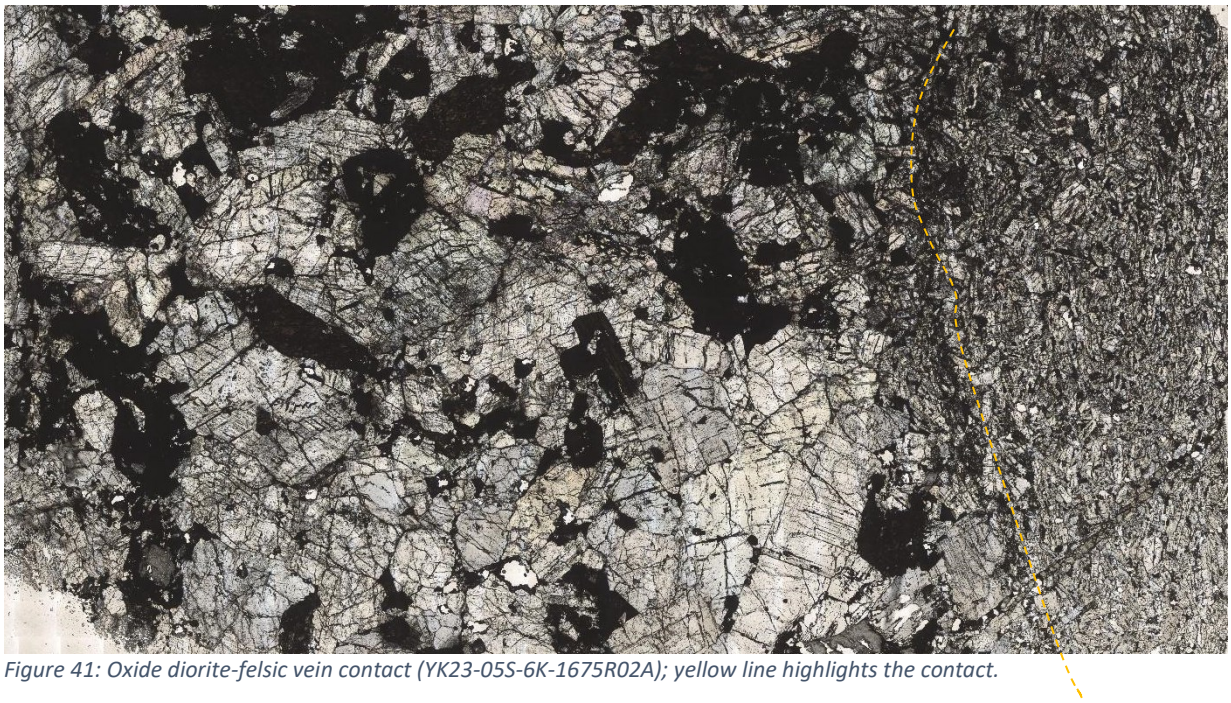

Figure 41: Oxide diorite-felsic vein contact (YK23-05S-6K-1675R02A); yellow line highlights the contact.

4.1.3 c) Basaltic Andesite - Oxides Diorite contact

Thin section YK23-05S-6K-1675R02C show the contact between the oxide diorite and a basaltic andesite (Fig.42). Although the main lithology is the same as that seen in paragraph 6.1.3.a, some things about this oxide diorite differ slightly. For example, we observe a slightly lower content of primary amphibole which is smaller in size and slightly more altered, even the plagioclase crystals are sometimes less preserved and finally the presence of oxides is lower.

In this sample the contact with basalt or rather basaltic andesite is visible on the right side. Between the two lithologies, i.e. oxide diorite and basaltic andesite, it is possible to observe a reaction zone in which the crystals take on recrystallization characteristics, in fact they are the same minerals that make up the oxide diorite but of much smaller and rounded dimensions (Fig.42).

Regarding basaltic andesite, do we observe an aphanitic texture, i.e. large crystals of primary plagioclase euhedral in shape immersed in a very fine-grained and fibrous or acicular background. The groundmass is complicated to analyse due to its size, however with parallel Nicols the presence of colourless plagioclase rods, green-brown amphibole aggregates and greyish pyroxenes can be recognized. Overall, the matrix with parallel Nicols appears very dark in colour while with crossed

Nicols we also observe a strong dark colour, but interference colours are also clearly visible ranging from the grey of the first order of the plagioclase rods, which almost always present twinning Carlsbad, very high interference colours for amphiboles. This intrusion of sialic melt (high content of light elements which allows the crystallisation of sialic minerals such as feldspars) has crystallised forming the andesitic basalt belonging to the calc-alkaline series.

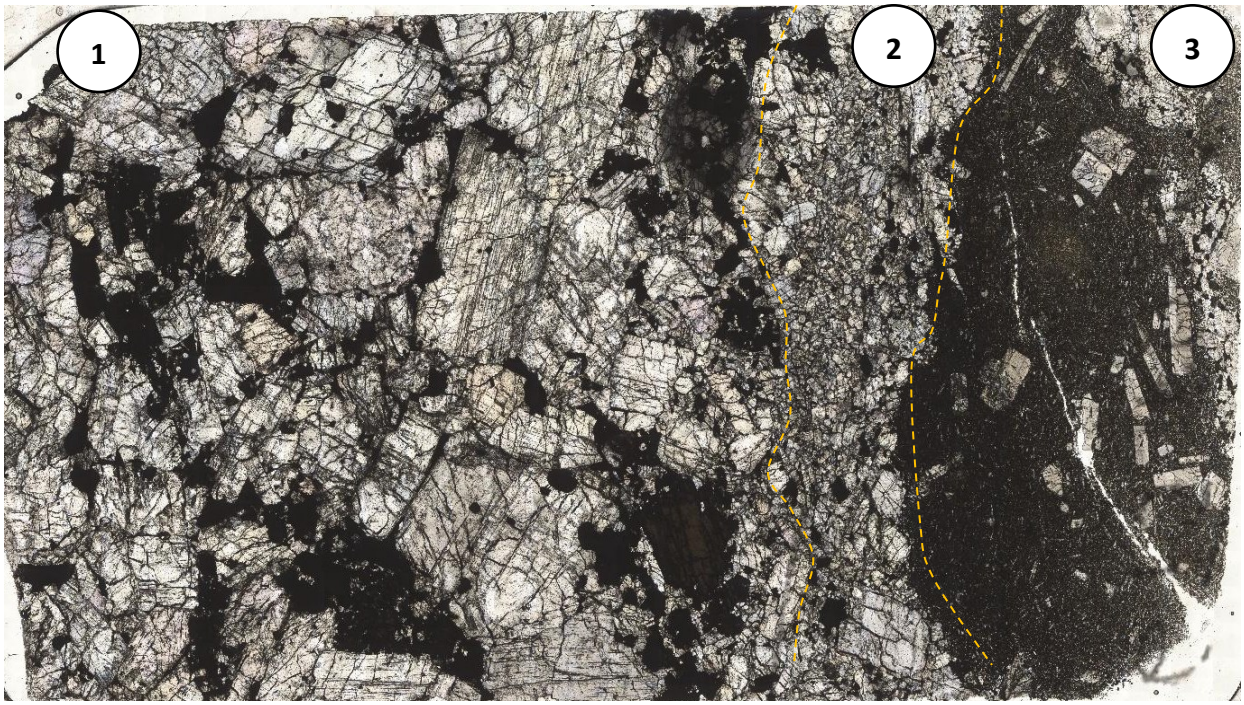

Figure 42: Oxide diorite(1)- andesitic basalt (3) contact (YK23-05S-6K-1675R02C); (2) reaction zone, fine grained oxide diorite.

Table 3: *Lithologies, deformation, minerals (%) composition and alteration grade.*

Sample name	Sampled Area	Lithology	Crystal-plastic Deformation	Ol %	Plg %	Cpx %	Primary Amph %	Oxide %	Alt
AYK19-04S-6K-1536R10	**Mado Central**	Gabbro varitext	no		60	40			---
YK19-04S-6K-1536R14A	Mado	Ol gabbro	no		60	40			---
YK19-04S-6K-1536R14BI	Mado	Gabbro varitext	no		60	35		5	--
YK19-04S-6K-1536R14BII	Mado	Gabbro varitext	no		55	45			---
YK19-04S-6K-1536R16II	Mado	Gabbro	half yes		50	50	1		---
YK19-04S-6K-1536R18	Mado	Ol gabbro	no	10	50	40			--
YK19-04S-6K-1536R20I	Mado	Ol gabbro	yes	7	52	40			--
YK19-04S-6K-1536R20II	Mado	Ol gabbro	yes	5	60	30		5	--
YK19-04S-6K-1536R20III	Mado	Ol gabbro	yes	5	60	30		5	--
KH18-2-D05R101AI	**Mado Central**	Gabbro varitext	no		60	40			-
KH18-2-D05R101AII	Mado	Gabbro varitext	no		70	30		1	--
KH18-2-D05R101AIII	Mado	Gabbro varitext	no		60	40			--
KH18-2-D05R101A IV	Mado	Gabbro varitext	no		55	45			--

KH18-2-D05R101B1	Mado	Gabbro-Felsic vein contact	no		65	30		5	--
KH18-2-KH18-2-D05R101B2	Mado	Gabbro-Felsic vein contact	no		65	30	5	5	--
KH18-2-D5R101B3	Mado	Fine grained Gabbro	no		50	50			--
KH18-2-D05R101B4	Mado	Gabbro-Felsic vein contact	no		60	40			--
YK18-07S-6K-1515R04	**Mado near Transform Fault**	Mylonitic Oxide Gabbro	yes		65	30		5	--
YK18-07S-6K-1515R14	Mado	Protomylonitic Oxide Gabbro	no		60	40		3	---
YK20-18S-6K-1569R04A	**Mado near Transform Fault**	Mylonitic Gabbro	yes		65	30	?	5	--
YK20-18S-6K-1569R04B	Mado	Mylonitic Gabbro	yes		60	40		5	--
YK20-18S-6K-1569R06A	Mado	Protomylonitic Oxide Gabbro	yes		50	40		10	---
YK20-18S-6K-1569R06B	Mado	Mylonitic Oxide gabbro	yes		60	30		10	---
YK20-18S-6K-1569R07B	Mado	Mylonitic Oxide gabbro	yes		50	45	?	5	---
YK20-18S-6K-1569R08A	Mado	Mylonitic Oxide gabbro	yes		55	35		10	--
YK20-18S-6K-1569R08B	Mado	Protomylonitic Oxide Gabbro	no		58	40		2	---
YK20-18S-6K-1569R09	Mado	Mylonitic Oxide gabbro	yes		45	40		20	
YK20-18S-6K-1569R010	Mado	Ultramylonitic Gabbro	yes		50	50			
KH18-2-D12R101	**Mado near Taransform Fault**	Protomylonitic Oxide Gabbro	no		60	30		10	--
KH18-2-D12R107	Mado	Protomylonitic Oxide Gabbro	yes		70	20	1	10	--
KH18-2-D12R111	Mado	Protomylonitic Oxide Gabbro	yes		55	30	5	15	---
YK22-16S-6K-1655R02A	**Tosa**	Oxide Diorite	no		70		20	10	--
YK22-16S-6K-1655R02B	Tosa	Oxide Diorite	no		55		30	15	--
YK22-16S-6K-1655R02C	Tosa	Oxide Diorite	no		70		30	10	--
YK22-16S-6K-1655R05A	Tosa	Oxide Diorite	no		55		40	5	--
YK22-16S-6K-1655R05B	Tosa	Oxide Diorite	no		45		50	5	--
YK23-05S-6K-1675R01	**Sanuki**	Dolerite	no		60		40		---
YK23-05S-6K-1675R02A	Sanuki	Oxide Diorite-Felsic Vein	no		58		40	2	--
YK23-05S-6K-1675R02B	Sanuki	Oxide Diorite	no		55		40	5	--
YK23-05S-6K-1675R02C	Sanuki	Oxide Diorite-Basalt	no		60		35	5	--
YK23-05S-6K-1675R02D	Sanuki	Oxide Diorite	no		60		35	5	--
YK23-05S-6K-1675R10A	Sanuki	Oxide Diorite	no		50		50	2	--
YK23-05S-6K-1675R11	Sanuki	Felsic Vein	no						---

4.2 Major and trace element compositions of the mineral phases

In this section, will be explained the geochemical composition of the main minerals, olivine, plagioclase, clinopyroxene and amphibole, composing the rocks under study. Major (SiO_2, TiO_2, Al_2O_3, Cr_2O_3, FeO, MgO, MnO, CaO, NiO, Na_2O, K_2O, ClO_2) and trace elements (V, Cr, Ni, Rb, Sr, Y, Zr, Nb, Cs, Ba, Hf, Ta, Pb, Th, U) analyses are from Basch et al. (2020). The methodologies used, such as laser ablation-inductively coupled plasma-mass spectrometry (LA-ICP-MS) and electron microprobe analyses (EPMA), are described in Basch et al. (2020). The results of the analysis data, corresponding to a series of points on the crystal, were processed into averages, taking into consideration only the points corresponding to the crystal core. The crystals were taken from each different lithology (olivine-gabbro, gabbro, oxide gabbro, oxide diorite, felsic veins) from Mado, Sanuki and Tosa.

4.2.1 Plagioclase

To understand the geochemical composition of plagioclase it was decided to relate the potassium dioxide content (wt%) to the Anorthite (Ca/Ca + Na) content (mol%), as seen in graph A. The anorthite content ranges from a minimum of 15 (mol%) to a maximum of 73 (mol%), indicating an anorthite composition for the plagioclases of the different lithologies. Figure 43 shows a very low K_2O content for all lithologies, ranging from 0 to 0.4, typical of oceanic environments. Furthermore, decreasing the anorthite content the K_2O content increases progressively. Specifically, the olivine-gabbro and the gabbro show a K_2O content < 0.1% and an anorthite content > 50 mol%, being the most primitive lithologies in the magmatic series. In fact, as the anorthite differentiates and the magmatic series advances, the K_2O content increases, albeit slightly, in the gabbro-oxide lithologies, diorite-oxides and felsic veins. The latter often have a peculiar behaviour.

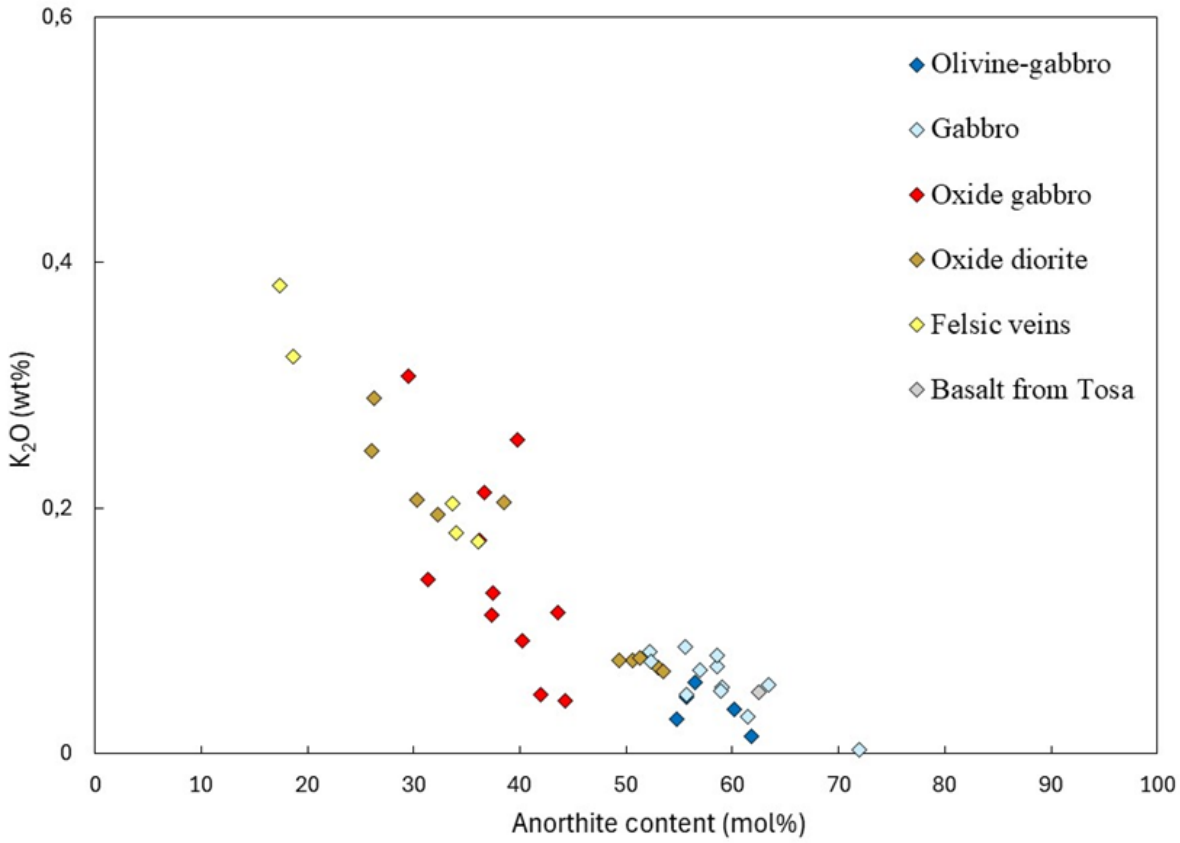

Figure 43: K_2O (wt%) vs Anorthite (Ca/Ca + Na) content (mol%).

4.2.2 Clinopyroxene

For the geochemical composition of clinopyroxene the graphs used were TiO_2 (wt%) vs Mg# (mol%) = [Mg2/(Mg2+Fe2)], Cr_2O_3 (wt%) vs Mg# and Al_2O_3 (wt%) vs Mg#, graph A, B and C respectively in figure 44. For comparison, these plots were implemented with the samples (n=8437) of Dick et al. (2002). The graph in Figure 44A shows a negative trend of TiO_2, which decreases at decreasing Mg#, i.e. as the crystallization series advances. On the contrary, in MOR environments TiO_2 increases until Mg# 75, then decreasing in the most evolved lithologies, as evidenced by the trend of the samples from Dick et al. (2002). Basch et al. (2020) interpreted the decrease in TiO_2 content in the Mado gabbros caused by the crystallization of magmatic amphibole. Mg# ranges from 80 to 85 (mol%) for olivine gabbros and gabbros, from 75 to 80 (mol%) for oxide diorites, and from 75 to 65 (mol%) for oxide gabbros. The TiO_2 content, however, ranges from 0.6 to 0.4 (wt%) for the most primitive lithologies, such as olivine-gabbro, gabbro and oxide diorites, while it is <0.4 (wt%) in oxide gabbros. Figure 44B also shows a trend with Cr_2O_3 that decreases as Mg# decreases and as the magmatic series advances. The Cr_2O_3 content tends to be extremely low, i.e. <0.2 wt% for almost all samples. Figure 44C shows a trend with Al_2O_3 decreasing as the Mg# decreases. The Al_2O_3 ranges between 3 and 1.7

wt% in olivine gabbro and in gabbros with Mg# from 75-80 (mol%), while Al_2O_3 is < 1.5 wt% for oxide gabbros and oxide diorites with Mg# 65-75 (mol%). Comparing with the gabbros from ODP Hole 735b, Southwest Indian Ridge (Dick et al., 2002), graphs B and C present the similar trends, despite the Shikoku Basin gabbros have slightly lower Al_2O_3.

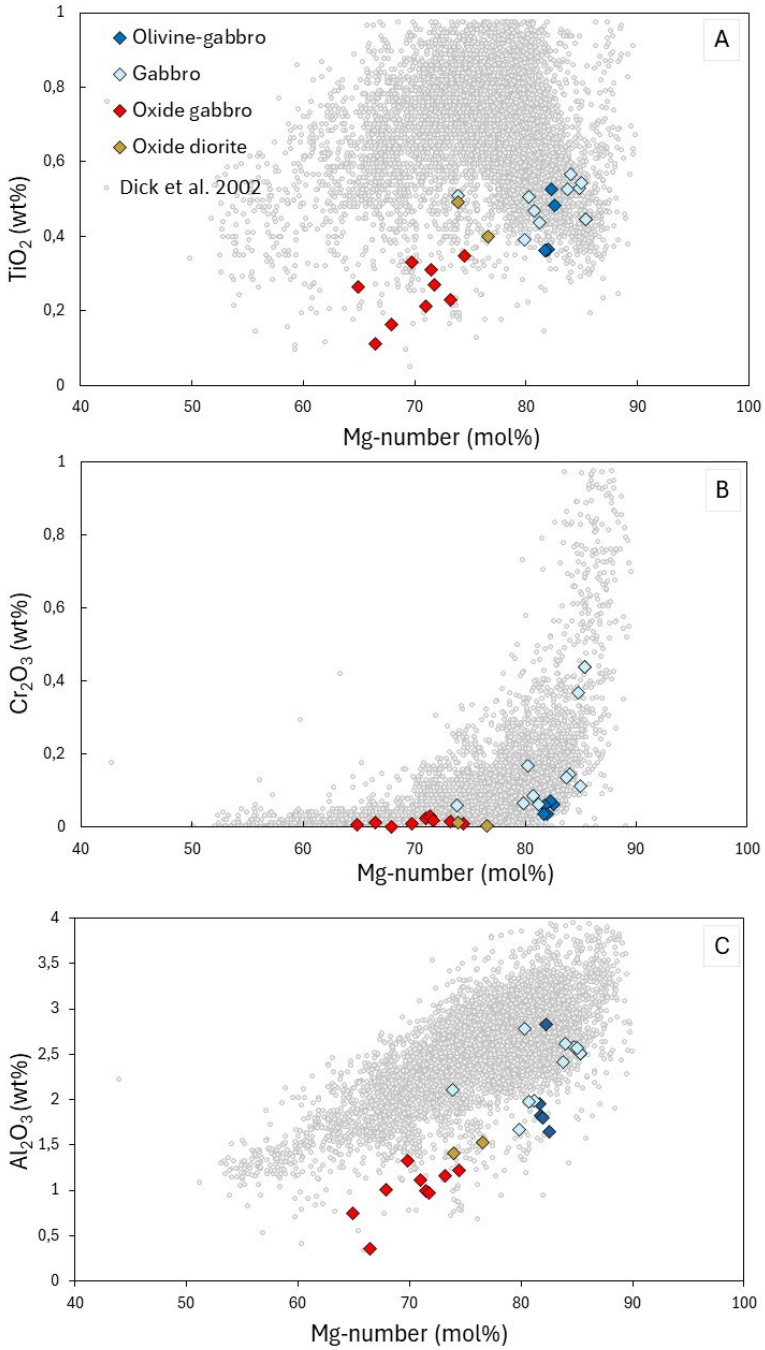

Figure 44: ***a)*** *TiO_2 (wt%) vs Mg# (mol%) = [Mg2/(Mg2+Fe2)],* ***b)*** *Cr_2O_3 (wt%) vs Mg# and* ***c)*** *Al_2O_3 (wt%) vs Mg#.*

The trace element compositions of clinopyroxene crystals are plotted on a graph relating the concentration (ppm) normalized to CI vs the atomic number (Z) of rare earth elements (REEs). Figure 45D contains samples from Mado, Figure 45F samples from Sanuki and Tosa. Since Earth

composition it's heterogeneous the concentrations are normalized to a reference standard such as the concentration of chondrites (CI), also to eliminate the Oddo-Harkins effect and make the logarithmic y scale more functional. The REE are arranged on a compatibility scale increasing from left to right, i.e. towards the right the atomic number increases (La 57, Lu 71) and the ionic radius decreases. These data are also plotted on a Spider Diagram which relates the concentrations normalized to the primitive mantle (PM) vs incompatible elements (Rb, Ba, Th, K, Sr), some REE (La, Ce, Eu, Yb, Y) and high charge atoms (Zr^{+4}, U, Ti^{+4}, P^{+5}). Also in this graph, from left to right the compatibility of the elements and their atomic number increases, while the ionic radius decreasess. Graph E (Fig.45) for samples from Mado and graph G (Fig.45) for samples from Sanuki and Tosa.

Graph D and F (Fig.45), show an increasing curve towards the more compatible elements, similar to a depleted mantle (DM) composition. It is also possible to note a clear distinction between the more primitive lithologies, such as olivine-gabbro and gabbro with lower concentrations (from 1 to 10 times CI) compared to the more evolved lithologies in the magmatic series, such as oxide gabbros and oxide diorites, with higher concentration (from 10 to 100 times CI). There is a negative anomaly in Eu because a good part of it formed plagioclase during crystallization, Eu being the only rare earth to have an isotope with a 2+ charge, this manages to slip into the crystalline lattice of plagioclase in place of the Ca^{2+}, moving from the melt. The depletion in Eu indicates that the melt from which the pyroxene crystallized was itself depleted in Eu.

The Spider Diagram E (Fig.45) shows a positive anomaly in U likely due to seawater alteration. Some lithologies as gabbros and some oxide gabbros have negative anomalies in Nb and K. The depletions in Pb, Sr and Ti are also evident in clinopyroxene from all lithologies. The negative anomalies of Sr are concordant with the anomaly in Eu, likely indicating the crystallization of Plagioclase. The negative Ti anomaly is very pronounced in Oxide-bearing lithologies and could be hence linked to the crystallization magmatic oxides. Cpx from Sanuki and Tosa (Fig.45) has the same negative Pb, Sr and Ti anomalies seen above, but does not show any positive anomaly in U, but its abundance tends to be very low. The only notable difference with cpx in gabbros from the rock selection is a stronger depletion in Nb and K in Tosa and Sanuki with respect to Mado (Nb/La 0,525952 and 0,962231 in Mado and Sanuki/Tosa, respectively).

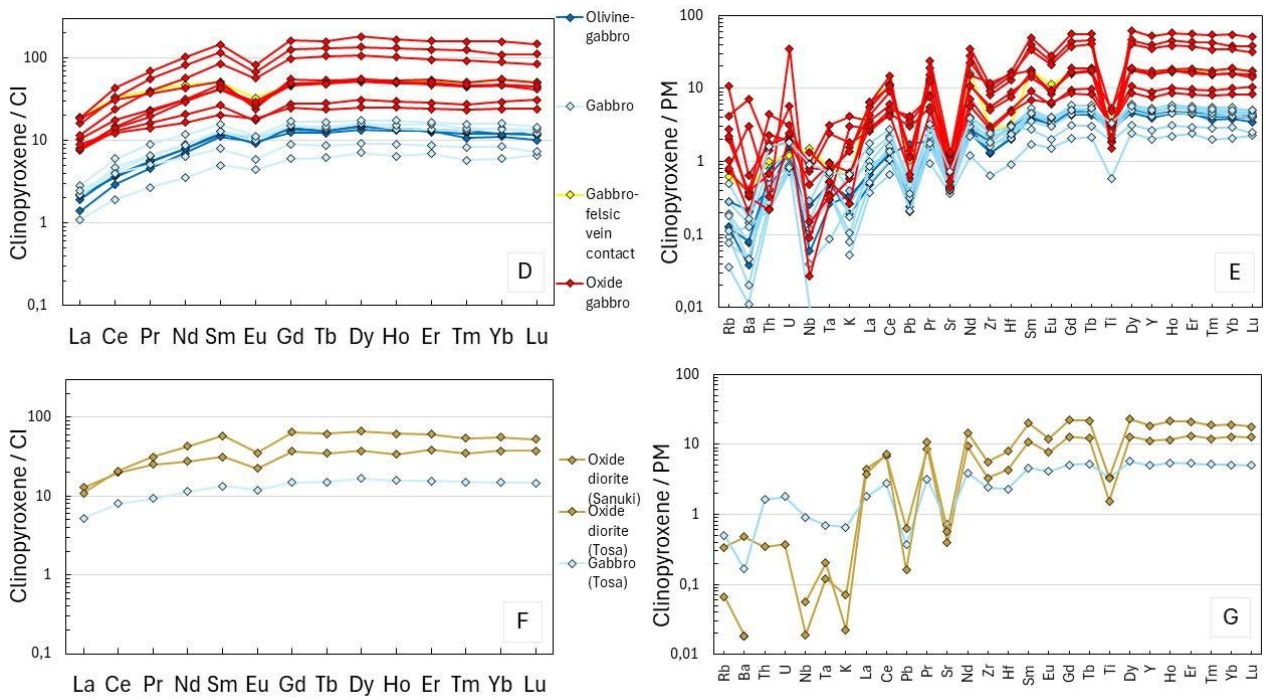

*Figure 45: **d)** Clinopyroxene/CI vs REE (samples from Mado Megamullion), **e)** clinopyroxene/PM vs incompatible elements (samples from MM), **f)** clinopyroxene/CI vs REE (samples from Sanuki and Tosa), **g)** clinopyroxene/PM vs incompatible elements (samples from Sanuki and Tosa).*

4.2.3 Amphibole

For the geochemical composition of amphibole, the graph of total alkali $(Na+K)_A$ vs silica content, expressed as atomic proportion per formula unit (apfu) of major cations, and the graph TiO_2 (wt%) vs Al apfu, are used. Graphs A and B (Fig.46) show samples from Mado, whereas graphs C and D (Fig.46) samples from Sanuki and Tosa, respectively. In all graphs, the rhombic-shaped symbols represent magmatic amphiboles, and the triangular-shaped ones represent low-temperature alteration amphiboles.

In figure 46A the alkali content decreases as the silica increases, crystals of magmatic origin have a higher alkali content of 0.4 - 0.8 for all lithologies for a content of Si from 6.3-7 apfu, while low-temperature alteration materials have (Na+K) content <0.4 apfu. down to ca. 0 apfu as silica increases from 7.1 to 7.9 apfu Figure 46C shows approximately the same trend.

Figure 46B shows a trend of increasing TiO_2 as Al increases, moving from low temperature alteration materials to magmatic materials. The magmatic minerals have high TiO_2 (4-2 wt%) and high Al (1.7-0.8 apfu). Low temperature alteration materials, on the other hand, have very low TiO_2 values <1 wt% with Al content ranging from 0.8 to 0.1 apfu. Figure 46D for Sanuki and Tosa samples have a very similar trend, with slightly higher values of about 0.5 apfu.

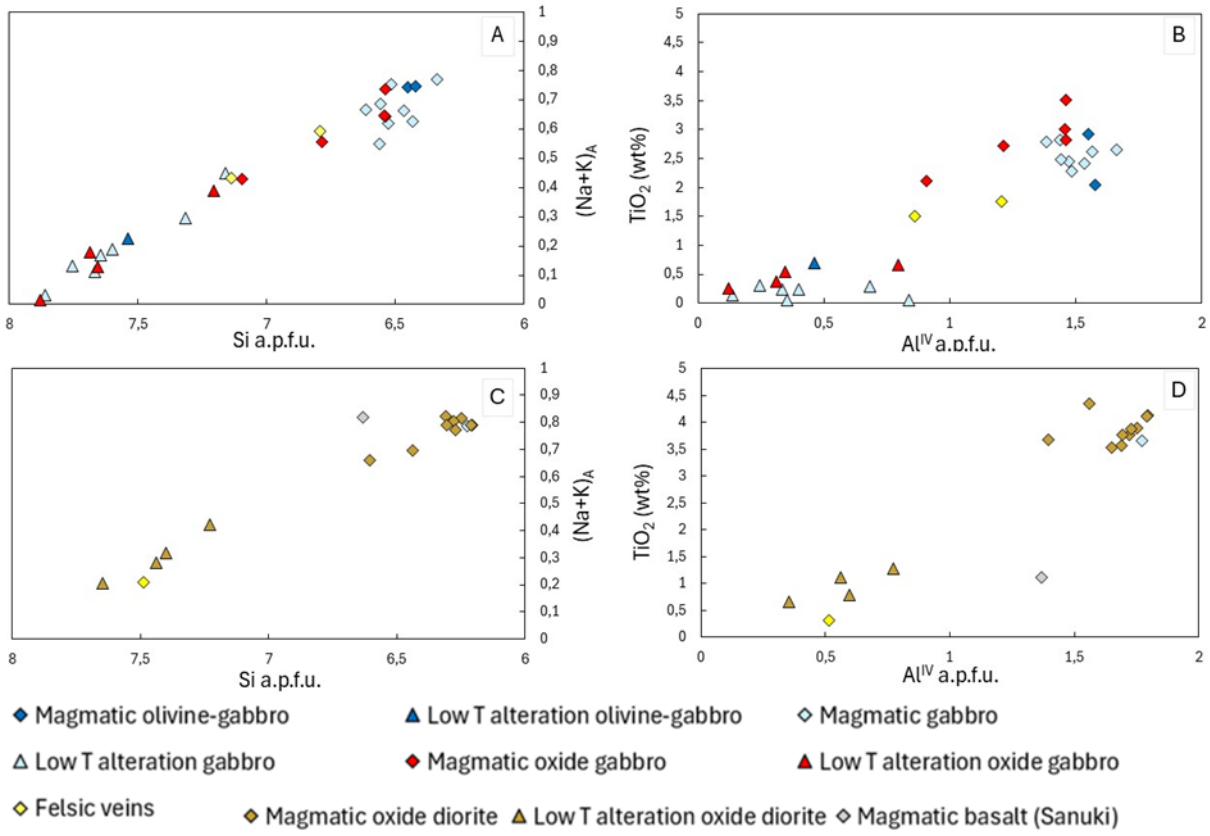

*Figure 46: **a)** Total alkali vs silica content (apfu) of samples from MM, **b)** TiO2 (wt%) vs Al apfu of samples from MM, **c)** Total alkali vs silica content (apfu) of samples from Sanuki and Tosa, **d)** TiO2 (wt%) vs Al apfu of samples from Sanuki and Tosa.*

The data resulting from trace elements analyses carried out on the amphibole crystals were plotted on concentration (ppm) normalised to CI vs REE, corresponding to graph E (Fig.47) for samples from Mado and graph G (Fig.47) for samples from Sanuki and Tosa. Data have been plotted also on the spider diagram having concentration (ppm) normalised to the PM vs incompatible elements, corresponding to graph F (Fig.47) for samples from Mado and graph H (Fig.47) for samples from Sanuki and Tosa. The graphs E and G (Fig.47) show a curve that increases towards the more compatible elements similar to the coexisting clinopyroxene. The lithologies representing the last phases of the magmatic series have higher abundances than the more primitive lithologies. The clear negative anomaly in Eu may be linked to the crystallisation of plagioclase, during which the Eu from the melt passes to the crystalline lattice of the plagioclase, depleting the melt more and more from which the clinopyroxene in turn depleted in Eu will crystallise. On the contrary, in graph G (Fig.47) we note a positive anomaly in Eu of the amphibole in basalt sampled at Tosa. Furthermore, the pattern of amphibole in a gabbro from Tosa sample has a slight enrichment in higly incompatible elements compared to those in the gabbros, similar to the coexisting cpx. This may be due to a slightly enriched signature of the melt forming the Tosa gabbros.

Finally, the felsic vein amphibole has a trend subparallel to that of oxide gabbro amphibole, but having lower Nb, Ta, Zr, Hf as likely result of oxide crystallization.

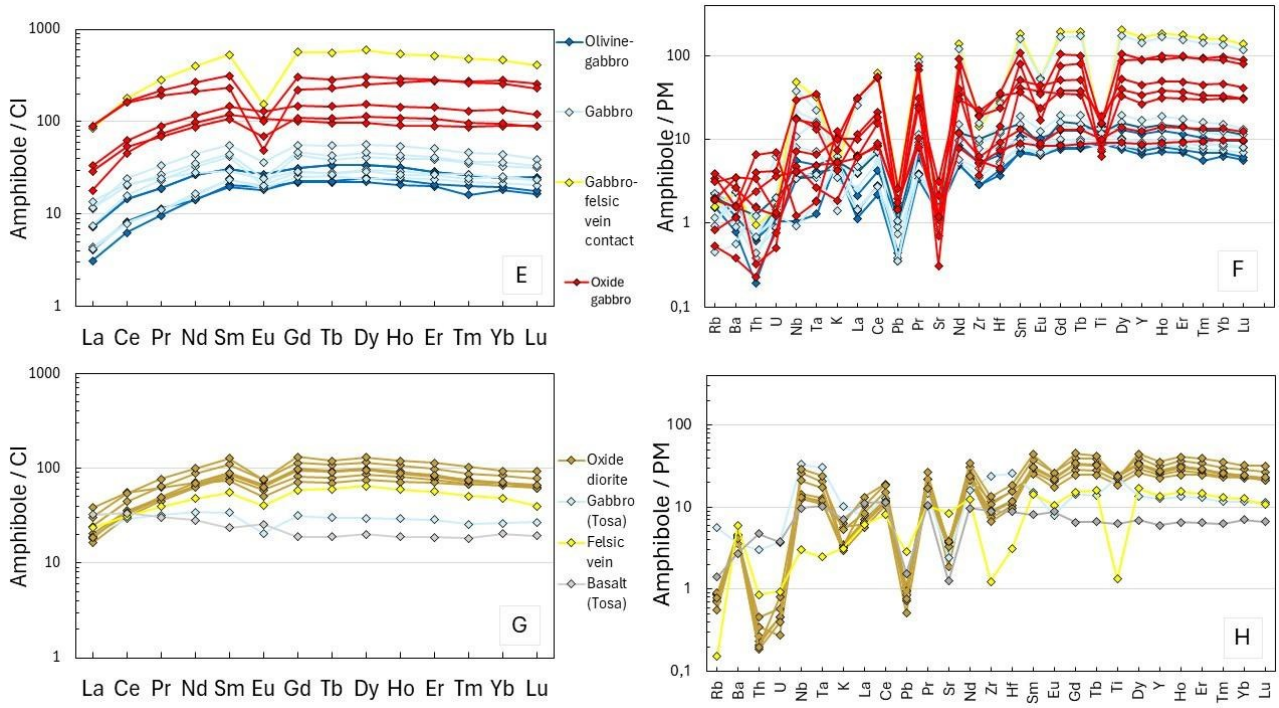

*Figure 47: **e)** Amphibole/CI vs REE samples from MM, **f)** amphibole/PM vs incompatible elements samples from MM, **g)** amphibole/CI vs REE samples from Sanuki and Tosa, **h)** amphibole/PM vs incompatible elements samples from Sanuki and Tosa.*

4.3 Isotopic compositions

Isotopic data of studied samples from Shikoku basin are shown in Figures 48 to 50. The present-day isotopic compositions are corrected to the initial age of crystallization defined in other stidies and reported in table 4. Gabbros from Mado Megamullion have initial $^{87}Sr/^{86}Sr$ of 0,70278 to 0,70339, initial $^{143}Nd/^{144}Nd$ of 0,51311 to 0,51314 (initial ε_{Nd}= 9,66 to 10,11), initial $^{206}Pb/^{204}Pb$ of 17,77621254 to 18,11759228. Oxide diorites from Tosa and Sanuki OCC show initial $^{87}Sr/^{86}Sr$ of 0,70295 to 0,70355, initial $^{143}Nd/^{144}Nd$ of 0,51309 to 0,51312 (initial ε_{Nd} = 9,36 to 9,97) and initial $^{206}Pb/^{204}Pb$ of 17,86527 to 18,08063. All collected samples have initial 208Pb/204Pb ratios higher than the North Reference line (NHRL), with Δ8/4 from +21 to +69. Almost all the samples, aside of two oxide-gabbro and one olivine-gabbro samples from Mado, show initial $^{207}Pb/^{204}Pb$ ratios higher than the NHRL, with Δ7/4 from +0,32 to +15.

Table 4: Sample name and location, minerals separate for isotopic analysis and Sr, Nd and Pb radiogenic ratios.

Sample	Age (Ma)	Sampled Area	Lithology	Separate	$^{87}Sr/^{86}Sr_i$	$^{143}Nd/^{144}Nd_i$	εNd	$^{206}Pb/^{204}Pb_i$	$^{207}Pb/^{204}Pb_i$	$^{208}Pb/^{204}Pb_i$
AYK19-04S-6K-1536R10	12,5	Mado central	Gabbro varitext	Cpx	0,702960	0,513118	9,6	18,108	15,501	37,949
AYK19-04S-6K-1536R14B	12,5	Mado central	Gabbro varitext	Cpx	0,702938	0,513130	9,9	18,052	15,505	37,877
AYK19-04S-6K-1536R16	12,5	Mado central	Gabbro	Cpx	0,702952	0,513139	10,08	17,934	15,441	37,521
AYK19-04S-6K-1536R18	12,5	Mado central	Ol gabbro	Cpx	0,702826	0,513117	9,6	17,881	15,483	37,629
AYK19-04S-6K-1536R20	12,5	Mado central	Ol gabbro	Cpx	0,702788	0,513136	10,02	17,797	15,412	37,427
KH18-2-D05R101A	12,5	Mado central	Gabbro varitext	Cpx	0,703239	0,513135	10,02	18,117	15,551	38,038
KH18-2-D05R101F	12,5	Mado central	Felsic vein	Cpx	0,702832323	0,513138	10,07	17,874	15,478	37,662
YK18-07S-6K-1515R04	12,5	Mado near Transform Fault	Mylonitic Oxide Gabbro	Cpx	0,703396	0,513132	9,9	17,877	15,420	37,533
YK18-07S-6K-1515R14	12,5	Mado near Transform Fault	Protomylonitic Oxide Gabbro	Cpx	0,703053	0,513123	9,7	18,019	15,477	37,782
YK20-18S-6K-1569R07B	12,5	Mado near Transform Fault	Mylonitic Oxide gabbro	Cpx	0,702864	0,513140	10,11	17,797	15,418	37,448

YK20-18S-6K-1569R08A	12,5	Mado near Transform Fault	Mylonitic Oxide gabbro	Cpx	0,702864	0,5131405	10,11	17,781	15,429	37,444
YK20-18S-6K-1569R09	12,5	Mado near Transform Fault	Mylonitic Oxide gabbro	Cpx	0,702993	0,5131359	10,02	17,875	15,492	37,696
KH18-2-D12R111	12,5	Mado near Transform Fault	Oxide Gabbro	Cpx	0,703043			17,837	15,431	37,505
YK22-16S-6K-1655R02	21,0	Tosa	Oxide Diorite	Amph	0,703046	0,5130913	9,36	17,897	15,452	37,718
YK22-16S-6K-1655R05	21,0	Tosa	Oxide Diorite	Amph	0,703026	0,5130955	9,45	18,080	15,600	38,174
YK23-05S-6K-1675R02A	21,0	Sanuki	Oxide Diorite-Felsic Vein	Amph	0,702955	0,5131221	9,97	17,880	15,440	37,695
YK23-05S-6K-1675R02C	21,0	Sanuki	Oxide Diorite-Basalt	Amph	0,702987	0,5131106	9,74	17,987	15,471	37,844
YK23-05S-6K-1675R10A	21,0	Sanuki	Oxide Diorite	Amph	0,703118	0,5131115	9,76	17,912	15,479	37,821
YK19-04S-6K-1536R20F	12,5	Mado central	Felsic vein	WR	0,702807	0,5131372	10,05	17,776	15,421	37,438
YK23-05S-6K-1675R02F	21,0	Sanuki	Felsic vein	WR	0,703432	0,5131023	9,58			
YK23-05S-6K-1675R11	21,0	Sanuki	Felsic vein	WR	0,703558	0,5131054	9,64	17,960	15,485	37,854

YK23-05S-6K-1675R02 B	21,0	Sanuki	Basalt	WR	0,703096	0,5131161	9,85	17,865	15,470	37,762

There are differences depending on the lithology or geographical location, therefore the ages and the corresponding opening phase of the back-arc basin. Samples from Mado have a higher Nd content and lower Pb (Fig.50A). However, the Cpx separated from the gabbros have a higher Pb isotope ratio than those separated from the olivine-gabbro. More variability in the Nd/Sr ratios, one oxide gabbro and two felsic veins from the Mado have anomalous Sr compositions (Fig. 48B), attributable to sea water. Another anomaly is the high content in $^{207}Pb/^{204}Pb$ showed by an oxide-diorite sample from Tosa (Fig.49C).

Comparison with literature data is provided in graphs 48 to 50, where we report intrusive rocks derived by boninites magmas from Marianna forearc erupted at 48–43 Ma (Johnson et al., 2014), basalts from the Shikoku basin floor, with an age from 17.28-19.93 Ma (Ishizuka et al., 2007) and basalts 15.48-7.73 Ma old from the Kinan seamount chain, the East Shikoku basin seamounts, the Back-arc seamount chain, the Kinan Escarpment (Ishizuka et al., 2007) and from DSDP sites 442B, 443 and 444A (H.Vargas, 1990-1991). Also shown are tonalites from the Mariana trench, recently sampled on the subduction wall north of Challenger Deep (Basch, unpublished).

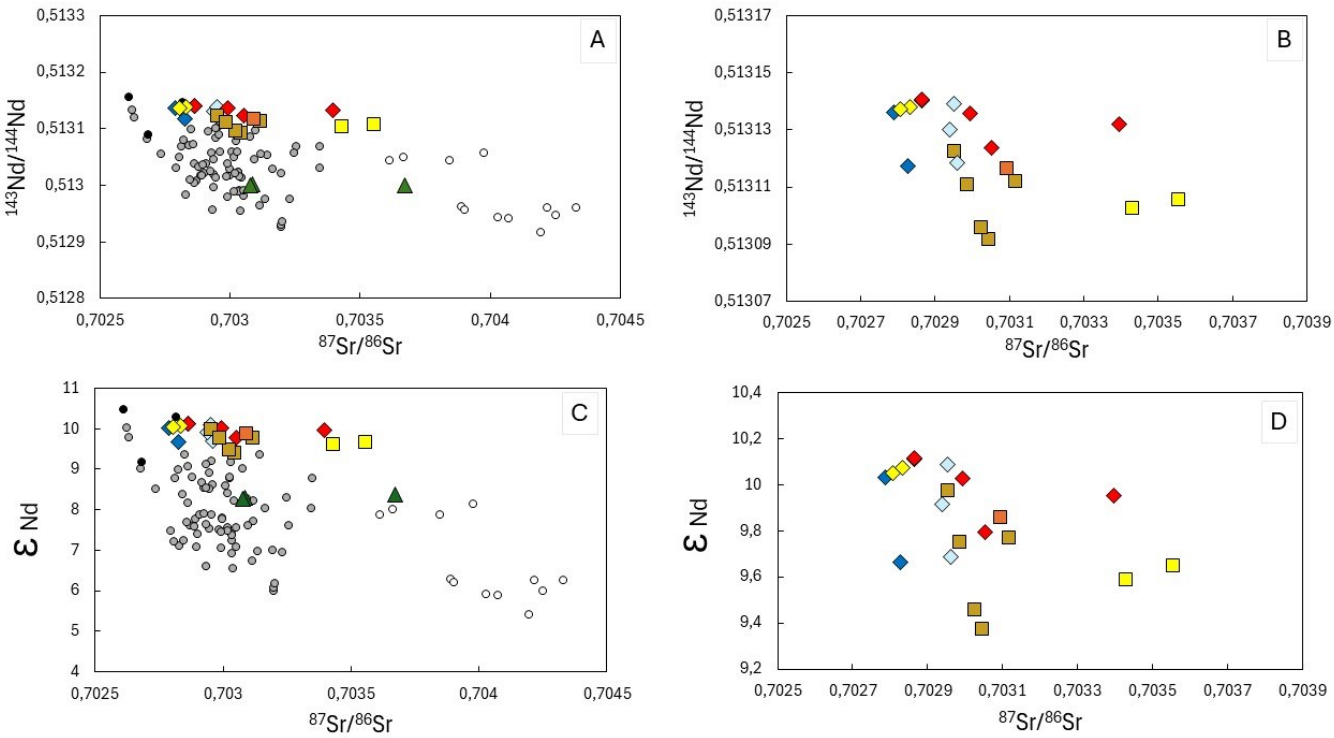

Figure 48 Isotopic data of Sr and Nd: a) initial $^{144}Nd/^{143}Nd$ vs initial $^{87}Sr/^{86}Sr$ of understudied samples and literature samples; b) initial $^{144}Nd/^{143}Nd$ vs initial $^{87}Sr/^{86}Sr$ focused just on samples understudied; c) initial εNd vs initial $^{87}Sr/^{86}Sr$ of samples from Mado, Tosa, Sanuki, Kinan seamount chain, Shikoku basin floor, Mariana Trench and Mariana forearc; d)) initial εNd vs initial $^{87}Sr/^{86}Sr$ focused on samples from Mado, Tosa, Sanuki.

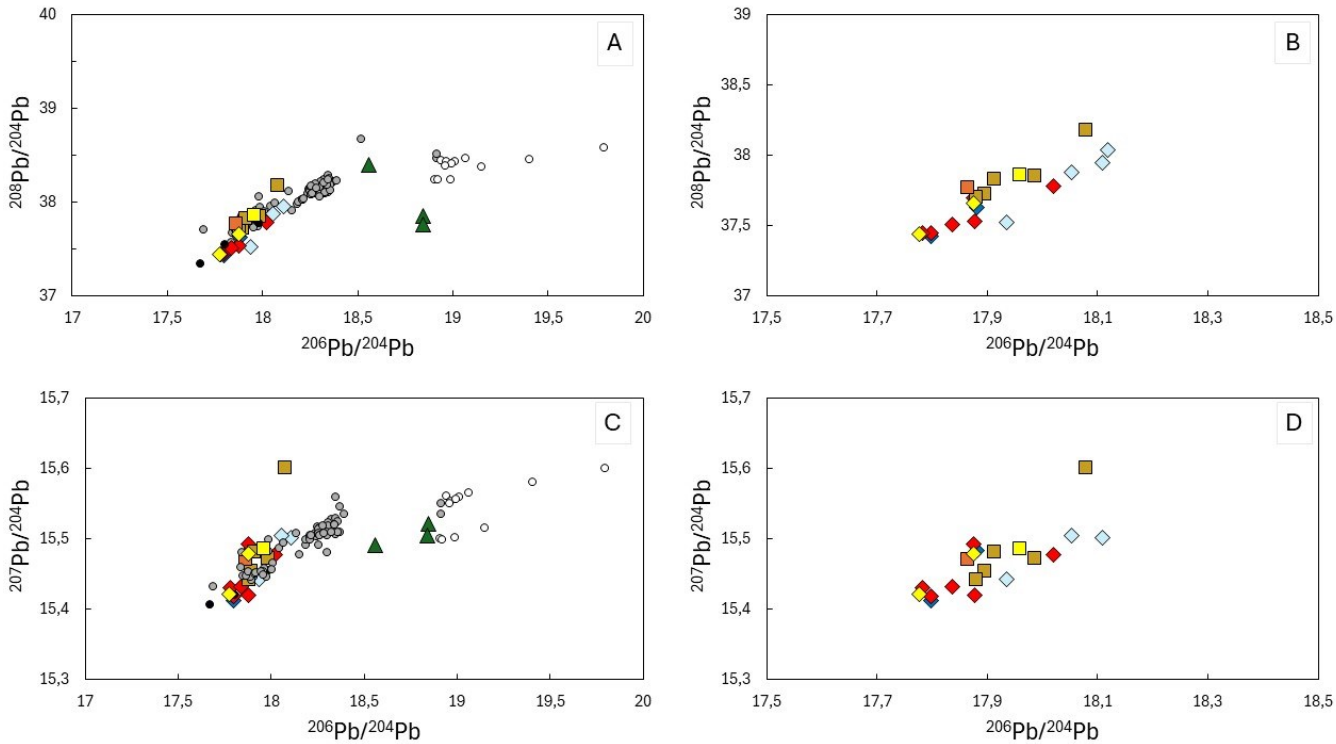

Figure 49 Isotopic data of Pb: a) initial $^{208}Pb/^{204}Pb$ vs initial $^{206}Pb/^{204}Pb$ of samples from different areas of Shikoku basin and from the Mariana trench and forearc; b)) initial $^{208}Pb/^{204}Pb$ vs initial $^{206}Pb/^{204}Pb$ of samples from Mado,Tosa and Sanuki; c) initial $^{207}Pb/^{204}Pb$ vs $^{206}Pb/^{204}Pb$ of samples from different areas of Shikoku basin and from the Mariana trench and forearc; d)) initial $^{207}Pb/^{204}Pb$ vs initial $^{206}Pb/^{204}Pb$ of samples from Mado ,Tosa and Sanuki

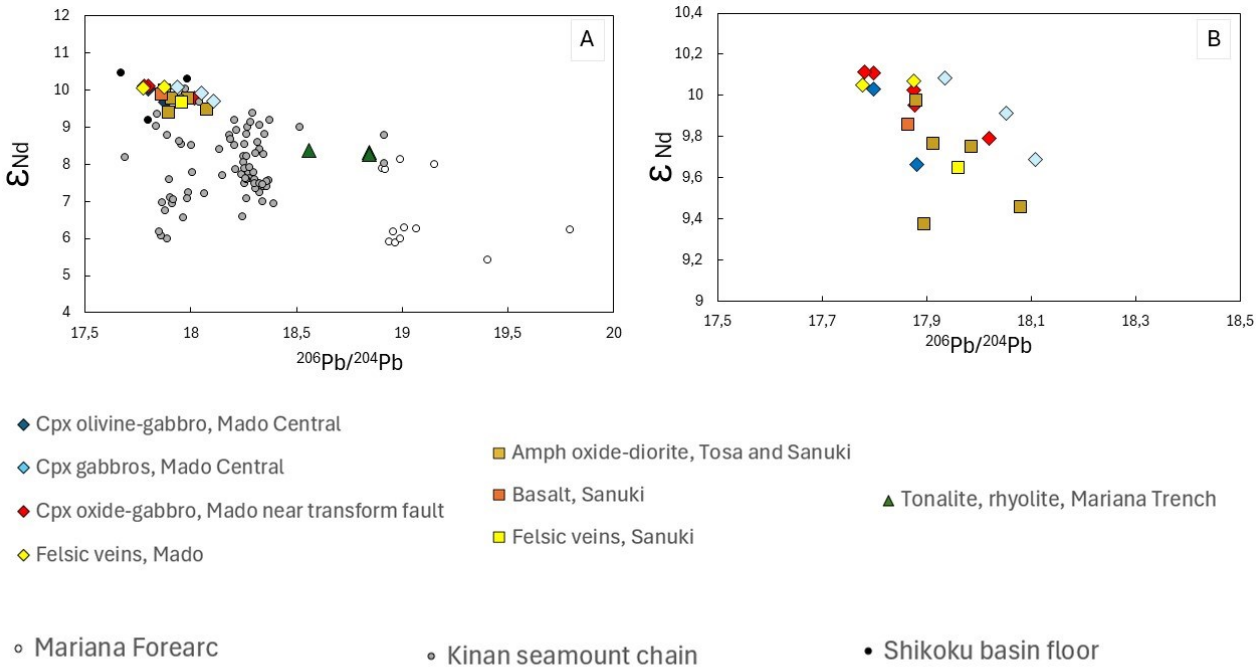

Figure 50: a) initial εNd vs initial $^{206}Pb/^{204}Pb$ of samples from Mado, Tosa, Sanuki, Kinan seamount chain, Shikoku basin floor, Mariana Trench and Mariana forearc; b) initial εNd vs initial $^{206}Pb/^{204}Pb$ of samples from Mado, Tosa, Sanuki.

In all the graphs there is a good correlation / overlap between the studied samples and the basalts recovered in the different areas of the Shikoku Basin, while they deviate from the samples from the Marianna trench and the Marianna forearc. However, we note that samples from Mado Tosa and

Sanuki OCCs have slightly higher values of $^{143}Nd/^{144}Nd$ than the basalts from the nearby Kinan seamount chain for a given $^{206}Pb/^{204}Pb$. On the other hand, basalts from the Shikoku basin floor have higher $^{143}Nd/^{144}Nd$ than the intrusive OCC samples from this study, or they show a perfect overlap. The composition of $^{208}Pb/^{204}Pb$ and $^{207}Pb/^{204}Pb$ tend to increase with increasing $^{206}Pb/^{204}Pb$ for all the samples. Finally, it is possible to mark 3 main trends: Shikoku basin, Marianna Trench and Marianna forearc, which show an increase of $^{87}Sr/^{86}Sr$, a decrease of $^{143}Nd/^{144}Nd$ vs $^{206}Pb/^{204}Pb$ (Fig.51) and an increase of $^{208}Pb/^{204}Pb$ and $^{207}Pb/^{204}Pb$ vs $^{206}Pb/^{204}Pb$.

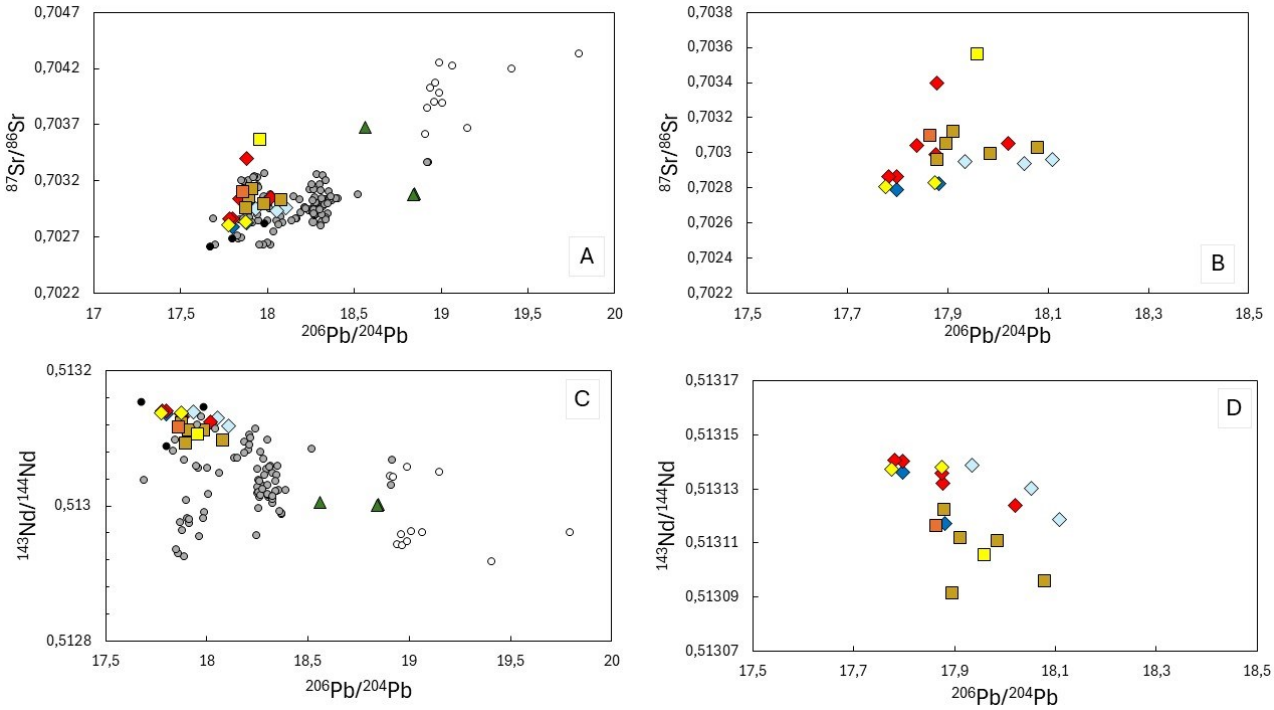

Figure 51: a) initial $^{87}Sr/^{86}Sr$ vs initial $^{206}Pb/^{204}Pb$ of samples from Mado, Tosa Sanuki , Kinan seamount chain, Shikoku basin floor, Mariana Trench and Mariana forearc; b) initial $^{87}Sr/^{86}Sr$ vs $^{206}Pb/^{204}Pb$ of samples from Mado, Tosa Sanuki; c) initial $^{143}Nd/^{144}Nd$ vs initial $^{206}Pb/^{204}Pb$ of samples from Mado, Tosa Sanuki , Kinan seamount chain, Shikoku basin floor, Mariana Trench and Mariana forearc; d) initial $^{143}Nd/^{144}Nd$ vs initial $^{206}Pb/^{204}Pb$ of samples from Mado, Tosa Sanuki.

CHAPTER 5 – DISCUSSION AND CONCLUSIONS

5.1.1 Petrographic evidence

Tosa and Sanuki Megamullions have an age of 21 Ma and represent the initial phases of the opening of the Shikoku basin, while Mado OCC is 12.5 Ma and corresponds to the final phases of back-arc extension. The petrographic study conducted on thin sections obtained from hand-selected samples reveals lithologies corresponding to different magmatic series based on the sampling area. In the central part of the Mado Megamullion occur olivine-gabbros, which represent the most primitive lithology of the tholeiitic magmatic series, followed by gabbros s.s. and chemically evolved varitextured gabbros. The varitextured gabbros are characterized by zones in which the crystals (plg, cpx) develop in a radial shape and with irregular dimensions, possibly formed as melt droplets that crystallize in-situ at lowering temperature, with no input of new magmas. These lithologies appear undeformed and are variably altered during hydration processes. The gabbros are intersected by a series of felsic veins attributable to sialic evolved melts that rise through fractures crosscutting the gabbros. The samples from the Mado OCC near the transform fault instead are oxide gabbros, representing the most evolved lithologies of the magmatic serie. Contrary to the central area, these lithologies are strongly deformed and mylonized likely due to a combination of detachment faulting and transform tectonics. By analysing the mineralogical associations within the mylonitic bands, the granulitic and amphibolitic metamorphic facies were identified.

Samples from Tosa and Sanuki are mainly oxide diorite, representing products of the evolution from primitive gabbros to more evolved lithologies. Interesting, the composition of these rocks requires silica-rich melts with high water contents and are never observed at the Mado OCC. Felsic veins and a sialic intrusion were also found at Tosa and Sanuki. The highest water content found in samples from Tosa and Sanuki suggest fluids influx during the melting process.

5.1.2 Major and trace elements

The analysis of the major elements on plagioclase crystals reveals variable anorthite composition which decrease at increasing K_2O content from the primitive to the more evolved lithologies. In clinopyroxene crystals, TiO_2, CrO_3 and AlO decrease at decreasing Mg# from the most primitive to the most evolved lithologies. Decreasing in Cr and Al is compatible with fractionation of clinopyroxene, spinel and anorthitic plagioclase, as typically seen in MOR gabbros. On the other hand, Ti generally increases at MOR gabbros, until it reaches a maximum corresponding to the saturation of Ti-Fe oxides. The discrepancy between MOR gabbros and our samples can be related to the early crystallization of magmatic oxides, commonly associated with amphibole in nearly all samples. This feature indicates high fugacity in the primary melts, likely due to the influx of water-

rich fluids during the melting process. Analyses of amphibole indicate that crystals of magmatic origin are extremely common, and have a higher alkali content, high TiO_2 and high Al, which can be easily distinguished from secondary amphibole related to low-temperature alteration. Trace elements analysis on clinopyroxene and amphibole show in both minerals the typical patterns of minerals in equilibrium with MORB-type melts, having fractionation in LREE and increasing toward the more compatible elements. Higher incompatible element concentrations are found in the most evolved lithologies, in agreement with processes of fractional crystallization. Crystals of all samples have depletion in Eu and Sr, indicating previous crystallization of plagioclase, in agreement with textural compositions. The only differences are seen in an amphibole crystal from Tosa basalt that, on the contrary, shows a positive anomaly in Eu, and in amphiboles from a gabbro from Tosa MM, which shows preferential enrichments in highly incompatible elements. The latter can be due to a slightly enriched signature of the melt forming the Tosa MM gabbros.

5.1.3 Isotopic compositions and geodynamic implication

The Pacific-type and Indian-type MORB isotopic source domains in the upper mantle are clear distinct. The Indian mantle domain (~10^8 km^2) is centred in the Indian Ocean and it is delineated by oceanic island and oceanic crust basalts having anomalous Sr, Nd and Pb isotopic signatures. This isotopic mantle domain, characterized by the Dupal anomaly (after Dupré and Alègre, 1983), can be traced nearly continuously around the Southern Hemisphere between the Equator and 60°S (Hart, 1984). The Indian-type mantle domain is a long-lived feature that can be traced back to, at least, the Palaeozoic (Mahoney et al., 1998). Isotopic data for Cretaceous Pacific MORB indicate the Pacific-type mantle domain has existed since ~200 to 150 Ma (Janney and Castillo, 1997; Mahoney et al., 1998), however, it was probably already present before the formation of the Pacific Ocean since the Precambrian (Scotese, 2009). Both domains are long-lived and large, linked to the core-mantle-crust differentiation processes, early in Earth history. This portions, not fully delineated yet, manifests the global-scale mantle compositional heterogeneities. In detail, the Indian-type mantle domain is characterized by higher $^{208}Pb/^{204}Pb$, $^{87}Sr/^{86}Sr$, and lower $^{143}Nd/^{144}Nd$ at a given $^{206}Pb/^{204}Pb$ compared to the Pacific-type mantle, and can be well identified using Sr-Nd-Pb systematics.

Comparing our samples with the NHRL (Fig. 52), obtain from essential collinearity of MORB and OIB (Hart, 1984), we infer that the Shikoku basin samples were produced by a source belonging to the Indian mantle domain. This feature is peculiar because geographically the Shikoku Basin is part of the Pacific Ocean, although we must consider that towards the southeast, along the Izu-Bonin-Mariana arc, there is a large subduction zone, where the Pacific plate subducts the overlying Philippine oceanic plate. This study, in agreement with previous works on the isotopic signature (Vargas 1998, Ishizuka 2008, Qian 2024), confirms that the Philippine Sea mantle is distinct from the

Pacific domain mantle since the very early stages of opening and formation of the Shikoku back-arc basin (i.e. since 21 Ma).

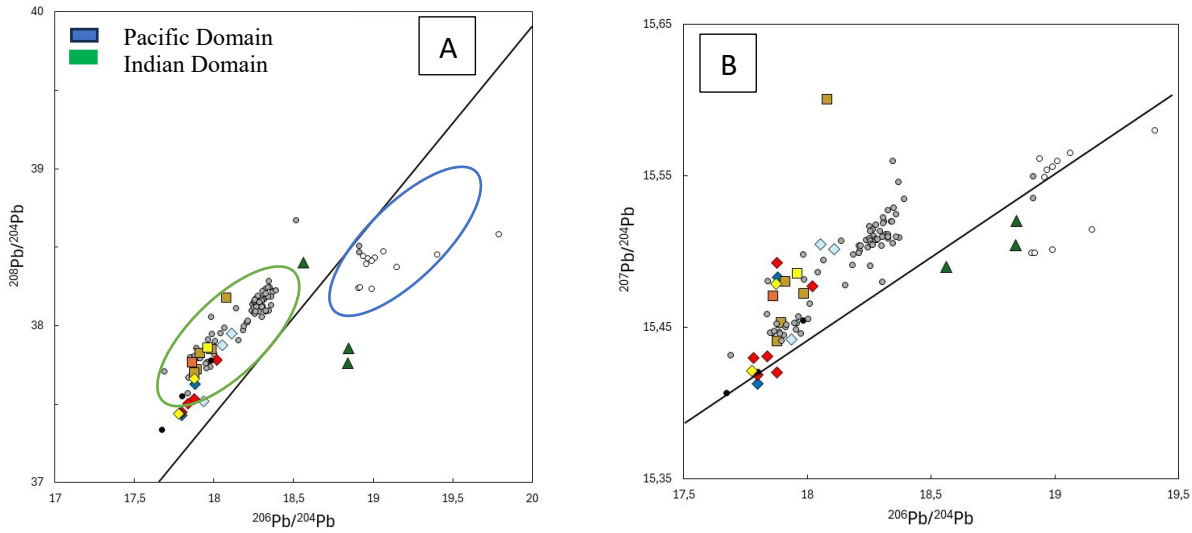

Figure 52: A)$^{208}Pb/^{204}Pb$ vs $^{206}Pb/^{204}Pb$ with North Reference line, green circle for the Indian domain and blue circle for the pacific. B) $^{207}Pb/^{204}Pb$ vs $^{206}Pb/^{204}Pb$ with NRL as reference to identify Indian and Pacif domains.

Subduction zones may or may not contribute to the contamination of the mantle source. An example of contamination are subduction fluids that can transport sediments from the continental or oceanic crust enriching the mantle source. On the contrary, there are also depleted or strongly depleted sources that can derive from melt extraction, which occur in rocks with depleted isotopic signature due just to the source itself.

The sampling areas in our study are of two different ages, and we can make considerations on the composition of the mantle source from a temporal point of view. Going from Tosa and Sanuki (21 Ma) to Mado MM (12 Ma) the samples show an increase of Nd isotope ratio and a decrease in Sr and Pb isotope ratio with time. This would indicate a slight change in mantle source from the initial to the final phases of spreading, which, despite being DM-like in composition, seems to be more enriched at the beginning of the basin opening. Since the timing of the exhumation of Mado Megamullion corresponds to the very end of the spreading of Shikoku Basin (Okino et al., 2001, Akizawa et al., 2021) the distance from the back-arc spreading center to the arc front increased away through maturing of Shikoku Basin. This may explain the gradual depletion in the mantle source. The DM-like signature of the Mado gabbros is in accordance with previous in-situ Pb isotope analysis of magmatic brown amphibole shows tight ranges of $^{207}Pb/^{206}Pb$ (0.866–0.879) and $^{208}Pb/^{206}Pb$ (2.114–2.123), which overlaps with values of depleted MORB source mantle (Akizawa et al. 2021).

The Mariana trench and Mariana forearc samples, instead, may have similarities with EM-like reservoir, having very high Sr and Pb compositions. Previous studies in this area (Johnson et al.,2014) have established through analysis of major elements, trace elements and isotopic compositions that the rocks present along the arc derive from boninitic magmatic sources or in any case from sources more enriched than the Indian domain. The boninite parent magma would have incorporated Pb and Nd from pelagic sediment, resulting in lower $^{143}Nd/^{144}Nd$, lower $^{206}Pb/^{204}Pb$ and higher $^{207}Pb/^{204}Pb$ and $^{208}Pb/^{204}Pb$ than Shikoku basin samples.
This is likely the effect of melting oceanic sediments close to the subduction zone. The forearc of the southern Mariana arc preserves igneous suites formed during the initiation of subduction between the Pacific and Philippine Sea plates about 50 Ma ago (Johnson et al.2014).

The post-spreading volcanism (12 to 3.6 Ma), on the other hand, is geochemically enriched in Nd and, to less extent, Pb isotopes, which are distinct from the rest of the Shikoku basin. This enrichment of the mantle in the late stages of ocean opening could be due to low degrees of partial melting caused by the presence of a stagnant slab and the thinning of the lithosphere, which melted preferentially enriched lithologies (Ishizuka et al. 2008). The post-spreading volcanism is associated with the formation of Kinan Seamount Chain (Ishizuka et al. 2009) and derived by residual mantle upwelling beneath the extinct back-arc spreading center.

Our data indicates that since the beginning of the back arc opening, the spreading ridge and arc front were well-separated, and that the subduction component was not added to the source mantle beneath the back arc spreading center.

5.2 Synthesis and geodynamic implication

The mantle of the Philippine Sea is of Indian relevance, at least until the formation of the Shikoku (25-15Ma), and has remained isolated from the Pacific subduction. Although a small temporal variation can be defined from the beginning to the final stages of the formation of the Shikoku basin. This small variation shows how over time the mantle source beneath the basin and the expansion center has become more depleted. In the initial phases (21Ma) in fact there is a slightly more enriched isotopic signature although still of Indian type. Analyzing the geodynamic context (Fig.53), the first phases of opening of the basin also correspond to a smaller distance from the volcanic arc (today paleo arc Kyoshu-Palau ridge) and from the subduction zone and from the slab. These elements could have influenced a minimum the depleted mantle source beneath the expanding basin. As can be understood, the final phases of the opening of the basin (12Ma)

correspond to the moment in which there was a greater distance from the subduction zone of the Pacific Plate. Following the chronology, after the end of the basin formation and the subduction zone movement, post-spreading volcanism occurred. This is a suite of rocks showing higher ^{206}Pb (low ^{208}Pb) and Sr and lower Nd. During this phase of the evolutionary history of the Shikoku basin, post-spreading volcanism could have been characterized by a series of bubbles of heterogeneous mantle more enriched with an OIB-like signature. The portions of the mantle in question would be those that during the opening of the basin when (21-12Ma) the subduction system was still active, the oceanic slab had influenced parts of the mantle enriching them with Pb and Sr. These enriched portions, at the time they were formed, remained isolated without influencing the magmatism during the spreading (Fig.53 A). It is only after the formation of the basin, stimulated by post-spreading volcanism, through upwelling (Fig. 53B), that they influenced the volcanic edifices that we analyze today. The enriched signature of the forearc instead has been interpreted because of the influence due to the percolation of subduction fluids inside the mantle source. These fluids transporting continental pelagic sediments can 'insert' Pb and Sr into the composition of the mantle source, which are easy to identify in the isotopic study. Since the arc is in contact with the subduction zone of the oceanic plate still in progress, it makes a lot of sense that this is influenced by it.

The first impressions due to the petrographic study, of the samples recovered directly from the OCCs of the Shikoku basin floor, focused on the strong presence of magmatic amphibole had made us ask questions related to the strong presence of fluids. However, thanks to the more complete study obtained through isotopic analysis, we were able to exclude the presence of subduction fluids or fluids with dissolved sediments inside to justify the presence of magmatic amphibole. We believe, however, that clearly the massive development of magmatic amphibole is linked to the presence of a wet component inside the mantle source. In practice, the hydrated mantle underlying the Philippine Sea would be affected by the circulation of fluids that have allowed the formation of amphiboles of this kind. Therefore, future isotopic study is highly recommended in order to define whether the mantle in these areas is actually characterized by a wet component.

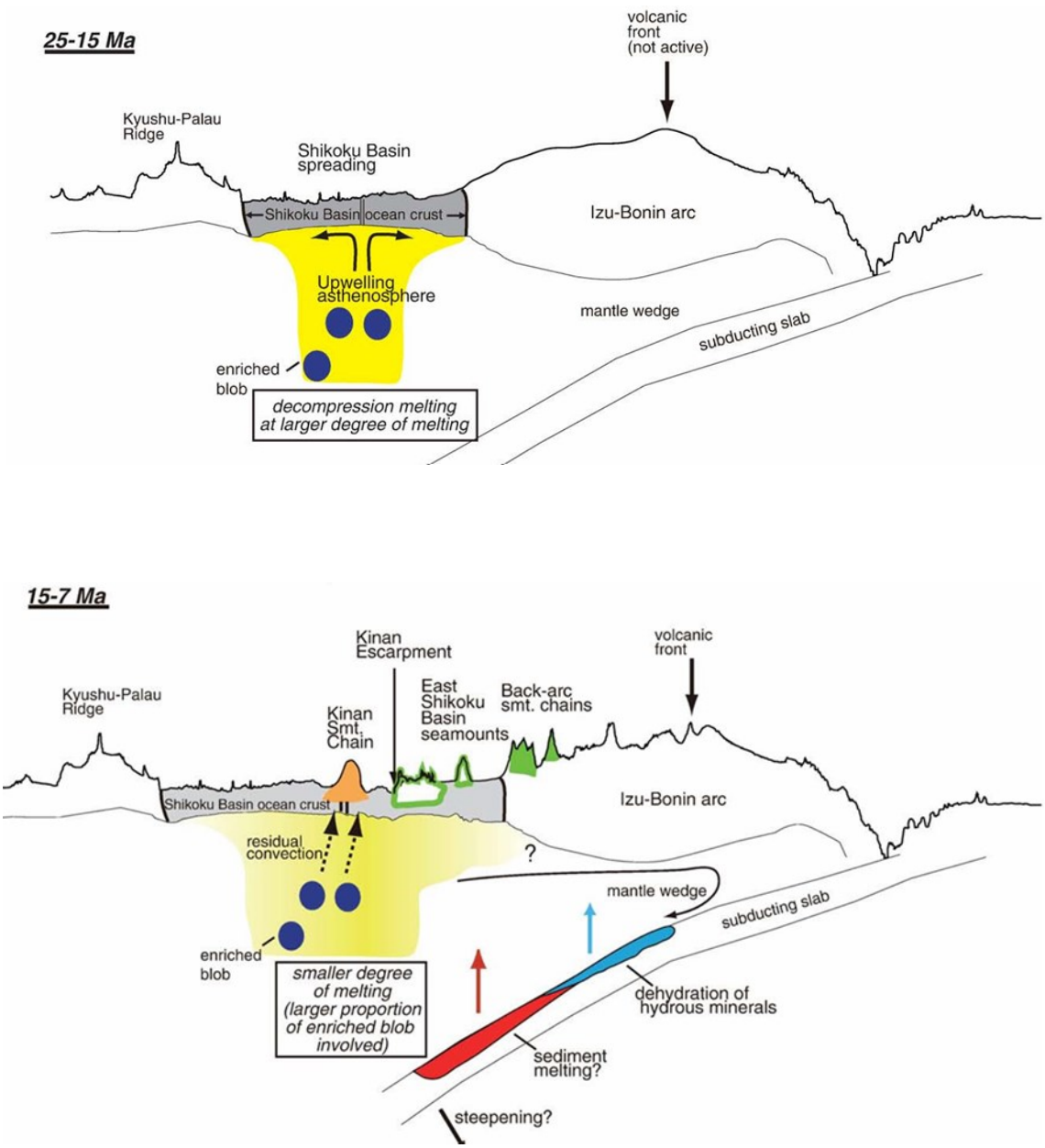

Figure 53: Evolution of Shikoku basin opening trough time from 25 to 7 Ma. A) Beginning of the Shikoku spreading without any subduction slab influence in the mantle source that fed the Shikoku basin crust. B) Post-spreading volcanism with influence from enriched blob derived by the previous slab subducted. (Ishizuka et al. 2008)

CHAPTER 6 - BIBLIOGRAPHY

A.W. Hofmann,3.3 - Sampling Mantle Heterogeneity through Oceanic Basalts: Isotopes and Trace Elements, Editor(s): Heinrich D. Holland, Karl K. Turekian, Treatise on Geochemistry (Second Edition), Elsevier, 2014, Pages 67-101, ISBN 9780080983004, http://doi.org/10.1016/B978-0-08-095975-7.00203-5

Akizawa, N., Ohara, Y., Okino, K. *et al.* Geochemical characteristics of back-arc basin lower crust and upper mantle at final spreading stage of Shikoku Basin: an example of Mado Megamullion. *Prog Earth Planet Sci* 8, 65 (2021). https://doi.org/10.1186/s40645-021-00454-3

Basch, V., Sanfilippo, A., Sani, C., Ohara, Y., Snow, J., Ishizuka, O., et al. (2020). Crustal accretion in a slow spreading back-arc basin: Insights from the Mado Megamullion oceanic core complex in the Shikoku Basin. *Geochemistry, Geophysics, Geosystems*, 21, e2020GC009199. https://doi.org/10.1029/2020GC009199

Be´zos, A., S. Escrig, C. H. Langmuir, P. J. Michael, and P. D. Asimow (2009), Origins of chemical diversity of back-arc basin basalts: A segment-scale study of the Eastern Lau Spreading Center, J. Geophys. Res., 114, B06212, doi:10.1029/2008JB005924.

Brian Taylor, Fernando Martinez, Back-arc basin basalt systematics, Earth and Planetary Science Letters, Volume 210, Issues 3–4, 2003, Pages 481-497, ISSN 0012-821X, https://doi.org/10.1016/S0012-821X(03)00167-5.

Cary L. Mrozowski, Dennis E. Hayes, The evolution of the Parece Vela Basin, eastern Philippine Sea, Earth and Planetary Science Letters, Volume 46, Issue 1, 1979, Pages 49-67, ISSN 0012-821X, https://doi.org/10.1016/0012-821X(79)90065-7.

Dupré, B., Allègre, C. Pb–Sr isotope variation in Indian Ocean basalts and mixing phenomena. *Nature* 303, 142–146 (1983). https://doi.org/10.1038/303142a0

Gale A., C. A. Dalton, C. H. Langmuir, Y. Su, and J.-G. Schilling (2013), The mean composition of ocean ridge basalts, *Geochem. Geophys. Geosyst.*, 14, 489–518, doi:10.1029/2012GC004334.

Gale A., C. A. Dalton, C. H. Langmuir, Y. Su, and J.-G. Schilling (2013), The mean composition of ocean ridge basalts, *Geochem. Geophys. Geosyst.*, 14, 489–518, doi:10.1029/2012GC004334.
Gill (1976)

Hall, R.; Fuller, M.; Ali, J.R.; Anderson, C.D. The Philippine Sea Plate: Magnetism and reconstructions. In Active Margins and Marginal Basins of the Western Pacific; Taylor, B., Natland, J., Eds.; AGU: Washington, DC, USA, 1995; pp. 371–404.; Tan, H.Y.; Wang, Z. Seismic velocity imaging and tectonic characteristics of bidirectional subducting slabs under Philippine Archipelago. Chin. J. Geophys. 2018, 61, 4887–4990.

Hart, S. A large-scale isotope anomaly in the Southern Hemisphere mantle. *Nature* 309, 753–757 (1984). https://doi.org/10.1038/309753a0

Hawkins, J. W., and J. T. Melchior (1985), Petrology of Mariana Trough and Lau Basin basalts, *J. Geophys. Res.*, 90(B13), 11431–11468, doi:10.1029/JB090iB13p11431.

Hickey-Vargas, Rosemary. "Isotope characteristics of submarine lavas from the Philippine Sea: implications for the origin of arc and basin magmas of the Philippine tectonic plate." *Earth and Planetary Science Letters* 107.2 (1991): 290-304.

I.M. Artemieva Earth-Science Reviews 236 (2023) 104242 Back-arc basins: A global view from geophysical synthesis and analysis https://doi.org/10.1016/j.earscirev.2022.104242

Ishizuka, O., M. Yuasa, and R. N. Taylor. "Two contrasting magmatic types coexist after the cessation of back-arc spreading." *AGU Fall Meeting Abstracts*. Vol. 2007. 2007.

Jean-Philippe Eissen, Christian Lefe`vre, Patrick Maillet, Gilles Morvan, Masato Nohara, Petrology and geochemistry of the central North Fiji Basin spreading centre (Southwest Pacific) between 16°S and 22°S, Marine Geology, Volume 98, Issues 2–4, 1991, Pages 201-239, ISSN 0025-3227, https://doi.org/10.1016/0025-3227(91)90104-C.

JOHN M. SINTON, LORI L. FORD, BRUCE CHAPPELL, MALCOLM T. McCULLOCH, Magma Genesis and Mantle Heterogeneity in the Manus Back-Arc Basin, Papua New Guinea, *Journal of Petrology*, Volume 44, Issue 1, January 2003, Pages 159–195, https://doi.org/10.1093/petrology/44.1.159

JULIAN A. PEARCE, PETER E. BAKER, PETER K. HARVEY, IAN W. LUFF, Geochemical Evidence for Subduction Fluxes, Mantle Melting and Fractional Crystallization Beneath the South Sandwich Island Arc, *Journal of Petrology*, Volume 36, Issue 4, August 1995, Pages 1073–1109, https://doi.org/10.1093/petrology/36.4.1073

Karig, D. E. (1971). Structural history of the Mariana island arc system. *Geological Society of America Bulletin*, *82*(2), 323-344.

Long Yuan, Quanshu Yan, Yanguang Liu, Shiying Wu, Ruirui Wang, Xuefa Shi; *In Situ* Geochemical Compositions of the Minerals in Basaltic Rocks from the West Philippine Basin: Constraints on Source Lithology and Magmatic Processes. *Lithosphere* 2020;; 2020 (1): 8878501. doi: https://doi.org/10.2113/2020/8878501;

M.Nafi Toksöz, Albert T. Hsui, Numerical studies of back-arc convection and the formation of marginal basins, Tectonophysics, Volume 50, Issues 2–3, 1978, Pages 177-196, ISSN 0040-1951, https://doi.org/10.1016/0040-1951(78)90134-8.

Mantovani, E., Viti, M., Babbucci, D., Tamburelli, C. and Albarello, D. 2001. Back arc extension: which driving mechanism? In: Jessell, M. J. 2001. General Contributions: 2001. Journal of the Virtual Explorer, 3, 17-44

Nisterenko, G. V. "Petrochemistry and geochemistry of basalts in the Shikoku Basin and Daito Basin, Philippine Sea." *Initial Reports DSDP* 58 (1980): 791-804.

Ohara, Y., K. Fujioka, T. Ishii, and H. Yurimoto, Peridotites and gabbros from the Parece Vela backarc basin: Unique tectonic window in an extinct backarc spreading ridge, Geochem. Geophys. Geosyst., 4(7), 8611, doi:10.1029/2002GC000469, 2003.

Okino, K. and Kato, Y. (1995), Geomorphological study on a clastic accretionary prism: The Nankai Trough. Island Arc, 4: 182-198. https://doi.org/10.1111/j.1440-1738.1995.tb00142.x
Okino, K., Kasuga, S. & Ohara, Y. A New Scenario of the Parece Vela Basin Genesis. *Marine Geophysical Researches* **20**, 21–40 (1998). https://doi.org/10.1023/A:1004377422118

Okino, K., Ohara, Y., Kasuga, S., & Kato, Y. (1999). The Philippine Sea: New survey results reveal the structure and the history of the marginal basins. *Geophysical Research Letters*, *26*(15), 2287-2290. https://doi.org/10.1029/1999GL900537

Okino, K., Tani, K., Fujii, M. *et al.* Geophysical investigation of the Mado Megamullion oceanic core complex: implications for the end of back-arc spreading. *Prog Earth Planet Sci* 10, 37 (2023). https://doi.org/10.1186/s40645-023-00570-2

Osamu Ishizuka, Rex N. Taylor, Yasuhiko Ohara, Makoto Yuasa; Upwelling, rifting, and age-progressive magmatism from the Oki-Daito mantle plume. *Geology* 2013;; 41 (9): 1011–1014. doi: https://doi.org/10.1130/G34525.1;

Pearce, J., Barker, P., Edwards, S. *et al.* Geochemistry and tectonic significance of peridotites from the South Sandwich arc–basin system, South Atlantic. *Contrib Mineral Petrol* **139**, 36–53 (2000). https://doi.org/10.1007/s004100050572

Pearce, J.A. and Stern, R.J. (2006). Origin of Back-Arc Basin Magmas: Trace Element and Isotope Perspectives. In Back-Arc Spreading Systems: Geological, Biological, Chemical, and Physical Interactions (eds D.M. Christie, C.R. Fisher, S.-M. Lee and S. Givens). https://doi.org/10.1029/166GM06

Qian, S., Wu, J.TJ. & Wu, J. Philippine Sea plate and surrounding magmatism reveal the Antarctic-Zealandia, Pacific, and Indian mantle domain boundaries. *Commun Earth Environ* 5, 183 (2024). https://doi.org/10.1038/s43247-024-01326-6

Quanshu Yan, Xuefa Shi, Long Yuan, Shishuai Yan, Zhenxuan Liu, Tectono-magmatic evolution of the Philippine Sea Plate: A review, Geosystems and Geoenvironment, Volume 1, Issue 2, 2022,100018, ISSN 2772-8838,https://doi.org/10.1016/j.geogeo.2021.100018.

Quanshu Yan, Xuefa Shi, Long Yuan, Shishuai Yan, Zhenxuan Liu, Tectono-magmatic evolution of the Philippine Sea Plate: A review, Geosystems and Geoenvironment, Volume 1, Issue 2, 2022, 100018, ISSN 2772-8838, https://doi.org/10.1016/j.geogeo.2021.100018

S. FRETZDORFF, R. A. LIVERMORE, C. W. DEVEY, P. T. LEAT, P. STOFFERS, Petrogenesis of the Back-arc East Scotia Ridge, South Atlantic Ocean, *Journal of Petrology*, Volume 43, Issue 8, August 2002, Pages 1435–1467, https://doi.org/10.1093/petrology/43.8.1435

Sanfilippo, A., Dick, H. J. B., Marschall, H. R., Lissenberg, C. J., & Urann, B. (2019). Emplacement and high-temperature evolution of gabbros of the 16.5°N oceanic core complexes (Mid-Atlantic Ridge): Insights into the compositional variability of the lower oceanic crust. Geochemistry, Geophysics, Geosystems, 20. https://doi.org/10.1029/ 2018GC007512
Sdrolias, M., and R. D. Müller (2006), Controls on back-arc basin formation, *Geochem. Geophys. Geosyst.*, 7, Q04016, doi:10.1029/2005GC001090.

SLEEP, N., TOKSÖZ, M. Evolution of Marginal Basins. *Nature* 233, 548–550 (1971). https://doi.org/10.1038/233548a0

Tatsumi and Suzuki-Kamata, 2014 Taylor, B., and G. D. Karner (1983), On the evolution of marginal basins, *Rev. Geophys.*, 21(8), 1727–1741, doi:10.1029/RG021i008p01727.